On the influence of steam on combustion

Marco Derksen

Samenstelling van de promotiecommissie:

Voorzitter:	Prof.dr.ir. H.J. Grootenboer
Secretaris:	Prof.dr.ir. H.J. Grootenboer
Promotor:	Prof.dr.ir. Th.H. van der Meer
Assistent Promotor:	Dr.ir. J.B.W. Kok
Leden:	Prof.dr.ir. H.W.M. Hoeijmakers
	Prof.dr.ir. G.F. Versteeg
	Prof.dr. L.P.H. De Goey
	Prof.ir. J.P. van Buijtenen
	Dr. D.A. Goussis

ON THE INFLUENCE OF STEAM ON COMBUSTION

PROEFSCHRIFT

ter verkrijging van
de graad van doctor aan de Universiteit Twente,
op gezag van de rector magnificus,
prof.dr. W.H.M. Zijm,
volgens besluit van het College voor Promoties
in het openbaar te verdedigen
op vrijdag 29 april 2005 om 15.00 uur

door

Marco Anton Frederik Derksen

geboren op 15 april 1973
te Nijmegen

Dit proefschrift is goedgekeurd door de promotor:

Prof.dr.ir. Th. H. van der Meer

en de assistent promotor:

Dr.ir. J.B.W. Kok

Voor Pap,
voor Opa van Tongeren

Summary

The gas turbine is nowadays a widely used means of power generation. Especially gas turbines operating on natural gas combine very low emissions with a compact design to deliver power at a high overall efficiency. However, the simple cycle gas turbine, consisting of a compressor, a combustion chamber and a turbine, is limited in the maximum efficiency it can attain. For this reason several enhancements of the thermodynamic cycle have been implemented in the past. By far the most popular of these is the use of a steam cycle which employs the exhaust energy of the gas turbine which would otherwise be dumped through the stack. With this so called 'bottoming' steam cycle this 'combined cycle' realizes efficiencies of up to 60%.

There are several drawbacks for the combined cycle. The most eminent of these is that it is only commercially attractive for large scale power plants, typically over 200 MW in size. One of the current challenges in power generation is to design a gas turbine cycle that offers the efficiency and feasibility of the combined cycle, but for lower ranges of power generation. One of these cycles is the range of 'mixed cycles.' In these cycles, steam and air are in direct contact inside the turbine. Of these cycles, the HAT cycle (Humid Air Turbine) or the evaporative cycle are the most promising. They offer efficiencies equal to or better than the combined cycle at a competitive price.

These mixed cycles have in common that steam is present in large quantities before the flame. On the behavior of humidified flames little research is published so far. Some laminar flame results exist, however very little information is gathered on the behavior and emissions of such turbulent flames. It is known that for diffusion flames steam acts to reduce emissions through reducing the peak temperatures of the flame, but little information is known of the influence of humidification of partially premixed or fully premixed turbulent flames. These flames are, in modern-day gas turbines with ultra-low emissions, the most employed types of flames. This fact was one of the incentives to start the European FLAMESEEK programme, where one of the goals was to investigate the influence of steam on humidified premixed flames. The research presented here was in part performed within the framework of this program. To be able to disseminate the results, a burner geometry was also chosen that is available in literature to perform a numerical simulation study. This is the DLR test combustor, described in references [13], [19] and [61].

In this thesis, a numerical simulation study is presented of the influence of steam on premixed and partially premixed combustion. Both laminar (premixed) and turbulent (partially premixed) calculations are presented. The laminar calculations were performed using a detailed chemical mechanism and the 1-dimensional CHEMKIN PREMIX code that allows the numerical simulation of premixed, freely propagating flames. The turbulent calculations were performed using a novel combustion model which is presented here. Results are presented of a case without any dilution, a case with steam dilution and a case with nitrogen dilution.

In chapter 1, an introduction is given to the topic of mixed cycles. The features that are present in these cycles are discussed, and a short overview of the data available in literature is given.

In chapter 2, the CFI turbulent combustion model is presented. The numerical background for the model is given and the transport equations that describe reaction, c, mixing, f, and enthalpy transport, i, are derived. The CSP algorithm that is employed in the model is presented. This algorithm is employed to map a detailed reaction mechanism onto the model's scalars using steady-state and element conservation relations. Also, the chemistry mapping onto the reaction scalars is provided by CSP. Furthermore, the method of solving the transport equations, with the use of a thermochemical database of the source term values as function of the transported properties, is presented and discussed. The creation of the thermochemical database is explained. A data storage and retrieval algorithm is presented here that is used for the efficient storage and retrieval of the thermochemical data. Finally, a discussion is presented on some issues that have arisen in this chapter. In this discussion it is shown that using a manually defined reduced mechanism mapping results in fast modes of the reaction mechanism being present in the reduced mechanism mapping, while slow modes will exist in the steady-state relations. Some points of attention are given with respect to the mapping of the reduced mechanism with respect to the CFI combustion model and with respect to the laminar database program. It is also stated that the thermal NO post processor will be used, instead of the steady-state assumption for NO, in the predictions of NO emissions in turbulent flames.

In chapter 3, a assessment is presented of the laminar databases created for 2 suitable cases using detailed laminar flame simulations obtained with the CHEMKIN PREMIX package. The conclusions of this chapter are that CSP defined reduced mechanism mappings yield better results than their manually defined counterparts. Also, 2-step reduced mechanisms perform better than 1-step reduced mechanisms. However, this difference is too little to necessitate the use of the much larger 2-step reduced mechanism database. Therefore, for subsequent calculations, a 1-step, CSP mapped reduced mechanism is provided which will be used for the turbulent flame calculations. Comparisons also show that the model will perform better closer to stoichiometric conditions. Furthermore, it is also shown that the use of the steady-state assumption for NO will result in overpredictions of its emissions in a flame.

In chapter 4, a study is presented on the effects of steam on a turbulent, partially premixed flame. For this reason, also a laminar study is included. A case with steam dilution and a case with nitrogen dilution are presented along with the Base case without dilution. The overall adiabatic flame temperature and inlet temperature have been kept constant. In the dilution cases, the volume flows of diluent were constant, the burner power is slightly adjusted to maintain a constant overall adiabatic flame temperature. At the overall mixture fractions, laminar premixed flame calculations were performed with detailed chemistry. The turbulent flame calculations were performed using the CFI combustion model, without nonadiabatic effects included. The turbulent combustor is obtained from DLR (Deutsches Zentrum fr Luft und Raumfahrt) and is a scale model of an industrial gas-turbine combustor. A case was chosen which proved to burn very stable at a sufficiently high Reynolds number. The inlet temperature of this case was raised with respect to this to ensure all diluents (most importantly water) were present in gaseous form. The results here show that the turbulent flow and temperature fields are identical for all cases. The species concentrations fields are however very different. The laminar and turbulent results differ with respect to the trend in reducing the emissions of NO. The laminar calculations show that nitrogen dilution raises the emission level of the flame and that steam lowers it, while the turbulent calculations show that both nitrogen and steam reduce NO

emissions, but that steam yields a higher reduction than nitrogen. The trends observed in the turbulent simulations are shown to compare very well with those observed in measurements performed for this work, on a similar turbulent flame, with comparable amounts of steam and nitrogen dilution. These results illustrate it is not always possible to translate results obtained with laminar flames to a turbulent situation. In the turbulent flames, NO is reduced by a reduction of peak temperatures, and a reduction of the peak O radical concentration. By chemical action, steam acts to further reduce the peak O concentration than nitrogen does.

In chapter 5, conclusions of various chapters are repeated and some recommendations are given. Some recommendations for the improvement of the CFI combustion model are given. Furthermore, it is recommended to execute a turbulent validation of the CFI combustion model, and to incorporate and investigate the effects of heat loss through radiation in the turbulent flame simulations presented here.

Samenvatting

De gasturbine is een veelgebruikt middel om energie mee op te wekken. In het bijzonder de gasturbines die aardgas als brandbaar medium gebruiken combineren zeer lage emissies met een compact ontwerp en hoge rendementen. Echter, de zogenaamde 'eenvoudige-cyclus' gasturbine, bestaande uit een compressor, verbrandingskamer en een turbine, is gelimiteerd in haar maximaal haalbare rendement. Om deze reden zijn er in het verleden verscheidene verbeteringen aangebracht in de thermodynamische cyclus die hieraan ten grondslag ligt. Verreweg de meest populaire hiervan is het gebruik van een additionele stoomcyclus die de resterende energie benut die bij de eenvoudige cyclus door de schoorsteen verdwijnt. De zo ontstane 'gecombineerde cyclus,' met deze 'afromende' stoomcyclus, realiseert rendementen tot 60%.

Er kleven verschillende nadelen aan de gecombineerde cyclus. De meest prangende daarvan is dat deze alleen economisch aantrekkelijk is voor grotere installaties, groter dan ongeveer 200 MW. Een van de hedendaagse uitdagingen in energieopwekking is het creëren van een gasturbinecyclus die de efficiëntie en realiseerbaarheid van de gecombineerde cyclus geeft, maar voor installaties met lagere niveaus van energieopwekking. Van deze cycli zijn de HAT cyclus (Humid Air Turbine, ofwel 'vochtige lucht turbine') en de 'verdampende cyclus' het meest veelbelovend. Deze leveren rendementen vergelijkbaar met- of zelfs beter dan die van de gecombineerde cyclus, tegen een competatieve prijs.

Deze cycli, ook wel 'gemengde cycli' genoemd hebben met elkaar gemeen dat stoom in grote hoeveelheden aanwezig is vóór de vlam. Over het gedrag van dit soort vochtige vlammen is tot nu toe weinig gepubliceerd. Er bestaat literatuur over laminaire vlammen, er is echter weinig informatie bekend over het gedrag en de emissies van zulke turbulente vlammen. Van diffusievlammen is bekend dat stoom de piektemperaturen in de vlam reduceert, maar weinig informatie bestaat over de invloed van stoom op gedeeltelijk- of volledig voorgemengde vochtige turbulente vlammen. Dit soort vlammen komt voor in vrijwel alle moderne gasturbines met ultralage emissies. Dit feit was onder andere de achtergrond voor het Europese FLAMESEEK project, waar één van de doelen was het onderzoeken van de invloed van stoom op voorgemengde vlammen. Het onderzoek dat in dit proefschrift wordt gepresenteerd is deels gedaan als onderdeel van dat project. Om de resultaten beter te kunnen dissemineren, werd er ook een brandergeometrie gekozen die beschikbaar was in de literatuur. Hiermee zijn numerieke simulaties gedaan. Dit is de DLR brander en verbrandingskamer die beschreven wordt in referenties [13], [19] en [61].

In dit proefschrift wordt een numerieke studie gepresenteerd over de invloed van stoom op volledig- en gedeeltelijk voorgemengde verbranding. Zowel laminaire (voorgemengde) als turbulente (gedeeltelijk voorgemengde) berekeningsresultaten worden gepresenteerd. De laminaire berekeningen zijn gedaan met een gedetailleerd chemisch reactiemechanisme en de 1-dimensionale CHEM-

KIN PREMIX code waarmee onder andere voorgemengde, vrij propagerende vlammen kunnen worden gesimuleerd. De turbulente berekeningen zijn uitgevoerd met een nieuw verbrandingsmodel welke hier ook wordt gepresenteerd. Resultaten van een berekening zonder enkele verdunning, en berekeningen met respectievelijk stoom- en stikstofverdunning zullen worden beschouwd.

In hoofdstuk 1 van dit proefschrift wordt een introductie gegeven over het onderwerp van de gemengde cycli. De eigenschappen van deze cycli worden besproken en een kort literatuuroverzicht zal worden gegeven.

In hoofdstuk 2 wordt het CFI verbrandingsmodel gepresenteerd. De numerieke achtergrond voor het model wordt uitgelegd en de transportvergelijkingen die reactie, c, menging, f, en enthalpietransport, i, weergeven worden afgeleid. Het CSP algoritme dat in het model wordt gebruikt wordt gepresenteerd. Dit algoritme wordt gebruikt om een gedetailleerd reactiemechanisme te reduceren op de scalairen van het model, gebruik makend van aannames betreffende evenwicht van stoffen en van elementbehoudsvergelijkingen. De samenstelling van de reactiescalairen c wordt ook gegenereerd door het CSP algoritme. De oplosmethode voor de aldus verkregen transportvergelijkingen, waar een thermochemische database wordt gebruikt voor de opslag van de waarden van de diverse brontermen als functie van de transportgrootheden, wordt beschreven en bediscusiëerd. Ook wordt uitgelegd hoe de thermochemische database wordt verkregen. Een data opslag- en terugwinalgoritme wordt gepresenteerd ten behoeve van het efficiënte gebruik van de database. Ten slotte wordt een discussie gegeven over sommige onderwerpen die beschreven zijn in dit hoofdstuk. In deze discussie wordt getoond dat bij het gebruik van een manuele definitie van de samenstelling van het gereduceerde mechanisme, snelle modi van het reactiemechanisme aanwezig zullen zijn in het (langzame) gereduceerde mechanisme, terwijl langzame modi zullen bestaan in de (snel geachte) evenwichtsvergelijkingen voor stoffen. Enkele aandachtspunten worden gegeven met betrekking tot het beschrijven van het gereduceerde mechanisme in relatie tot het CFI verbrandingsmodel en het laminaire database programma. Het gebruik van een post-processor voor de berekening van de NO massafractie wordt uitgelegd, in plaats van het gebruik van een evenwichtsaanname voor deze stof in de voorspellingen van NO emissies van turbulente vlammen.

In hoofdstuk 3 wordt een studie gepresenteerd van de laminaire databases die zijn gecreëerd voor 2 representatieve gevallen, waarbij resultaten op basis van gedetailleerde chemie, verkregen met CHEMKIN PREMIX, worden gebruikt als toetssteen. Hieruit blijkt dat de CSP-gedefinieerde gereduceerd mechanismebeschrijvingen betere resultaten geven dan de manueel gedefinieerde versies. Verder zijn de resultaten van de 2-staps mechanismen beter dan die van de 1-stapsmechanismen. Echter, de verschillen tussen die laatste twee zijn te klein om het gebruik van een 2-staps mechanisme te rechtvaardigen. Daarom is voor verdere berekeningen gekozen voor het gebruik van het 1-staps, CSP gedefinieerd gereduceerd mechanisme. Dit zal ook worden gebruikt voor de turbulente vlamsimulaties verderop in dit proefschrift. Een verdere laminaire vergelijking laat ook zien dat het CFI-model beter zal presteren bij condities dichter bij stoichiometrie van het mengsel met de brandstof. Het wordt ook zichtbaar gemaakt dat het gebruik van een evenwichtsaanname voor NO zal resulteren in overschattingen van deze emissies in een vlam.

In hoofdstuk 4 wordt een studie beschreven naar de effecten van stoom op een turbulente, gedeeltelijk voorgemengde vlam. Ook laminaire studie wordt betrokken in de discussie. Naast een basisberekening, zonder verdunning wordt een berekening gegeven van een stoom- en van een stikstofverdunde vlam. In deze berekeningen is de volumestroom van verdunningsmiddel constant gehouden, het brandervermogen werd iedere keer licht bijgesteld om een constante adiabatische vlamtemperatuur te

verkrijgen. Voor de waarden van de gemiddelde mengfracties, werden laminaire berekeningen uitgevoerd aan voorgemengde vlammen, met gedetailleerde chemie. Voor de turbulente vlamberekeningen wordt het CFI verbrandingsmodel gebruikt, waar niet-adiabatische effecten genegeerd worden. De verbrandingskamer- en brandergeometrie is verkregen van het DLR (Deutsches Zentrum fr Luft und Raumfahrt) en is een schaalmodel van een industriële gasturbinebrander en -verbrandingskamer. Als basisberekening worden randvoorwaarden gekozen waarbij de brander heeft bewezen stabiel te werken onder een voldoende hoog Reynolds getal. Van deze randvoorwaarden is de inlaattemperatuur verhoogd om er zeker van te zijn dat alle bestanddelen (voornamelijk water) er aanwezig zijn in gasvormige toestand. De resultaten laten zien dat de turbulente stromings- en temperatuurvelden identiek zijn voor alle berekende gevallen. De concentratieprofielen voor verschillende stoffen zijn echter zeer verschillend. De laminaire en turbulente resultaten verschillen in de trend waarin de NO emissies worden gereduceerd. De laminaire berekeningen laten zien dat stikstof de NO emissies doet stijgen, terwijl stoom deze doet dalen. De turbulente berekeningen daarentegen laten een dalende trend zien voor zowel stikstof- als stoominjectie, waarbij stoom een hogere emissiereductie veroorzaakt dan stikstof. De trend die geobserveerd is in de turbulente berekeningen vergelijkt zeer goed met die welke geobserveerd is in metingen aan een vergelijkbare gedeeltelijk voorgemengde vlam, met vergelijkbare hoeveelheden stoom- en stikstofverdunning. Deze resultaten illustreren dat het niet altijd mogelijk is resultaten, verkregen met laminaire vlamsimulaties, direct te vertalen naar een turbulente situatie. In de turbulente vlammen wordt NO gereduceerd door een combinatie van een reductie in piektemperaturen en een reductie van de piek O-radicaalconcentratie. Door middel van chemische actie van stoom wordt hierdoor de piek O-concentratie verder gereduceerd dan het geval is in de stikstofverdunde vlam.

In hoofdstuk 5 worden de conclusies uit de diverse hoofdstukken samengevat en worden enkele aanbevelingen gegeven. Zo worden er aanbevelingen gedaan ter verbetering van het CFI verbrandingsmodel. Ook wordt het aanbevolen een turbulente validatie uit te voeren van het CFI verbrandingsmodel, en om de effecten van warmteverlies door straling op te nemen in de turbulente vlamsimulaties die in dit proefschrift gepresenteerd zijn.

Voorwoord

Dit proefschrift is de vrucht van 4 jaar arbeid bij de vakgroep Thermische werktuigbouw aan de universiteit Twente. Tijdens deze periode heb ik veel meer ervaringen opgedaan dan ik in dit proefschrift kan vermelden. Deze ervaringen heb ik opgedaan op zowel het wetenschappelijk als het persoonlijk vlak en ik mag wel zeggen dat ik er een ander mens door ben geworden. Een promotie is een uitstekende kans om jezelf beter te leren kennen en door vallen en opstaan wijzer te worden. Diegene die het alleen ziet als een wetenschappelijke verrijking is zeker aan het verkeerde adres. Nu ik op het punt sta om de universiteit te verlaten na bijna 12.5 jaar, en mezelf te storten in het bedrijfsleven, kan ik zeggen dat dit een boeiende, leerzame en enerverende periode is geweest.

Vele mensen hebben mijn pad gekruist in deze periode, maar een aantal wil ik toch met name noemen. Mijn begeleiders Theo van der Meer en Jim Kok wil ik in het bijzonder bedanken voor de intensieve steun die ik altijd van ze gekregen heb, en het onvoorwaardelijke vertrouwen dat ze altijd in me gehad hebben. Zonder hun steun zou het proefschrift niet in deze vorm voor u gelegen hebben. Verder ben ik erg veel dank verschuldigd aan Dimitris Goussis. Zijn oneindige geduld, en grote parate kennis van lineaire algebra, stromingsleer en chemie hebben me geholpen de kennis eigen te maken op het gebied van CSP en ook om de links te kunnen leggen tussen deze wiskundige theorie en de praktische toepassingen ervan in de chemie en de stromingsleer. De vele discussies over allerlei - vaak ook niet wetenschappelijke - onderwerpen tijdens mijn verblijven in Rio-Patra hebben me veel geleerd en geholpen. Efcharisto para poli! Ook wil ik mijn kamergenoten in mijn promotieperiode noemen. Behalve de vele lol, goede gesprekken en discussies die ik met ze heb gehad zijn Nutte en Edwin vooral goede vrienden geworden.

Verder wil ik de studenten bedanken die een deel van dit werk hebben uitgevoerd. Dat zijn Nutte en Mark, waarbij Nutte mede verantwoordelijk is geweest voor de realisatie van de meetopstelling, en waaraan Mark o.a. de metingen met stoom- en stikstofinjectie heeft uitgevoerd. Verder heeft Nutte alle geometriën waaraan ik heb gerekend in Solid Works gezet, hetgeen mij een enorme hoeveelheid tijd en moeite heeft gescheeld. Dank ook aan Jaap, Bram en Sjoerd voor de hulp bij de implementatie van mijn code in het pakket CFX. Verder wil ik alle studenten, promovendi en medewerkers van de vakgroep bedanken voor de aangename tijd die ik hier gehad heb.

Mijn ouders, mijn broertje en zijn vrouw, bedankt voor alles. Ik ben er trots op zo'n familie te hebben. Manon, zoals jij is er maar één. Bedankt voor je steun, je liefde, je begrip, voor jij zoals je bent.

Marco Derksen

Enschede, december 2004

ix

x

Acknowledgement

Contents

Chapter 1

Introduction

The gas turbine is nowadays a widely used means of power generation. It offers a relatively cheap, light and small power generation unit. In these respects it is favorable over steam plants or reciprocating engines, while achieving comparable or better efficiencies [60]. The oil crisis in the nineteen seventies put the emphasis of power generation on fuel efficiency, which has led to the introduction and subsequent widespread use of the combined cycle [30]. In this cycle the gas turbine exhaust heat is utilized in a steam cycle, increasing the efficiency of the total system to over 50%, compared to around 30% for the single cycle. The drawback of the combined cycle is that it is only economically attractive for large-scale power plants, typically over $200MW$ in size. For smaller sizes, below $100MW$, efficiency decreases and specific cost increases [42], for plant scales under $30MW$ its efficiency is typically about 42% [30]. Since the bottoming steam cycle becomes uneconomically expensive at these lower power ranges, other means are necessary to improve the performance of the gas turbine cycle to reach values of the large-scale combined cycle plants. Various methods have been proposed which all increase the thermodynamic efficiency of the gas turbine cycle. These modern cycles are referred to as 'Advanced Cycles.' For an in depth discussion of these cycles, one is referred to the literature, e.g. refs. [15] or [30].

One range of advanced cycles is the range of 'mixed cycles': steam is incorporated into the gas cycle. These cycles utilize one or more heat transfer processes which increase the efficiency and/or specific power, employing water or steam in one or more of the heat exchanger flows. The actual heat exchanger can either be an indirect one, where water/steam is physically separated from the gas flow. It can also be direct, where water/steam is in direct contact with the gas, with hence a mixture of both existing in the heat exchanger. The overall efficiency of such a system can rival, or even surpass, those for large-scale combined cycles.

There are various implementations of the mixed cycle. A main distinction can be made in cycles where the steam injection location is before-, and cycles where it is behind the flame of the gas turbine. Since the research of this thesis focusses on the impact of steam on a flame, the range of mixed cycles where steam or water is injected before the flame will be the main topic of interest here. This leads to the range of evaporative cycles, which will be discussed below. First, a short summary of some processes involved will be given, starting with a description of the simple gas turbine cycle, following a short description of heat transfer processes employed in evaporative cycles.

1.1   The simple cycle

The gas turbine cycle is a realization of the Brayton or Joule cycle. The T-S and flow diagram of this cycle are shown in figure 1.1, where T is the temperature and S the entropy. In this so-called "simple cycle" or SC, the gaseous medium, almost always air, is isentropically compressed (1-2 in figure 1.1), isobarically heated (2-3), isentropically expanded (3-4) and finally isobarically cooled (4-1) in subsequent steps.
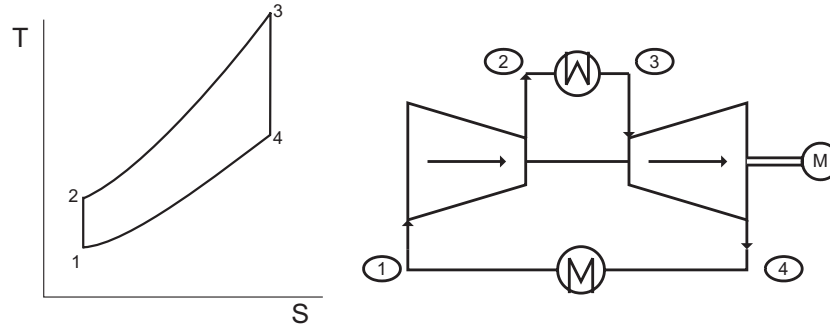
Figure 1.1: The Joule-Brayton simple cycle, T-S-diagram (left) and plant flow scheme (right).

Heating is often done by directly burning fuel in the compressed medium, or sometimes indirectly, via a heat exchanger. The second heat exchanger, representing process (4-1) in figure 1.1 is not actually present in a simple cycle, it represents the heat loss of the turbine exhaust stream to the atmosphere. This exhaust stream still can possess temperatures up to 400^0C and, together with the mixing losses in the combustion chamber, account for the greatest sources of efficiency loss [9]. Reducing mixing losses can increase overall efficiency with a few percentage points by fuel preheat and a higher Turbine Inlet Temperature (or TIT, the temperature at point 3 of figure 1.1) [60], but waste heat recovery or reduction are the major sources for efficiency improvements by gas turbine manufacturers [9].

The efficiency and/or specific work output of the simple cycle can be enhanced with several methodologies, see e.g. [15]. Of these, especially intercooling, recuperation and aftercooling are employed in mixed cycles. They will shortly be discussed below.

1.2   Intercooling, recuperation and aftercooling

All three mentioned processes have in common that they are heat exchanging processes. They help to improve efficiency and/or specific work.

Using intercooling, compression is split into two or more steps where in between the medium is cooled in a heat exchanger. This reduces total compression work therefore increases specific work. Generally efficiency decreases as more fuel is needed to obtain the same TIT as in the reference cycle. In figure 1.2 intercooling is represented by $1 - 1a - 1b - 2'$.

Recuperation is represented by points $2 - 3'$ and $4 - 4'$ in figure 1.2. The heat released by $4 - 4'$ is used to heat the compressed gases from 2 to $2'$. This reduces the amount of fuel needed for increasing the temperature to T_3, reduces the amount of heat lost to the environment, and therefore increases the

Figure 1.2: T-S-diagram of intercooling, recuperation and aftercooling.

efficiency. Ideally, $T_4 = T_{3'}$ and $T_{4'} = T_2$, but this requires an infinitely large heat exchanger area and is therefore not feasible. It also follows from figure 1.2 that recuperation is only possible when $T_4 > T_2$, or $T_4 > T_{2'}$ when intercooling is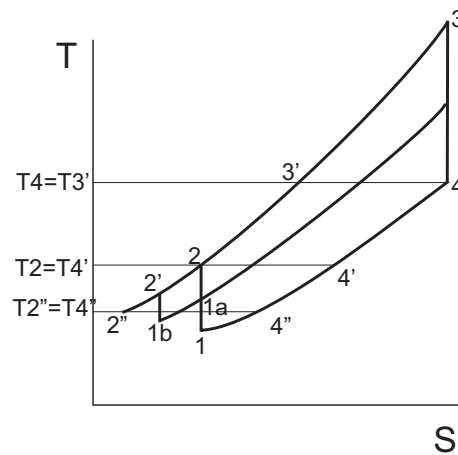 used. This limits the use of a recuperator, certainly if also other efficiency enhancing measures have been taken which reduce the turbine exit temperature T_4. Walsh and Fletcher [60] report a maximum efficiency increase of around 10% with respect to the normal single cycle. An economizer is a secondary recuperator, but with lower grade heat exchange, to recover even more exhaust heat.

Aftercooling serves the same purpose as intercooling, lowering efficiency and increasing specific work. However, when combined with recuperation, it allows the possible heat regained in the recuperator to increase. For a recuperated machine, aftercooling can therefore lead to an *increase* in overall efficiency. Looking at figure 1.2 the cold stream available for the recuperator to heat is $2'' - 4$, which lowers the waste heat temperature to $T_{4''}$ and therefore lowers the heat loss to the environment. Also, aftercooling reduces the temperature difference between the hot and the cold stream of the recuperator, reducing mixing losses which is beneficial for efficiency.

In an actual gas turbine part of this air stream is used to cool parts in the hot gas flow path, such as the turbine rotor and stator blades. This significantly lowers efficiency since it involves mixing of high- and low temperature streams, throttling of high-pressure air to intermediate or low pressure levels, heat transfer etc. Intercooling and aftercooling both lower the compressor discharge temperature, T_2 in figure 1.1. This reduces the necessary coolant flow and also increases the amount of air that passes through the combustion chamber, therefore the effects on efficiency of intercooling and aftercooling can be highly beneficial and even lead to a higher efficiency [42]. Also, in a non-ideal cycle the compression work is greater than in the ideal case, hence, at low pressure ratios, the reduction in work done by the compressor can more than compensate for the additional fuel required [52].

1.3 Evaporative cycles

In most existing gas turbine cycles, water or steam injection is employed as a 'power boost,' to be able to respond to extra temporary power demands when the machine is already running on full load. Also

evaporative inlet cooling is employed in hot areas. The injected amounts of water in these methods do not necessitate modifications to the components of the gas turbine, and are typically in the order of 2 to 4% of the air mass flow [51]. Therefore these should not be considered as 'mixed' cycles. In evaporative cycles, the amounts of water injected are much higher, in the order of 10 to 15% of the air mass flow.

1.3.1   Thermodynamic advantages

The main advantage of water is that it requires little work in compression, but increases the total mass flow through the turbine, thereby improving the specific power output of the cycle. This is amplified by the greater heat capacity of water with respect to air.

The efficiency of evaporative cycles is relatively insensitive to the pressure ratio, for pressure ratios greater than the one for optimal efficiency [6][9][17]. This means that increasing the pressure ratio for better specific power output does not lead to severe reductions in efficiency.

Part load performance is improved with respect to the simple cycle since steam can replace fuel demand [57]. Nakhamkin *et al.* [46] report that cycle part load has negligible efficiency degradation. At 75% of the rated power output, a combined cycle has 4% reduced efficiency while the simple cycle nearly 10%.

Traverso and Massardo [56] have performed a thermoeconomic comparison of a medium-sized mixed cycle with a combined cycle. They conclude that, although maximum cycle efficiency is always attained by the combined cycle, it cannot compete with mixed cycles because of the need of a heat recovery system with at least 2 pressure levels, and because of steam turbine and other purchase costs. At the medium power range of $50MW$, lowest energy cost and interest-return rates (IRR) are obtained by the mixed cycles. Nakhamkin *et al.* [46] conclude that a Cascaded HAT cycle (described further on in this chapter) is 15 to 20% cheaper in specific costs than a representative combined cycle plant. This difference increases with ambient temperature, due to the decreased sensitivity to this factor from the mixed cycle.

1.3.2   The water issue

Of the disadvantages mentioned in literature, the amount of make-up water needed and its purity are mentioned the most, see e.g. [9][17][22][25][54][56][57]. Chiesa *et al.* [9] note that water make-up requirements are similar to comparable combined cycles using wet cooling towers, and are less when blowdown water requirements are also taken in consideration. However, in areas where water is scarce or its use is severely restricted, this might pose a problem and a water separation unit should be considered there.

Regarding the water purity requirements, Ågren [1] and Rosén [54], reporting findings from a HAT cycle pilot plant, note that in evaporative cycles the evaporator works as a distiller. This enables the plant to work with low-grade water, possibly even with sea water and even has the potential to scrub air from impurities. El-Masri [16] notes that using low-grade water is only possible if the water injectors are designed to create a mist which evaporates before it impinges to the recuperator walls. Impingement can lead to fouling which can then only be avoided when high-purity water is used or a recuperator which lends itself to quick, periodic cleaning. Also, one should be aware that low-quality water can only be employed in a evaporative cycle if evaporation is complete. Droplets will carry

excessive pollutants into the turbine. Either no overspray should be allowed, or a mist eliminator should be employed [1]. Tuzson [57] reports that the water treatment cost is estimated to be a few percent of the fuel cost, and therefore should not be considered an obstacle.

A thermodynamic drawback of the evaporative cycle compared to the combined cycle is that in the former the expansion is to atmospheric pressure whereas in the latter steam is expanded to much lower pressures. Also part of the steam is liquified in the steam turbine expansion of the combined cycle. However, these thermodynamic drawbacks are more than overcome in the evaporative cycle, owing to its possible higher efficiencies.

1.3.3 The HAT cycle

One of the most promising evaporative cycles is the range of HAT cycles. A Humidified Air Turbine, or Humid Air Turbine, both abbreviated with HAT, is a cycle patented by Rao [50] which is inter-cooled, evaporatively aftercooled and recuperated. A schematic of the cycle is shown in figure 1.3. Water is indirectly preheated in an economizer and an intercooler and an indirect aftercooler. It is mixed with the airstream in a saturator which also acts as a direct contact aftercooler. Here water is allowed to evaporate into the airstream. The water vapor - air mixture is further heated in a recuperator, evaporating any water that might be entrained in the evaporator exhaust flow and superheating it. Fuel is added in the combustion chamber, where the mixture is burnt, increasing the temperature. Subsequently the combusted mixture is expanded in a turbine, after which further heat is extracted in the recuperator and economizer before leaving through the stack.
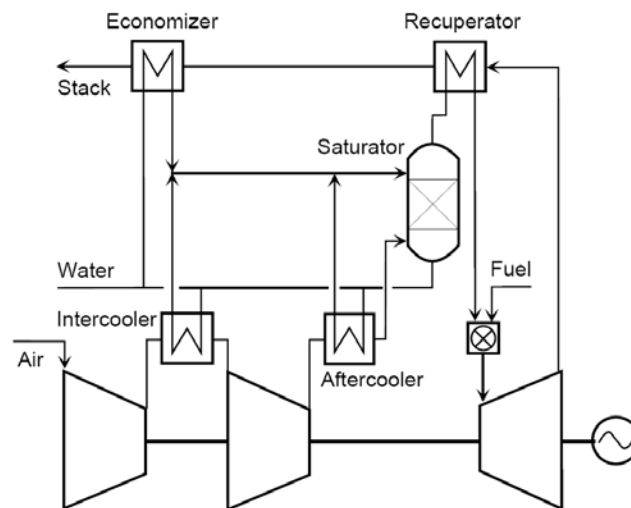
Figure 1.3: Schematic of the HAT cycle (from Korobitsyn [30]).

The main thermodynamic advantage of this cycle lies in the heat transfer of flows with relatively small temperature differences. It does not require a bottoming steam cycle to achieve efficiencies above 50% [9]. The different implementations of the HAT cycle mainly vary in the number of heat exchangers employed and their respective locations in the cycle. These are named Cascaded HAT or CHAT (which also employs reheat) [46], Humid Air Water Injection Turbine or HAWIT (with evaporative intercooling) [56], or Evaporative Gas Turbine cycle (EGT or EvGT) (see e.g. [26] [54]).

Lazzaretto and Segato [35][36] (and later in ref. [37]) optimized the heat exchanger network in the HAT cycle using rules of pinch technology and exergy analysis. A minimal number of 5 heat exchangers was found for a cycle with an efficiency of 55%: a saturator which acts as an evaporative aftercooler, a recuperator and an economizer, and two intercoolers.

1.4   The influence of steam on combustion

The thermodynamics of the HAT cycle and other evaporative cycles are widely studied, as is described in the previous sections. However, the influence of steam on turbulent flames, especially with respect to the emissions, has been given little attendance in literature. A survey by Barghava *et al.* [5] showed that most data on humidified flames is on diffusion flames. There it was concluded that most of the reduction in NO emissions was due to the reduction in flame peak temperatures by water addition. For premixed flames, the following routes of NO reduction are mentioned:

- Reduction in equilibrium temperature

- Reduction in heat-release rate

- O atom suppression

The concentration of the O-atom is suppressed through different mechanisms. Added water necessitates combustion closer to stoichiometric fuel-air ratios if the adiabatic flame temperature is to be kept constant. This reduces the available oxygen and hence the O-atom concentration. Also, the abundance of H_2O shifts the equilibrium of the elementary reaction $O + H_2O \rightleftharpoons 2OH$ to the right. According to Bhargava *et al.*, the lower O-radical concentration reduces NO produced in the thermal and $N2O$-mechanisms, while the higher OH radical concentration reduces prompt NO production. In their experimental setup, lower NO emissions were indeed measured when steam was added. However, these were plotted normalized to dry air with 15% O_2. As discussed in the paper by Landman *et al.* [34] this procedure might be adequate to represent emission data for dry flames, it overestimates the effect of steam on emissions. Since this normalization is on *dry* air, a biassed normalization will occur in humidified flames where part of the oxidizer stream is H_2O. Therefore Landman *et al.* propose to plot NO-emissions on a g NO per GJ basis. Also, the data should be plotted for the logarithm of NO versus the inverse of temperature, to be able to assess the Arrhenius behavior of the NO emission.

Another way through which NO emissions might be reduced in turbulent flames is through the cushioning effect of H_2O. In a turbulent flame the local temperature is subject to turbulent fluctuations. In regions of high temperatures more NO will be created than in regions with lower local temperatures. An abundance of water might lead to a more uniform temperature profile since water absorbs and radiates much more effective than N_2 or O_2. Pockets of near-stoichiometric fuel-oxidizer mixtures will radiate more heat and will therefore achieve temperatures lower than the corresponding adiabatic flame temperature.

The possible chemical influence of H_2O on NO emissions is assessed in the framework of this thesis, in an experimental study. Results are reported in a paper by Landman *et al.* [34]. To eliminate the effect of dilution, equal amounts by mole of H_2O or N_2 are injected in the flame, at various pressures, burner powers, and equivalence ratios. Operating points have been chosen in such a way
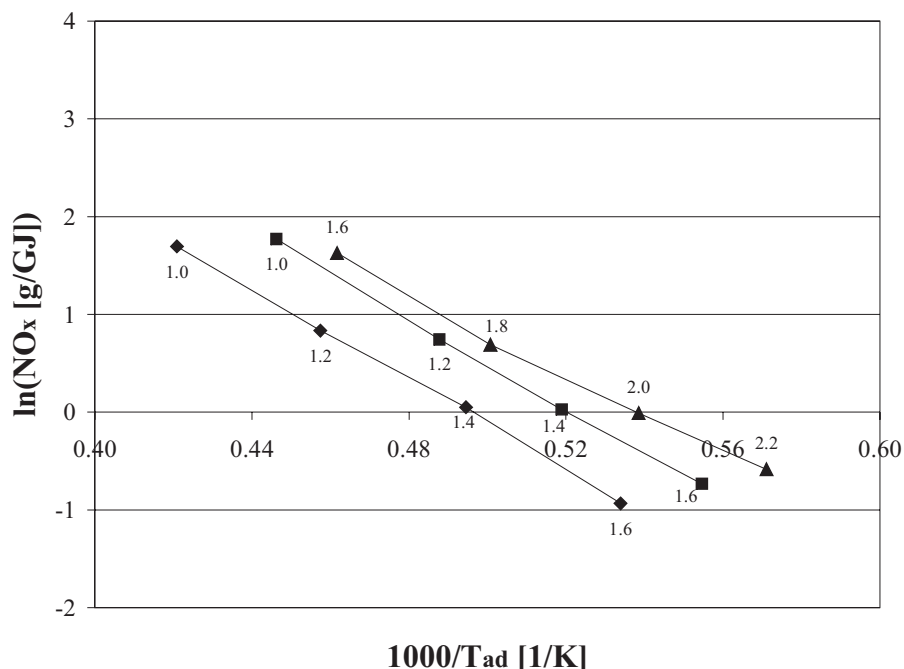
Figure 1.4: Log of NO emissions as a function of the inverse temperature. Also published in [34].

that the burner flow field is kept as constant as possible, to eliminate effects of residence time on emissions. It is concluded that both H_2O and N_2 addition reduce NO emissions, at constant adiabatic flame temperature, where the reduction by H_2O addition is a factor of approximately 2 larger than the reduction by N_2 addition. This is illustrated in figure 1.4, which is a typical result of the measurements performed. In this figure, the NO emissions are plotted on a logarithmic scale versus the inverse of temperature. These results indicate that besides oxygen deficiency water also has an effect on the chemistry leading to NO emissions, such as the shift in elementary reaction of $O + H_2O \rightleftharpoons 2OH$, as also suggested by Barghava *et al.* for diffusion flames. These measurement results and the results of Barghava *et al.* indicate that chemistry might be important in the production of NO in humidified flames. However, to the knowledge of the author, no turbulent flame simulations, on premixed, diffusion or partially premixed flames, have been performed addressing this point. Also, the influence of steam on the burner flow field and flame front position is not known to be assessed in literature.

In this thesis, calculations will be presented on premixed and partly premixed laminar and turbulent flames with steam- or nitrogen- dilution, and without any dilution. The turbulent simulations will be performed using a turbulent combustion model that is presented here, which is developed at the laboratory of Thermal Engineering of the University of Twente. The model employs the CSP algorithm [44] to map a detailed reaction mechanism onto dimensionless scalars which represent combustion progress, additional dimensionless scalars are used to represent turbulent mixing and heat loss. The performance of the model will be assessed using laminar, one-dimensional, freely propagating methane-air flames which are calculated using the CHEMKIN PREMIX code [28] using detailed chemistry according to the GRI-3.0 reaction mechanism [55].

1.5   Scope of the thesis

In chapter 2, the turbulent combustion model will be described that will be used in the simulations. It will be derived from the general species transport equation, equations will be given for the description of turbulent premixed as well as nonpremixed combustion using presumed-PDF Favre averaging and first order moment closure. Combustion progress, mixing and enthalpy loss are described using dimensionless scalars. The use of the CSP algorithm is introduced, to map a detailed reaction mechanism on the model's transport equations that represent combustion progress. The chemical source terms of the turbulent transport equations are calculated and averaged *à priori* and stored in a thermochemical database which is called during simulations. The database creation procedure, as well as the data storage and retrieval methods will be discussed.

In chapter 3, a laminar assessment of the combustion model will be given. Here the thermochemical database will be compared to numerical results from 1-dimensional, laminar, premixed, freely propagating methane flames, with respect to species profiles and temperature. Using this laminar assessment, an indication can be given of the performance of the model in turbulent flame simulations. Also the accuracy of predictions of NO emissions with the Zeldovich mechanism is discussed. A stoichiometric and a lean case are selected to assess the performance of the model.

In chapter 4, simulations are presented of steam- and nitrogen diluted turbulent partially premixed flames, as well as results of laminar, 1-dimensional, premixed, freely propagating flames. For the turbulent flame simulations, a geometry of a scale model of a gas turbine combustor will be employed which is also used by DLR (Deutsches Zentrum fur Luft und Raumfahrt). Based on measurement results of that flame [61], a case is selected which is proven to burn stably and has a sufficiently high Reynolds number to be in the range of Reynolds independent flow. Using this geometry, 3 cases are selected to assess the influence of steam on the emissions and on the combustor flow field. A Base case is selected based on the case by DLR that has proven to burn stably. Subsequently, a Steam case is calculated with 15 volume % of steam and a N2 case with 15 volume % of nitrogen. In these 3 cases, the overall adiabatic flame temperature is kept constant by modifying the burner power, the inlet temperature is identical for all cases and the burner flow field has been kept as constant as possible by keeping the volume flow constant for all 3 cases. The last item is realized by replacing some of the air by diluent in the N2- and Steam cases. At the values of the overall mixture fractions, premixed laminar 1-dimensional flame simulations have been performed as well for these 3 cases.

Chapter 2

The CFI turbulent combustion model

The numerical description of turbulent combustion is a rapidly growing area of research in light of the increasing environmental and economical demands on combustion systems. To meet these demands a better understanding of combusting flow fields is essential and numerical simulation is becoming ever more used to achieve this.

The full numerical simulation of a combusting turbulent flow field in a industrial combustor is still not feasible. Therefore one has to resign to making simplifications of the expressions used to describe the combusting flow field. This turbulent combustion modeling is widely used and there are many variations in the way the expressions are simplified. The modeling work can be divided into two main branches: modeling of combustion and of turbulence. The former topic will be discussed here, in specific the modeling using the CFI turbulent combustion model.

The turbulent combustion model that is used and will be described here uses reaction progress variables to describe the chemical reaction progress. The model has been developed and used at the laboratory of Thermal Engineering of the University of Twente [29] [39] [40] [64]. It is derived from first principles, the scalar transport equations are derived from the species transport equations using generally accepted closures. It employs detailed chemistry which is mapped onto a limited number of transport equations. Other methods that are widely used are flamelet modeling, conditional moment closure modeling and more simple approaches such as the 'mixed is burnt' approach or the Eddy break-up modeling. For reviews, see e.g. references [7] and [59].

First, a description of the expressions describing combustion will be given below. Then it will be described how these expressions are simplified, using turbulence and combustion modeling. Finally, the CFI combustion model will be introduced and described.

2.1 The numerical description of combusting flow fields

To be able to describe a combusting flow field involving N species consisting of E elements, N expressions need to be solved since this is the number of unknowns. These expressions, together with conservation equations for energy and momentum and an equation of state describe the combusting flow field. The equations are described in great detail, e.g. by Williams [63] and will be summarized here. These equations, where only the assumptions made are that the ideal-gas law applies and body forces can be ignored, are:

Continuity

$$\frac{\partial \rho}{\partial t} + \nabla . (\rho \boldsymbol{u}) = 0 \tag{2.1}$$

In this expression, ρ is the mass density and $\boldsymbol{u}$ is the mass-weighted average velocity of the fluid mixture, defined as:

$$\boldsymbol{u} = \sum_{k=1}^{N} Y_k \boldsymbol{u}_k \tag{2.2}$$

where, $\boldsymbol{u}_k$ is the flow velocity of species k.

Momentum conservation

$$\frac{\partial \boldsymbol{u}}{\partial t} + \boldsymbol{u}.\nabla \boldsymbol{u} = -\frac{1}{\rho}\nabla . \boldsymbol{P} \tag{2.3}$$

The stress tensor $\boldsymbol{P}$ is defined as follows:

$$\boldsymbol{P} = \left[p + \left(\frac{2}{3}\mu - \kappa\right)(\nabla \boldsymbol{u})\right]\boldsymbol{I} - \mu\left[(\nabla \boldsymbol{u}) + (\nabla \boldsymbol{u})^T\right] \tag{2.4}$$

Here, p is the hydrostatic pressure, μ is the molecular viscosity, κ is the bulk viscosity and $\boldsymbol{I}$ the unit tensor.

Species conservation

$$\frac{\partial \rho Y_i}{\partial t} + \nabla . (\rho \boldsymbol{u} Y_i) + \nabla . (\rho \boldsymbol{V}_i Y_i) = \omega_i \tag{2.5}$$

Here, $i = 1, .., N$ where N is the number of species in the mixture, Y_i is the ith species mass fraction, $\boldsymbol{V}_i$ is the diffusion velocity of species i and ω_i is the rate of change of species i. For further reference it is noted that the dimension of the source term is $kg_i\,m^{-3}s^{-1}$. The diffusion velocity is defined as follows:

$$\boldsymbol{u}_i = \boldsymbol{u} + \boldsymbol{V}_i \tag{2.6}$$

In words, $\boldsymbol{V}_i$ is the velocity of species i respective to the flow of the mixture, hence the definition 'diffusion velocity.' It is a complex equation consisting of several terms, including thermal diffusion, diffusion through pressure effects and diffusion through external forces acting differently on each species in the mixture. The complete equation can be obtained from ref. [63] and is derived using kinetic theory of dilute gases. For the sake of completeness it will be stated here, (without the the

external force term which is already ignored):

$$
\begin{aligned}
\nabla X_i \;=\; & \sum_{j=1}^{N} \left(\frac{X_i X_j}{D_{ij}} \right) (\boldsymbol{V}_j - \boldsymbol{V}_i) + \underbrace{(Y_i - X_i) \frac{\nabla p}{p}}_{pressure} \\
& + \underbrace{\sum_{j=1}^{N} \left[\left(\frac{X_i X_j}{\rho D_{ij}} \left(\frac{D_j^T}{Y_j} - \frac{D_i^T}{Y_i} \right) \right) \right] \frac{\nabla T}{T}}_{thermal}
\end{aligned}
\tag{2.7}
$$

Here, X_i is the mole fraction of species i, D_{ij} is the diffusion coefficient of species i with respect to species j, T is the temperature and D_i^T is the thermal diffusion coefficient of species i. The diffusion velocities obey the following identity:

$$
\sum_{i=1}^{N} Y_i \boldsymbol{V}_i = 0
\tag{2.8}
$$

However, usually Fick's diffusion law is is used:

$$
Y_i \boldsymbol{V}_i = -D_{ij} \nabla Y_i
\tag{2.9}
$$

Fick's law is valid if the mixture is binary, thermal diffusion is negligible, body forces are identical for species i and j and if the molecular masses of both species are the same or the pressure is constant [63].

The chemical source term ω_i is defined in greatest detail using a detailed reaction mechanism. This mechanism consists of a large number of elementary reactions of which the reaction rate is a function of temperature, pressure and the involving species. Each elementary reaction is described in general as follows:

$$
\nu''_{1r} A_1 + \nu''_{2r} A_2 + .. + \nu''_{Nr} A_N \rightleftharpoons \nu'_{1r} A_1 + \nu'_{2r} A_2 + .. + \nu'_{Nr} A_N
\tag{2.10}
$$
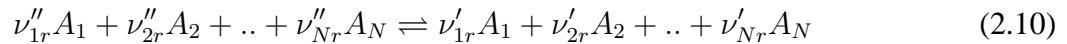
where subscript r denotes the rth reaction, A_j is a species and ν''_{jr}, ν'_{jr} are the stoichiometric coefficients of the forward and backward reaction of species j in reaction r, respectively. The reaction rate is a function of the species involved in the reaction, pressure and temperature. For a single species i the production rate ω_i is the sum of the production rates of the species in the elementary reactions it is involved in (This only holds for *elementary* reactions):

$$
\omega_i = M_i \sum_{r=1}^{R} (\nu''_{ir} - \nu'_{ir}) \left(k_r^f \prod_{n=1}^{N} [A_n]^{\nu'_{nr}} - \frac{k_r^f}{K_r^c} \prod_{n=1}^{N} [A_n]^{\nu''_{nr}} \right)
\tag{2.11}
$$

In this expression, R is the number of reactions, $[A_n]$ is the molar concentration of species n, k_r^f is the forward reaction rate of reaction r and K_r^c is the equilibrium constant of species i. The reaction rate is described by an Arrhenius expression for which the coefficients are tabulated in the reaction mechanism file. Reaction rates are sometimes enhanced with pressure terms and third-body reaction collision efficiencies.

Energy conservation

$$\rho \frac{\partial e}{\partial t} + \rho \boldsymbol{u}.\nabla e = -\nabla.\boldsymbol{q} - \boldsymbol{P} : (\nabla \boldsymbol{u}) \tag{2.12}$$

Here, e is the internal energy and $\boldsymbol{q}$ is the heat flux vector. The two dots (:) imply that the tensors are to be contracted twice to create a scalar. The heat flux tensor, $\boldsymbol{q}$ is described by:

$$\boldsymbol{q} = -\lambda \nabla T + \rho \sum_{i=1}^{N} h_i Y_i \boldsymbol{V}_i + R_g T \sum_{i=1}^{N} \sum_{j=1}^{N} \left(\frac{X_j D_j^T}{M_j D_{ij}} \right) (\boldsymbol{V}_i - \boldsymbol{V}_j) + \boldsymbol{q}^{rad} \tag{2.13}$$

where λ is the thermal conductivity, h_i is the specific enthalpy of species i, R_g is the universal gas constant, M_i the molar mass of species i and $\boldsymbol{q}^{rad}$ the radiation flux vector. These expressions are completed with the equation of state, the ideal gas law:

$$p = \frac{\rho R_g T}{\overline{M}} \tag{2.14}$$

where $\overline{M}$ is the average molar mass of the mixture:

$$\overline{M} = \frac{1}{\sum_{i=1}^{N} \frac{Y_i}{M_i}} \tag{2.15}$$

Furthermore, the internal energy is related to the enthalpy, h via:

$$e = h - \frac{p}{\rho} \tag{2.16}$$

and where h is defined as:

$$h = \sum_{i=1}^{N} h_i Y_i \tag{2.17}$$

and, finally, the specific enthalpy is defined through the caloric equation of state:

$$h_i = h_i^0 + \int_{T_0}^{T} c_{p,i} (\zeta) \, d\zeta \tag{2.18}$$

where $c_{p,i}$ is the specific heat and h_i^0 is the enthalpy of formation of species i at temperature T_0

2.2 General assumptions

In order to obtain a workable set of equations, in the simulation of turbulent combustion, some assumptions are usually made:

- Lewis number unity for all species

- Ignore thermal diffusion

- Ignore pressure diffusion

- Ignore bulk viscosity

- Trace species approximation

- Constant mean molar mass

- Low Mach number flow

- Pressure derivatives with respect to time are ignored

The low-mach number approximation and ignoring the pressure time derivatives are done to simplify the conservation equation of internal energy, which is rewritten to a conservation equation of the enthalpy using the unity Lewis number approximation, which is defined as:

$$\text{Le} = \frac{\lambda}{\rho D_{im} c_p} \equiv 1 \tag{2.19}$$

In many gases Le is very nearly unity, it is often slightly less than unity in combustible gas mixtures [63]. The Lewis number unity assumption is also very helpful in the derivation of the CFI-combustion model, as will be shown further on. It is assumed that this assumption holds in combustion simulations involving methane or natural gas to air. The bulk viscosity κ is zero only in monoatomic gas mixtures, however assuming it generally zero is almost always done, κ is negligible in combustion processes. The trace-species approximation yields $\boldsymbol{V}_i = \boldsymbol{V}$. It assumes there is one abundant species, replacing the binary diffusion coefficient D_{ij} with an effective diffusion coefficient D_{im} of species i into bulk species m. Ideally, this species m should be treated differently for consistency, otherwise the identity 2.8 is violated. Nevertheless this is rarely done, and the results may be acceptable if the degree of violation is not too great [63]. The trace species approximation leads to the assumption of constant mean molar mass, the abundant species prevents large deviations from the mean value. In atmospheric methane-air combustion for instance these assumptions hold because of the abundance of nitrogen.

These assumptions lead to the following transport equations:

Continuity

$$\frac{\partial \rho}{\partial t} + \nabla . \left(\rho \boldsymbol{u} \right) = 0 \tag{2.20}$$

Momentum conservation

$$\frac{\partial \rho \boldsymbol{u}}{\partial t} + \boldsymbol{u} . \nabla \left(\rho \boldsymbol{u} \right) - \nabla . \left(\mu \nabla \boldsymbol{u} \right) + \nabla p = 0 \tag{2.21}$$

Species conservation

$$\frac{\partial \rho Y_i}{\partial t} + \nabla . \left(\rho \boldsymbol{u} Y_i \right) = \nabla . \left(\rho D_{im} \nabla Y_i \right) + \omega_i \tag{2.22}$$

Enthalpy conservation

$$\frac{\partial \rho h}{\partial t} + \nabla.\left(\rho \boldsymbol{u} h\right) - \nabla.\left(\rho D_{im}\nabla h\right) = q^{rad} \tag{2.23}$$

2.3   Turbulent combustion

Together with the ideal gas law, expressions (2.20)-(2.23) describe the combustion of gases. However, their use is mostly restricted to laminar computations [23]. Examples of standard available codes for the solution of zero- or 1-dimensional laminar flames are PREMIX [28] and RUN-1DL [53]. The time-dependent solution of a turbulent flame using a detailed chemical reaction mechanism is still not feasible. Firstly, the amount of memory necessary for the simulation exceeds the available storage space of all but the most advanced computing systems available. It is a well-known rule that the memory requirements, A, of a turbulent *non-combusting* simulation grow as (see e.g. [47]:

$$A \sim \mathrm{Re}^{\frac{9}{4}} \tag{2.24}$$

where Re is the Reynolds number of the flow which is an indicator of the level of turbulence in a flow, defined by

$$\mathrm{Re} = \frac{UD\rho}{\mu} \tag{2.25}$$

Here, U is a characteristic velocity of the flow, D a characteristic diameter. For most industrial combustors, Re is 10^5 or higher, yielding a memory requirement of approximately 5 Tb *per time step* for a 32 bit-machine. For sufficient statistics at least a few seconds of a turbulent flow need to be solved, with time steps in the order of, say, 10^{-3} s as a rough estimate (most industrial combustors have residence times in the order of tens of milliseconds, so this is a very conservative estimate), yielding a memory requirement in the order of $5 \cdot 10^3$ Tb ($5 \cdot 10^{15}$ byte). For a combusting flow field, additional to the turbulent simulation, at each solution point of the simulation the temperature, enthalpy and species mass fractions need to be stored too. This multiplicates the memory requirement with a further factor of about 10. This is also based on the conservative assumption that the smallest length scales of the problem are not reduced by introducing combustion into the turbulent simulation. This makes such a calculation beyond the reach of even the most advanced supercomputer.

Secondly, such a detailed computation, if possible, would take an enormous amount of time to solve. State of the art turbulent combustion simulations, with a very small chemical reaction mechanism and small domains with very simple geometries, take in the order of years of wall-clock time to complete on a modern-day engineering workstation [8].

There are two basic issues involved why these expressions cannot directly be solved: The number of equations and their stiffness. As can be seen from the set of expressions that describe turbulent combustion, (2.20) - (2.23), most of the transport equations describe species transport, considering that a detailed reaction mechanism consists of tens to hundredths of species. Reducing this number means a direct reduction in the computational effort and the necessary memory requirement.

Stiffness is defined by the separation that exists in the scales of a problem. Turbulent combustion is characterized by very fast and very slow processes, meaning it is a stiff process. If one wants to solve such a flow problem numerically, a resolution is needed of the order of the smallest scale in the

problem, even if one is only interested in its large-scale behavior. If the smallest scales are removed from the computation, this significantly reduces the stiffness of the computation, relaxing the memory requirement of expression (2.24) considerably and reducing the time effort for the computation. However, if the influence of the removed scales onto the remaining ones is significant, it should be taken into account to acquire a reasonable accuracy. This influence then needs to be expressed in known variables to yield a closed set of equations. This is the task of turbulence and combustion models. In general it can be remarked that turbulence and combustion models simplify the transport equations and reduce their stiffness at the expense of reduced validity.

Concluding, to be able to solve equations (2.20)-(2.23) in a time-efficient manner, further simplifications are necessary, in the form of turbulence and combustion models. This means that one has to consider what one desires from the simulation. With time-efficient then is meant that the effort of the simulation - and hence the degree of simplification - should be balanced to the quality and quantity of results that is desired. For this reason, several simplifications to the governing expressions are devised, additional to those mentioned in section 2.2, resulting in the need to model the effect of the details that are left out to the result of the simulation. For turbulence, the Reynolds averaging approach is adopted here since it is the least computationally demanding level of modeling whilst retaining sufficient accuracy. Also, models that employ Reynolds averaging has received an enormous amount of attention which means their strengths and limitations are quite well-known. For these reasons, the standard $k - \varepsilon$ model will be used. To account for combustion, the CFI combustion model, developed at the laboratory of Thermal Engineering of the University of Twente, will be used. This model reduces the number of transport equations considerably and removes stiffness from the remaining equations while still retaining the detailed chemistry description. To accomplish this, the CSP algorithm for globally reduced chemical mechanisms is introduced [44]. These methods will be described below.

2.4 Turbulence Modeling: The $k - \varepsilon$ model

In the numerical description of turbulence, 3 classes of numerical tools exist: DNS or Direct Numerical Simulation, LES or Large Eddy Simulation and RaNS or Reynolds averaged Navier Stokes Simulations, ordered in increasing degree of simplification.

In DNS, in principle no modeling is applied, all the equations are solved in full. Because of the great detail of the results and their accuracy DNS simulations are often seen as 'numerical experiments.' However, full DNS without simplifications in turbulence and in combustion have not been performed yet on realistic fuels. In literature simulations are reported of 'DNS' of combustion. However, the DNS-part refers to the description of the momentum equations, and almost always (with the exception of small reaction schemes of species such as ozone) simplified models of combustion are employed [23]. Also, assumptions are made with respect to the influence of combustion on the smallest time scales of the problem.

In LES, only the larger scales of turbulence are taken into account, the interactions of the smaller scales with the larger scales are modeled. The smaller scales are filtered out using a filtering operation. The interaction of these scales to the larger scales is taken into account in a 'subgrid-scale' model. For a detailed discussion on this subject, LES and DNS, the reader is referred to ref. [18]. LES is becoming an increasingly used tool to describe turbulence in a combusting flow, however, it is still a very time- and computationally demanding calculation. An overview on the various implementations

of LES in turbulent combustion calculations is given in ref. [23]. Both DNS and LES are not adopted here since they are too computationally demanding for the solution of realistic fuels in industrial combustors. Instead the RaNS approach is used.

When all but the largest scales are filtered from the momentum transport equations, the resulting equations are called the Reynolds averaged Navier-Stokes equations, or RaNS. The equations are filtered over an infinite timeframe, and the filtering equation becomes (here T denotes a timeframe):

$$\overline{\phi} = \lim_{T \to \infty} \frac{1}{T} \int_0^T \phi\left(\boldsymbol{x}, t\right) dt \tag{2.26}$$

Using this definition, a scalar ϕ can be decomposed in its mean and a fluctuating part:

$$\phi\left(\boldsymbol{x}, t\right) = \overline{\phi}\left(\boldsymbol{x}\right) + \phi'\left(\boldsymbol{x}, t\right) \tag{2.27}$$

For a statistically stationary process, a time (or space) average may be replaced by a statistical *ensemble* average. The steady-state operation of continuous-flow combustors may be considered to stationary [63]. Under this assumption, a time-average may be seen as an ensemble average. The mean of a scalar ϕ is then defined as:

$$\overline{\phi} = \int_{-\infty}^{\infty} \phi P\left(\phi\right) d\phi \tag{2.28}$$

In this expression, P is the probability density function. The integral of this function represents the probability of the variable to be in the range of the integrand:

$$P(\phi_0 < \phi < \phi_1) = \int_{\phi_0}^{\phi_1} P(\phi') \mathrm{d}\phi' \tag{2.29}$$

Also, for $\phi_0 \to -\infty$ and $\phi_1 \to \infty$ the integral is one. The variance σ or standard deviation of the scalar is defined as:

$$\begin{aligned} \overline{\phi'^2} = \sigma^2 = \int_{-\infty}^{\infty} \phi'^2 P\left(\phi\right) d\phi &= \int_{-\infty}^{\infty} \left(\phi - \overline{\phi}\right)^2 P\left(\phi\right) d\phi \\ &= \overline{\phi\phi} - \overline{\phi}\,\overline{\phi} \end{aligned} \tag{2.30}$$

Accordingly, the nth moment of a scalar is defined as:

$$\overline{\phi'^n} = \int_{-\infty}^{\infty} \left(\phi - \overline{\phi}\right)^n P\left(\phi\right) d\phi$$

This averaging procedure can be applied to the momentum equations, leading to the RaNS equations. However, in combustion problems, another definition of the departure from the mean of a scalar is often used, called the Favre- or density-weighed mean:

$$\phi = \widetilde{\phi} + \phi" \tag{2.31}$$

The tilde here notices a Favre-averaged variable, defined by:

$$\widetilde{\phi} = \frac{\overline{\rho\phi}}{\overline{\rho}} \tag{2.32}$$

By definition, $\overline{\rho\phi"} = 0$ but $\overline{\phi"} \neq 0$.

2.4.1 Momentum equations

Applying the Favre decomposition on the velocities of the momentum conservation equation (2.21) and the Reynolds decomposition on the density and pressure yields:

$$\widetilde{\boldsymbol{u}}.\nabla\left(\overline{\rho}\widetilde{\boldsymbol{u}}\right) - \nabla.\left(\mu\nabla\widetilde{\boldsymbol{u}}\right) + \nabla\overline{p} = \nabla.\boldsymbol{\tau} \tag{2.33}$$

Here, a stress tensor $\boldsymbol{\tau}$ appears which is called the "Reynolds stress tensor":

$$\boldsymbol{\tau} = \overline{\rho\boldsymbol{u}"\boldsymbol{u}"} \tag{2.34}$$

This tensor is unknown and needs to be expressed into known flow variables. It contains the influence of all filtered scales on the averaged variables. This removes the stiffness arising from these scales but puts a heavy burden on the modeling of this tensor in that the interaction of all these scales to the remaining flow properties needs to be taken into account in a model that is simpler than the original expressions. In the past, a lot of different methods have been devised, the most widely used of these being the range of $k - \varepsilon$ models. The degree of modeling is usually defined by the order of moments (defined by expression (2.31)) that are used to close the set of expressions. The $k - \varepsilon$ closure is a first order moment closure, second order moment closures devise transport equations for the Reynolds stress tensor. For a discussion on higher order moment closures the reader is referred e.g. to ref. [48].

The $k-\varepsilon$ closure, although several varieties of its implementation exist, is based on the description of the Reynolds stress tensor as a function of k and ε and defining transport equations for both scalars. The turbulent kinetic energy, k, is defined as:

$$k = \frac{1}{2}\widetilde{\boldsymbol{u}"\boldsymbol{u}"} \tag{2.35}$$

and the viscous dissipation, ε:

$$\varepsilon \equiv \frac{\mathrm{d}k}{\mathrm{d}t} \tag{2.36}$$

The Boussinesq hypothesis is used which states that the Reynolds stress tensor scales with the gradient of the mean velocity. A turbulent viscosity μ_T is introduced which is the proportionality constant of $\boldsymbol{\tau}$ to the mean velocity gradient:

$$\boldsymbol{\tau} = -\mu_T\overline{\rho}\left(\nabla\widetilde{\boldsymbol{u}} + (\nabla\widetilde{\boldsymbol{u}})^T\right) + \frac{2}{3}\left(\overline{\rho}k + \mu_T\nabla.\widetilde{\boldsymbol{u}}\right)\boldsymbol{I} \tag{2.37}$$

where k arises from the static part of the turbulence stress tensor and is often ignored. Boussinesq used the assumption that the turbulent viscosity μ_T is, like its molecular counterpart, a product of a characteristic length scale and a characteristic velocity. Taking as length scale the turbulence integral length scale and as velocity the variance of the velocity fluctuations, $\sqrt{\boldsymbol{u}"\boldsymbol{u}"}$, dimensional analysis then shows that μ_T scales with:

$$\mu_T \sim \frac{k^2}{\varepsilon} = C_\mu\frac{k^2}{\varepsilon} \tag{2.38}$$

where C_μ is a proportionality constant. The transport equations for k and ε are defined as follows [27], ignoring buoyancy effects:

$$\rho\boldsymbol{u}.\nabla k = \nabla.\left(\left(\frac{\mu_T}{\sigma_k} + \mu\right)\nabla k\right) - \boldsymbol{\tau}\nabla.\widetilde{\boldsymbol{u}} - \overline{\rho}\varepsilon \tag{2.39}$$

$$\rho\boldsymbol{u}.\nabla\varepsilon = \nabla.\left(\left(\frac{\mu_T}{\sigma_\varepsilon}+\mu\right)\nabla\varepsilon\right) - C_1\frac{\varepsilon}{k}\boldsymbol{\tau}\nabla.\widetilde{\boldsymbol{u}} - C_2\overline{\rho}\frac{\varepsilon^2}{k} \tag{2.40}$$

In these equations, the modeling constants C_μ, σ_k, σ_ε, C_1 and C_2 appear. The values of the model constants that are used in this thesis are summarized in table 2.1 [4].

Symbol	Value
C_μ	0.09
σ_k	1.0
σ_ε	1.3
C_1	1.44
C_2	1.92

Table 2.1: Model Constants of the $k - \varepsilon$ model

2.4.2   Scalar transport equations

Using expression (2.31) in expression (2.22), and assuming that, like for a species Y_i, a generic scalar transport equation can be solved with its specific properties such as scalar diffusivity, the following expression arises (cf [59]:

$$\nabla.\left(\overline{\rho}\widetilde{\boldsymbol{u}}\widetilde{\phi}\right) - \nabla.\left(\overline{\rho}D\nabla\widetilde{\phi}\right) = -\nabla\overline{p} - \nabla.\boldsymbol{\tau}' + \overline{\omega} \tag{2.41}$$

From this expression, a tensor $\boldsymbol{\tau}'$ arises which constitutes the interaction of the filtered scales to the resolved flow properties. It is the turbulent scalar flux, defined by:

$$\boldsymbol{\tau}' = \overline{\rho\boldsymbol{u}"\phi"} \tag{2.42}$$

This term is also modeled using a gradient assumption:

$$\boldsymbol{\tau}' = -\frac{\mu_T}{\mathrm{Sc}_T}\nabla\widetilde{\phi} \tag{2.43}$$

Here, Sc is the turbulent Schmidt number of the scalar. Usually it is set to 0.9, which is also done here, but its value can vary from case to case, depending on the type of flow that is solved. It should be noted that when countergradient turbulent transport is significant, this model might not be adequate anymore. However, in the simulations reported here expression (2.43) is presumed to hold.

A transport equation for the variance $\widetilde{\phi"^2}$ of a scalar can be created by multiplying expression (2.22), for a scalar ϕ, with $\phi"$ and subsequently average the result [59]:

$$\nabla.\left(\overline{\rho}\widetilde{\boldsymbol{u}}\widetilde{\phi"^2}\right) - \underbrace{\nabla.\overline{(\rho D\nabla\phi"^2)}}_{1} = \underbrace{\overline{2\phi"\nabla.\left(\rho D\nabla\widetilde{\phi}\right)}}_{2} - \underbrace{2\overline{\rho\boldsymbol{u}"\phi"}.\nabla\widetilde{\phi}}_{3}$$
$$- \underbrace{2\overline{\rho D\nabla\phi"\nabla\phi"}}_{4} + \underbrace{2\overline{\omega\phi"}}_{5} \tag{2.44}$$

In this expression, terms 1 and 2 are expected to be small in large Reynolds number flows and are usually ignored [59]. Term 3 contains a turbulent scalar flux which is modeled using expression (2.43). Terms 4 is the fluctuating part of the scalar dissipation rate which is a key concept of turbulent combustion [59]. Here it is modeled as follows, see ref. [14] for details:

$$2\overline{\rho D \nabla \phi" \nabla \phi"} = \overline{\rho} R_T \frac{\varepsilon}{k} \widetilde{\phi"^2} \tag{2.45}$$

The proportionality constant R_T is usually set to 2, however, Durbin *et al.* [14] mention that in the presence of a uniform mean scalar gradient R_T is found to be approximately 1.5; in the decay of isotropic turbulence a varying value of 1 to 3 is found. Here R_T will be assumed to be constant at 2.0. Term 5 can be described in values of the mean of the scalar only:

$$\overline{\phi" \omega} = \overline{\phi \omega} - \widetilde{\phi} \overline{\omega} \tag{2.46}$$

This expression can only be solved directly if the relation $\overline{\phi \omega}$ is known. In the CFI combustion model this is the case, as will be shown further on in this thesis.

2.5 The CSP algorithm for globally reduced mechanisms

One of the methods that are often used to reduce the number of transport equations is the introduction of steady-state relations for some of the species in the kinetic mechanism. These relations apply when the chemical system is stiff, i.e. consists of fast and slow timescales, and when the fastest chemical time scales can be related to these species. The chemical action then moves along the domain dictated by the slow timescales, any perturbation off this domain will quickly decay due to the action of the fast timescales [44]. This domain is a manifold which can be spanned by basis vectors consisting of only a part of the complete domain and is usually referred to as the *low-dimensional manifold*. The CSP algorithm is a method to specify the low-dimensional manifold and identify the species associated with the fastest chemical timescales, the steady-state species.

Suppose a detailed reaction mechanism is used with N species consisting of E elements which are interacting in R reactions. A N-dimensional orthonormal basis can be defined in species space, consisting of 3 sets of linearly independent column basis vectors $\boldsymbol{a}_i$, $i = 1, .., N$:

$$[\boldsymbol{a}] = [\boldsymbol{a}_1, \boldsymbol{a}_N] = [\boldsymbol{a}_r, \boldsymbol{a}_s, \boldsymbol{a}_c] \tag{2.47}$$

Where

$$\boldsymbol{a}_r = [\boldsymbol{a}_1, .., \boldsymbol{a}_M] \tag{2.48}$$
$$\boldsymbol{a}_s = [\boldsymbol{a}_{M+1}, .., \boldsymbol{a}_{N-E}] \tag{2.49}$$
$$\boldsymbol{a}_c = [\boldsymbol{a}_{N-E+1}, .., \boldsymbol{a}_N] \tag{2.50}$$

There are M vectors $\boldsymbol{b}_j^r$, $S = N - M - E$ vectors $\boldsymbol{b}_j^s$ and E vectors $\boldsymbol{b}_j^c$. From this set of basis vectors $\boldsymbol{a}$ a dual set of row vectors $\boldsymbol{b}$ can be defined:

$$\boldsymbol{b}^r = [\boldsymbol{b}^1, .., \boldsymbol{b}^M]^T \tag{2.51}$$
$$\boldsymbol{b}^r = [\boldsymbol{b}^{M+1}, .., \boldsymbol{b}^{N-E}]^T \tag{2.52}$$
$$\boldsymbol{b}^c = [\boldsymbol{b}^{N-E+1}, .., \boldsymbol{b}^N]^T \tag{2.53}$$

For these vectors the following holds by definition:

$$\boldsymbol{b} \cdot \boldsymbol{a} = \boldsymbol{I} \Leftrightarrow \boldsymbol{b} = \boldsymbol{a}^{-1} \tag{2.54}$$

In these expressions, b_{ij} is has dimensions $\frac{g_i}{g_j}$. In the molar sense, $\widehat{b}_{ij}$ is used, which has dimensions $\widehat{b}_{ij} = \frac{\text{Mol}_i}{\text{Mol}_j}$. They are related as follows:

$$\widehat{b}_{ij} = \frac{\text{Mol}_i}{\text{Mol}_j} = \frac{M_j}{M_i} b_{ij} \tag{2.55}$$

Expanding expression (2.22) on the basis of these vectors leads to:

$$\frac{\partial Y_i}{\partial t} = \boldsymbol{L}(\boldsymbol{Y}) + \boldsymbol{a}_c \boldsymbol{f}^c + \boldsymbol{a}_r \boldsymbol{f}^r + \boldsymbol{a}_s \boldsymbol{f}^s \tag{2.56}$$

where $\boldsymbol{L}$ denotes the convection-diffusion operator of expression (2.22), and:

$$\boldsymbol{f}^c = \boldsymbol{b}^c \cdot \boldsymbol{\omega} \tag{2.57}$$
$$\boldsymbol{f}^r = \boldsymbol{b}^r \cdot \boldsymbol{\omega} \tag{2.58}$$
$$\boldsymbol{f}^s = \boldsymbol{b}^s \cdot \boldsymbol{\omega} \tag{2.59}$$

The reaction rate ω_i can be expressed as:

$$\omega_i = \frac{1}{\rho} M_i \sum_{r=1}^{R} \boldsymbol{S}_r R^r \tag{2.60}$$

In this expression M_i is the molar mass of species i, R^r is the reaction rate of the rth elementary reaction. $\boldsymbol{S}_r$ is its stoichiometric vector, where S_{ri} contains the molar participation of species i in reaction r. For example, suppose the species vector is described by

$$[O, H, OH, HO_2, H_2O]^T$$

and reaction r is:

$$O + H \rightleftharpoons OH$$
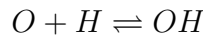
then

$$\boldsymbol{S}_r = [-1, -1, 1, 0, 0]^T$$

Following the example, suppose $\widehat{\boldsymbol{b}}_c^e$ is the eth species molar element composition vector, suppose for species O:

$$\widehat{\boldsymbol{b}}_c^e = [1, 0, 1, 2, 1]$$

It easily follows that $\widehat{\boldsymbol{b}}_c^e \cdot \boldsymbol{S}_j = 0$. This is true for all $r = 1, .., R$ and all elements $e = 1, .., E$ in the chemical reaction mechanism. In other words:

$$\boldsymbol{f}^c \equiv \boldsymbol{0} \tag{2.61}$$

Now suppose that, under some conditions, the movement of the system (2.56) takes place only in the subspace defined by the basis vectors a^s and its dual basis b_s. This means that the contributions in the directions orthogonal to this manifold are negligible. Expression (2.56) becomes:

$$
\begin{aligned}
\frac{\partial \boldsymbol{Y}}{\partial t} &\simeq \boldsymbol{L}(\boldsymbol{Y}) + \boldsymbol{a}_s \boldsymbol{f}^s \\
\boldsymbol{f}^c &= \boldsymbol{0} \\
\boldsymbol{f}^r &\simeq \boldsymbol{0}
\end{aligned}
\tag{2.62}
$$

The subspace defined by a^s and b_s is referred to as the low-dimensional manifold in species space. The scales associated with b^r are associated with *fast* processes. Any perturbation off the low-dimensional manifold will quickly decay due to these fast processes [44]. Multiplying expressions (2.62) with b leads to:

$$
\begin{aligned}
\frac{\partial \boldsymbol{\eta}^s}{\partial t} &\simeq \boldsymbol{L}(\boldsymbol{\eta}^s) + \boldsymbol{f}^s \\
\frac{\partial \boldsymbol{\eta}^c}{\partial t} &= \boldsymbol{L}(\boldsymbol{\eta}^c) \\
\boldsymbol{b}^r \cdot \boldsymbol{\omega} &\simeq \boldsymbol{0}
\end{aligned}
\tag{2.63}
$$

where $\boldsymbol{\eta}^s = \boldsymbol{b}^s \boldsymbol{Y}$ and $\boldsymbol{\eta}^c = \boldsymbol{b}^c \boldsymbol{Y}$. Since a is an orthonormal basis, the elements of $\boldsymbol{\eta}^s$ are linearly independent, also the vector $\boldsymbol{\eta}^s$ is linearly independent of the fast subspace. It should be noted that it is assumed here that the matrices a and b have to be invariant with respect to space and time for this expression to be valid. Also, the equal diffusivity assumption is used. When this is the case, expressions (2.63) describe a globally reduced reaction mechanism. If this is not the case, these expressions will contain derivatives of b with respect to space and time, or expressions (2.62) should be used.

2.5.1 Local CSP

Suppose that at a point in space, for a time-independent flow, a suitable set of orthogonal basis vectors a_0 and its dual basis b^0 can be defined. Let $\boldsymbol{J}$ be the jacobian of $\boldsymbol{\omega}$:

$$
J_{ij} = \frac{\partial \omega_i}{\partial Y_j}
\tag{2.64}
$$

Then the *first CSP iteration* produces a *local* set of basis vectors b (see ref. [44]):

$$
\begin{aligned}
\boldsymbol{a}^r &= \boldsymbol{J} \boldsymbol{a}_{r0} \boldsymbol{\tau}_0^0 \tag{2.65} \\
\boldsymbol{\tau}_0^0 &= \left[\boldsymbol{b}^{r0} \boldsymbol{J} \boldsymbol{a}_{r0}\right]^{-1} \tag{2.66} \\
\boldsymbol{a}^s &= \left[\boldsymbol{I} - \boldsymbol{a}_r \boldsymbol{b}^r\right] \boldsymbol{a}_{so} \tag{2.67} \\
\boldsymbol{b}^r &= \boldsymbol{\tau}^0 \boldsymbol{b}^{r0} \boldsymbol{J} \tag{2.68} \\
\boldsymbol{\tau}^0 &= \left[\boldsymbol{b}^{r0} \boldsymbol{J} \boldsymbol{a}_r\right]^{-1} \tag{2.69} \\
\boldsymbol{b}^s &= \boldsymbol{b}^{s0} \left[\boldsymbol{I} - \boldsymbol{a}_r \boldsymbol{b}^{r0}\right] \tag{2.70}
\end{aligned}
$$

Now, the M components of $\boldsymbol{Y}$ that

1. are most influenced by the M fastest timescales

2. exhibit strong participation in the M $\boldsymbol{f}^r \simeq \boldsymbol{0}$ relations

are considered to be the best candidates for steady-state species. The first item requires a strong projection of $\boldsymbol{a}_i$, $i = 1, .., M$, on the axis of species Y^k, $\boldsymbol{e}^k$:

$$\frac{1}{Y^k} \left(\boldsymbol{e}^k \cdot \boldsymbol{a}_i \right)$$

The second item yields a large projection of $\boldsymbol{e}^k$ on $\boldsymbol{b}^i$, $i = 1, .., M$:

$$Y^k \left(\boldsymbol{b}^i \cdot \boldsymbol{e}^k \right)$$

Combined, the M species which are assumed to be in steady state are the ones with the largest value of $\left[\frac{1}{Y^k} \left(\boldsymbol{e}^k \cdot \boldsymbol{a}_i \right) \right] \left[Y^k \left(\boldsymbol{b}^i \cdot \boldsymbol{e}^k \right) \right] = b_k^i a_i^k$, $k = 1, .., M$ are the optimal choice of species assumed to be in local steady-state. The trace elements of $\boldsymbol{b}^r \cdot \boldsymbol{a}_r$, normalized to sum to 1, and are called the *local CSP-pointers* D^i, $i = 1, .., N$:

$$\boldsymbol{D} = \frac{\text{Diag} \left(\boldsymbol{a}_i \boldsymbol{b}^i \right)}{\sum_{i=1,N} b_k^i a_i^k} \tag{2.71}$$

It must be noted that local CSP involves more than 1 refinement. For details see e.g. [44].

2.5.2   Global CSP

The M largest CSP pointers define the M local steady-state species. In a steady-state flow, at each location there will be different species that are pointed, both in number and in specification. To be able to construct a globally reduced mechanism, this local knowledge must be interpreted on a more global scale and the choice of steady-state species be constant. This process enlarges the generality of the reduction at the cost of its accuracy.

First, the number of steady-state species, M, is fixed. Then, a detailed steady-state laminar flame solution is needed. At the moment, this is the solution of a 1-dimensional, freely propagating, perfectly premixed laminar flame, obtained using the RUN-1DL- [53] or the CHEMKIN PREMIX code [28]. At each solution point of this calculation, the local CSP pointers D_i are calculated. Then, the *integral CSP pointer* I^i is defined as:

$$I^i = \frac{1}{L} \int_0^L D^i \frac{1}{X_i + \epsilon_1} \frac{|\omega_i|}{|\omega_i^{max}| + \epsilon_2} \mathrm{d}x \tag{2.72}$$

This integral pointer integrates the local CSP pointer over the points in the solution where this species is present and its net production rate is meaningful [44]. In this expression, ϵ_1 and ϵ_2 are small numbers preventing a division by zero and $|\omega_i|^{max}$ is the maximum net production rate of species i in the computational domain. The M species with the largest value of I^i are selected as global steady-state species.

Suppose the species vector is ordered from fast to slow, in decreasing value of I^i. The matrix $\widehat{\boldsymbol{b}}^r$ is then defined as:

$$\widehat{\boldsymbol{b}}^r = \left[\boldsymbol{I}_{M \times M}, \boldsymbol{0}_{M \times N-M} \right] \tag{2.73}$$

where $\boldsymbol{I}_{M \times M}$ is a M by M unit matrix, containing the M steady-state species, and $\boldsymbol{0}_{M \times N-M}$ is a M by $N - M$ zero matrix. Subsequently, $\widehat{\boldsymbol{b}}^c$ is defined as the molar species element composition matrix and is usually fully populated. Then the complementary linearly independent $N - M - E$ row vectors are determined and stored in $\widehat{\boldsymbol{b}}^{s0}$. Then a new set of vectors $\widehat{\boldsymbol{b}}^s$ is computed from the relation [44]:

$$\widehat{\boldsymbol{b}}^s = \widehat{\boldsymbol{b}}^{s0} \left[\boldsymbol{I}_{N \times N} - \widehat{\boldsymbol{a}}_r \widehat{\boldsymbol{b}}^r \right] \tag{2.74}$$

In general, $\widehat{\boldsymbol{b}}^s$ is fully populated. Matrix $\widehat{\boldsymbol{a}}$ is then computed from:

$$\widehat{\boldsymbol{a}} = \left[\begin{array}{c} \widehat{\boldsymbol{b}}^r \\ \widehat{\boldsymbol{b}}^c \\ \widehat{\boldsymbol{b}}^s \end{array} \right]^{-1} = [\widehat{\boldsymbol{a}}_r \ \widehat{\boldsymbol{a}}_c \ \widehat{\boldsymbol{a}}_s] \tag{2.75}$$

A division can now be made of the species vector into M steady-state species and $N - M$ major species. These major species react in $S = N - M - E$ CSP-reactions, defined to leading order by the stoichiometric vectors $\widehat{\boldsymbol{a}}_j^s, j = 1, .., S$, and reaction rates $\boldsymbol{b}^s \cdot \boldsymbol{\omega}$. The corresponding low-dimensional manifold is defined by $\boldsymbol{\eta}^s$.

2.6   Turbulent combustion modeling: The CFI model

In turbulent combustion modeling, many different methods are devised to simplify the governing equations. Unfortunately, the separation into ranges of models is not as clear as in the modeling of turbulence, and a short description can therefore not easily be given.

Most models are designed specifically for the limiting cases of either fully premixed flames, or for diffusion flames. Models that cover both fields are rare. In a perfectly premixed flame, the flame front separates the perfectly mixed fuel and oxidizer from the combustion products, in a diffusion flame fuel and oxidized are separated by the flame front. Intermediate situations are partially premixed flames. There oxidizer may be present at the fuel side of a diffusion flame, or vice versa. Also fuel and air can be imperfectly mixed but still be separated from the products by the fuel front. Most industrial continuous-flow burners are partially premixed, consisting of separate fuel and air inlets which mix to some degree before reaching the flame front.

Almost all combustion models are developed within the framework of RaNS but most of these can be extended to LES or even DNS. This is allowed if the typical time scale of the combustion process is smaller than the time frame of averaging, meaning that it can be assumed to be in local equilibrium. If one assumes that the time scales of combustion are smaller than the Kolmogorov time scale which is the smallest scale in turbulence, these models can be extended to DNS.

Most combustion calculations are done using the assumption of adiabatic combustion. This removes the transport equation for enthalpy and replaces it with an identity equation, relating species mass fractions and pressure to temperature. If nonadiabatic effects are included, they are mostly to account for heat loss through emission of radiation.

2.6.1 Outline

In the CFI-combustion model, combustion is taken into account through reaction progress variables, c, mixing is taken into account through the use of a mixture fraction scalar, f and heat loss is incorporated through the dimensionless enthalpy scalar i. The model is based on an adiabatic combustion model which was developed by Janicka and Kollmann [20][21] for hydrogen-air diffusion flames. It was extended to cover CO-H_2 combustion by Correa [10]. Various changes have subsequently been made to the model at the University of Twente. Amongst others, heat loss through radiation was included for hydrogen-air flames [39], the model was converted to cover methane combustion as well [29][64], the second moment of the reaction progress variables and mixture fraction was taken into account [39] and heat loss for premixed methane-air flames was introduced [40].

All these models were based on the manual simplification of the chemistry involved which allowed only the use of very small reaction mechanisms with a reduced amount of species involved. The chemical reaction mechanism was reduced by introducing steady-state of species and partial equilibrium of reactions assumptions. The adequate representation of the reduced chemistry was done manually and with *ad hoc* assumptions. This was done to remove nonlinearities in the remaining transport equation source terms, which were seen to cause inaccuracies in the remaining turbulent transport equations. Here, the CSP algorithm for globally reduced mechanisms will be incorporated, allowing the use of arbitrarily large, detailed reaction mechanisms. It will be employed for the optimal representation of the reduced chemistry, based on considerations arising from the stiffness of the chemical system. It will also be used for the optimal selection of species assumed to be in steady-state. In all the previous models the number of scalars that account for combustion was fixed, in the present model this number is free to be set by the user. More, minor, modifications to the previous models were introduced and will be stated where appropriate.

The methodologies used to derive the CFI combustion model will be described here, for an in-depth discussion of the various techniques the reader is referred to refs. [7], [23] and [59]. The model presented here allows the solution of nonpremixed, partially premixed and fully premixed flows, with or without heat loss taken into account. It is applicable to LES, DNS and RaNS, although it is specifically designed for the RaNS framework on Favre-decomposed scalars. Using RaNS, the presumed decomposed PDF approach is used to describe the scalar probability density functions.

2.6.2 Derivation

Suppose a detailed reaction mechanism is used with N species consisting of E elements which are interacting in R reactions is reduced onto S reaction progress variables using M species steady-state approximations and E element conservation relations. Then the reduced system is described by expressions (2.63). Using the equal diffusivity assumption, the element mass fractions can be related to a single conserved scalar through algebraic relations and it suffices to create one transport equation of this conserved scalar. This conserved scalar is the mixture fraction, the relation to the element mass fractions is given by:

$$f = \frac{\eta_e^c - \eta_e^{c,in2}}{\eta_e^{c,in1} - \eta_e^{c,in2}} \quad , e = 1, .., E \tag{2.76}$$

where superscript $in1$ denotes the element mass fraction of inlet 1 and $in2$ of inlet 2 and $\eta_i = \sum_{i=1}^{N} b_{ij} Y_i$ as in expression 2.63. Most partially premixed and diffusion flames can be broken down

into 2 chemically different species mass flows, therefore 2 inlets are sufficient to describe most of these flows. For more than 2 chemically different flows, more mixture fraction scalars need to be devised, however it is assumed here that one mixture fraction is sufficient. Using this definition, the mixture fraction attains values between 0 and 1. Relations (2.76) are known as Schwab-Zeldovich variables [59]. The system of equations is now:

$$\frac{\partial \boldsymbol{\eta}^s}{\partial t} = \boldsymbol{L}\left(\boldsymbol{\eta}_s\right) + \boldsymbol{f}^s \tag{2.77}$$

$$\frac{\partial f}{\partial t} = \boldsymbol{L}\left(f\right) \tag{2.78}$$

$$\boldsymbol{b}^r \cdot \boldsymbol{\omega} = \boldsymbol{0} \tag{2.79}$$

$$\boldsymbol{\eta}^c = f \boldsymbol{\eta}^{c,in1} + (1 - f) \boldsymbol{\eta}^{c,in2} \tag{2.80}$$

A dimensionless scalar c_k can be defined from η_k^s by normalizing using its equilibrium (denoted by superscript eq) and 'unburnt' (denoted by superscript u) compositions:

$$c_k = \frac{\eta_k^s - \eta_k^{s,u}}{\eta_k^{s,eq} - \eta_k^{s,u}} = \frac{\eta_k^s - \eta_k^{s,u}}{W_k} \tag{2.81}$$

where W_k is the normalization function of the kth scalar, and:

$$\eta_k^{s,u} = \sum_{j=1}^{N} b_{kj}^s Y_j^u; \tag{2.82}$$

$$\eta_k^{s,eq} = \sum_{j=1}^{N} b_{kj}^s Y_j^{eq} \tag{2.83}$$

If in expression (2.81) $\eta_k^{s,eq}$ and $\eta_k^{s,u}$ denote the two extremes η_k can attain and if η_k^s is monotonic between these two, c_k becomes a scalar that moves between 0, the unburnt - mixed only - state and 1, the equilibrium state. Then, c_k can be interpreted as a reaction progress variable.

The unburnt mass fractions $\boldsymbol{\eta}_k^{s,u}$ are Schwab-Zeldovich variables:

$$\boldsymbol{\eta}^{s,u} = f \boldsymbol{b}^s \cdot \boldsymbol{Y}^{in1} + (1 - f) \boldsymbol{b}^s \cdot \boldsymbol{Y}_k^{in2} \tag{2.84}$$

The mixture fraction can be used directly to describe the unburnt species mass fractions since in definition (2.84) it is specified that these are not subject to reaction, but to convection and diffusion only and can therefore be created nor destroyed. Here, the assumption of equal diffusivity is used. In case of a perfectly premixed flame, the mixture fraction is presumed to be identically 1. Now, $\boldsymbol{\eta}^{s,eq}$ is defined as the composed equilibrium mass fraction of this unburnt mixture. This is a function of the available enthalpy at that position, h and of the mixture fraction through the unburnt mass fraction vector $\boldsymbol{Y}^u$:

$$\boldsymbol{\eta}^{s,eq} = \boldsymbol{\eta}_k^{s,eq}\left(\boldsymbol{Y}^u(f), h\right) = \boldsymbol{b}^s \cdot \boldsymbol{Y}^{eq}\left(f, h\right) \tag{2.85}$$

It is assumed that the enthalpy of the unburnt and equilibrium mixture is equal. The enthalpy can also be normalized, creating an enthalpy scalar i, which is defined as follows:

$$i = \frac{h - h^{min}}{h^{ad} - h^{min}} = \frac{h - h^{min}}{V} \tag{2.86}$$

where h^{ad} is the enthalpy of the mixture without heat loss, i.e. the adiabatic enthalpy. The minimum enthalpy of the system is defined by h^{min}, it is defined as the enthalpy of the combusted mixture when it is instantly cooled to T^0, the temperature of the environment:

$$h^{min} = h(\boldsymbol{Y}^{eq}, T^0) \tag{2.87}$$

This scalar i also moves between 1 - fully adiabatic - and 0 - complete heat loss - if h^{ad} and h^{min} are the extremes and h is monotonic between these values.

In expression (2.86), V is the normalization function for the enthalpy scalar. Both the minimum and the adiabatic enthalpy are functions of mixture fraction only. Hence, V is a function of mixture fraction and the normalization function W_k in expression (2.81) is a function of f and i, yielding for the definitions of c_k and i:

$$c_k = \frac{\eta_k^s - \eta_k^{s,u}}{W_k(f,i)} \tag{2.88}$$

$$i = \frac{h - h^{min}}{V(f)} \tag{2.89}$$

In previous models, W_k was not only a function of f and i but could also be a function of other scalars $c_j, j \neq k$. This dependence has been dropped here. A derivation where this is taken into account can be obtained in appendix B.

The transport equation for η_k^s in expression (2.77) can be converted into a transport equation for c_k. Substituting expression (2.81) into expression (2.77) yields:

$$\frac{\partial}{\partial t}\left(c_k W_k(f,i) + Y_k^u(f)\right) + \rho\boldsymbol{u}\nabla\left(c_k W_k(f,i) + Y_k^u(f)\right) =$$
$$\nabla.\left\{\rho D \nabla\left[c_k W_k(f,i) + Y_k^u(f)\right]\right\} + \omega_k \tag{2.90}$$

After rewriting this expression and dropping the subscript k, one yields for a transport equation for a reaction progress variable:

$$\frac{\partial \rho c}{\partial t} \quad + \quad \nabla.\left(\rho\boldsymbol{u}c\right) - \nabla.\left(\rho D \nabla c\right)$$
$$= \quad -c\frac{W_i}{W}S^i + \rho Dc\left(\nabla f\right)^2\frac{W_{ff}}{W} + \rho Dc\left(\nabla i\right)^2\frac{W_{ii}}{W}$$
$$+ \quad 2\rho Dc\nabla i\nabla f\frac{W_{if}}{W} + 2\frac{W_i}{W}\rho D\nabla i\nabla c + 2\rho D\nabla c\nabla f\frac{W_f}{W} + \omega^c \tag{2.91}$$

For a complete derivation of this expression, one is referred to Appendix B. In this expression, subscripts denote partial differentiation with respect to that variable. Also:

$$\omega^c = \frac{1}{W}\boldsymbol{b}^s \cdot \boldsymbol{\omega} \tag{2.92}$$

It should be noted that for a perfectly premixed, adiabatic flow, where $f \equiv 1$ and $i \equiv 1$, this expression reduces to:

$$\frac{\partial \rho c}{\partial t} + \nabla.\left(\rho\boldsymbol{u}c\right) - \nabla.\left(\rho D_{im}\nabla c\right) = \omega^c$$

which is the standard reaction progress variable transport equation for a premixed combusting flow, see e.g. ref. [59], only in this equation the chemical source term is described as a function of the detailed reaction mechanism, and needs therefore not be modeled.

The i-transport equation can be obtained by inserting expression (2.86) into expression (2.23). Rewriting results in (see also appendix B):

$$\frac{\partial \rho i}{\partial t} + \nabla . (\rho \boldsymbol{u} i) - \nabla . (\rho D \nabla i) = \rho D (\nabla f)^2 \frac{V_{ff}}{V} (i - 1) + 2 \rho D \nabla i \nabla f \frac{V_f}{V} - S^{\text{rad},i} \qquad (2.93)$$

where superscript rad denotes the radiation source term:

$$S^{\text{rad},i} = \frac{q^{rad}}{V} \qquad (2.94)$$

This means that the source term S^i of expression (2.91) is equal to:

$$S^i = \rho D (\nabla f)^2 \frac{V_{ff}}{V} (i - 1) + 2 \rho D \nabla i \nabla f \frac{V_f}{V} \qquad (2.95)$$

In the previous models both steady-state and partial equilibrium assumptions were employed to reduce the chemical system [10] [20] [21] [29] [39] [40] [64]. Analogous to the steady-state assumption for species, a partial equilibrium assumes that a particular *reaction* is so fast that it is always in equilibrium with respect to the other reactions. In this derivation, only steady-state assumptions of species are used. These used to be picked manually, but when the chemical reaction mechanism is large, this is an impossible task. For this task the CSP algorithm for globally reduced mechanisms is used in the present model, as described here.

Also, in previous models, the coefficients b^s_{kj} which define η^s_k were obtained manually . From a small chemical reaction mechanism, the coefficients were chosen in such a way that the remaining source terms contained the least possible number of reactions with large activation energies. These terms were eliminated from the reaction progress variable source term because they contained most of the nonlinearities of the composed species source term [39]. This can also be viewed as a means to remove the stiffness from the remaining transport equations, since the fast chemical reactions can be related to those with high activation energies. Here this is done automatically using the CSP algorithm for globally reduced mechanisms.

It should be noted that, since in this thesis only adiabatic calculations will be discussed, the matter of calculating the value of the radiation source term $S^{rad,i}$ will not be discussed here. How this is achieved in previous versions of the CFI-model can be obtained in refs. [39] and [29]. However, for completeness the source term will be taken into account in the derivations described here.

2.7 Favre-averaging the CFI-transport equations

To be able to use the CFI-combustion model in the Favre-averaged description of turbulent combustion, the expressions defining the model need to be Favre-averaged. Each scalar c_k, f and i is decomposed into a mean and its fluctuation according to expression (2.31) on page 16 of this thesis. Since

each scalar is a function of these variables, the ensemble Favre average of a scalar is subsequently defined as:

$$\widetilde{\phi} = \frac{1}{\overline{\rho}} \int_{c=0}^{1} \int_{f=0}^{1} \int_{i=0}^{1} \rho\phi\left(c, f, i\right) P\left(c, f, i\right) \mathbf{d}c \mathrm{d}f \mathrm{d}i \qquad (2.96)$$

Where $P\left(c, f, i\right)$ is the composed PDF of scalar ϕ. If the scalars are statistically independent, the covariances of the scalars are zero and the PDF can be simplified to:

$$P\left(c, f, i\right) = P\left(c\right) P\left(f\right) P\left(i\right) \qquad (2.97)$$

If these scalars are linearly independent and if they do not become correlated due to actions of the turbulent flow, they are also statistically independent. In this case these turbulence correlations are negligible and it suffices to describe single scalar PDF's. One of the methods to accomplish this is the use of PDF's of presumed shape. In premixed combustion, the β-function is often used as for the presumed shape of the PDF, and in diffusion flames this shape is often used to describe the PDF of the mixture fraction. Other shapes include combinations of Dirac δ-functions, for example. See refs. [7] and [59] for more details. The β-PDF for a scalar ϕ is defined as follows:

$$\beta(\phi; \widetilde{\phi}, \widetilde{\phi''^2}) = \frac{\phi^{a-1}\left(1-\phi\right)^{b-1}}{I} \quad , \quad a = \widetilde{\phi}\left(\frac{\widetilde{\phi}\left(1-\widetilde{\phi}\right)}{\widetilde{\phi''^2}} - 1\right)$$

$$, \quad b = \frac{1-\widetilde{\phi}}{\widetilde{\phi}}a$$

$$, \quad I = \int \phi^{a-1}\left(1-\phi\right)^{b-1}\mathrm{d}\phi \qquad (2.98)$$

in this equation, the integral can be written as the product of Gamma functions:

$$I = \frac{\Gamma\left(a\right)\Gamma\left(b\right)}{\Gamma\left(a+b\right)} \qquad (2.99)$$

These Gamma functions can be relatively easily calculated, it takes approximately the same amount of computational time as a calculation of e^x [49]. From this expression it follows that $a, b \geq 0$. The δ-PDF is defined as:

$$\delta(\phi; \widetilde{\phi}) = \begin{cases} 1, \widetilde{\phi} = \phi \\ 0, \widetilde{\phi} \neq \phi \end{cases} \qquad (2.100)$$

It follows from these definitions that for the β-PDF the mean and variance of the scalar ϕ should be known, and for the δ-PDF only its mean needs to be known. This means that the δ-PDF-Favre averaged quantity ϕ is presumed not to be influenced by turbulence fluctuations. Turbulence fluctuations are presumed to be influencing the β-PDF-Favre averaged quantity, this is modeled through the variance of that scalar. Here the β-function will be employed for the mixture fraction f and reaction progress variables c_k, the single δ-PDF will be used for the PDF of the enthalpy scalar i. The latter choice is made since it is believed that turbulent fluctuations do not influence this scalar significantly [40][29]. To be able to solve the turbulent transport equations, the means and variances of c and f need to be known as well as the mean of i. This is done by setting up transport equations for these

quantities, as described in section 2.4.2. For the CFI model this results in the following expressions, a complete derivation of these transport equations can be obtained in appendix B. The subscript k for a reaction progress variable is dropped, differencing towards a variable is denoted by a subscript of that variable:

Reaction progress variable, c

$$\nabla \cdot (\overline{\rho} \widetilde{\boldsymbol{u}} \widetilde{c}) - \nabla \cdot (\overline{\rho} D \nabla \widetilde{c}) = \overline{\omega^c} - \overline{\left(\frac{W_i}{W}\right)} \cdot \overline{cS^{\text{rad},i}}$$

$$+ \left(\overline{\left(\frac{W_{ff}}{W}\right)} + \left(1 - \widetilde{i}\right) \overline{\left(\frac{W_i}{W}\right)} \cdot \overline{\left(\frac{V_{ff}}{V}\right)} \right) \overline{\rho} \widetilde{c} \frac{\varepsilon}{k} g \tag{2.101}$$

$$\nabla \cdot \left(\overline{\rho} \widetilde{\boldsymbol{u}} \widetilde{c''^2}\right) - \nabla \cdot \left(D \nabla \widetilde{c''^2}\right)$$

$$= 2\frac{\mu_T}{\sigma_T} (\nabla \widetilde{c})^2 - 2\overline{\rho} \frac{\varepsilon}{k} \widetilde{c''^2} \left(1 - g \left(\overline{\frac{W_{ff}}{W}} - 2 \left(\widetilde{i} - 1\right) \overline{\frac{V_{ff}}{V}} \cdot \overline{\frac{W_i}{W}} \right) \right)$$

$$+ \; 2\overline{c\omega^c} - 2\widetilde{c}\overline{\omega^c} - 2\widetilde{c''^2} \overline{\frac{W_i}{W} S^{rad,i}} \tag{2.102}$$

Mixture fraction, f

$$\overline{\rho} \widetilde{\boldsymbol{u}} \nabla \widetilde{f} = \nabla \left(\overline{\rho} D \nabla \widetilde{f}\right) \tag{2.103}$$

$$\overline{\rho} \widetilde{\boldsymbol{u}} \nabla g = \nabla \left(D \nabla g\right) + 2D \left(\nabla \widetilde{f}\right)^2 - 2Dg \tag{2.104}$$

Enthalpy scalar, i

$$\nabla \cdot \left(\overline{\rho} \widetilde{\boldsymbol{u}} \widetilde{i}\right) - \nabla \cdot \left(\overline{\rho} D \nabla \widetilde{i}\right) = \overline{\rho} \left(\widetilde{i} - 1\right) \overline{\left(\frac{V_{ff}}{V}\right)} \frac{\varepsilon}{k} g - \overline{S^{\text{rad},i}} \tag{2.105}$$

In these expressions, $g = \widetilde{f''^2}$ and $D = D_{im} + \frac{\mu^T}{\text{Sc}_T}$.

Thermochemical relations

The transport equations are completed with the relations of the species mass fractions, density and temperature to the means and variances of these scalars:

$$\overline{\rho} = \overline{\rho} \left(\widetilde{c}, \widetilde{c''^2}, \widetilde{f}, \widetilde{f''^2}, \widetilde{i}\right) \tag{2.106}$$

$$\overline{\boldsymbol{Y}} = \overline{\boldsymbol{Y}} \left(\widetilde{c}, \widetilde{c''^2}, \widetilde{f}, \widetilde{f''^2}, \widetilde{i}\right) \tag{2.107}$$

$$\overline{T} = \overline{T} \left(\widetilde{c}, \widetilde{c''^2}, \widetilde{f}, \widetilde{f''^2}, \widetilde{i}\right) \tag{2.108}$$

2.8   Solving the turbulent CFI-transport equations

The following quantities need to be calculated to be able to solve the Favre-averaged transport equations:

- $\overline{\rho}$, $\overline{S^c}$, $\overline{cS^c}$, $\overline{cS^{rad,i}}$, $\overline{S^{rad,i}}$

- $\overline{\dfrac{W_i}{W}}$, $\overline{\dfrac{W_{ii}}{W}}$, $\overline{\dfrac{W_{ff}}{W}}$

- $\overline{\dfrac{V_{ff}}{V}}$

This can be done by calculating their laminar counterparts for all values of c, f and i and subsequently averaging the result using expressions (2.96)-(2.100) and given values for the means and variances of the CFI-scalars. This results in repetitive calculations of the same quantities which can be prevented by the use of a thermochemical database. To greatly speed up the solution of the Favre-averaged transport equations, the above itemized quantities, plus the species mass fractions, density and temperature, are calculated in advance and stored in a thermochemical database. During a turbulent combustion simulation they are retrieved from the database, significantly reducing the total computational time. Also, this database can be used in any combusting flow simulation where the chemical composition of the inlets is identical. This can significantly reduce computational time for consecutive simulations with the same flow composition but with differences in e.g. inlet turbulence intensities or velocities.

In the creation of a thermochemical database for use in turbulent flow simulations, 3 actions are necessary:

- A routine that creates the *laminar* thermochemical database,

- An averaging routine that creates the *turbulent* thermochemical database,

- An interface routine that obtains the adequate values from the turbulent database file.

These 3 items will be discussed separately in the following sections. To create the laminar thermochemical database, a code has been written which will be presented in the next section. Then the Favre-averaging of that database will be discussed, after which the interface routine of the turbulent database with a flow-solver will be presented.

2.8.1   The laminar database program

The laminar CFI-transport equations can be cast in the following form, for a steady-state flow:

$$
\begin{aligned}
\boldsymbol{L}\left(\boldsymbol{c}\right) &= \boldsymbol{\omega^c} \\
\boldsymbol{L}\left(f\right) &= 0 \\
\boldsymbol{L}\left(i\right) &= \omega^i \\
\boldsymbol{b^r\omega} &= \boldsymbol{0} \\
\boldsymbol{\eta}_c &= f\boldsymbol{\eta}_c^{in1} + \left(1-f\right)\boldsymbol{\eta}_c^{in2}
\end{aligned}
\tag{2.109}
$$

Or, for presumed values of $\boldsymbol{c} = \boldsymbol{c}^0$, $f = f^0$ and $i = i^0$

$$
\begin{aligned}
\boldsymbol{c} &= \boldsymbol{c}^0 \\
f &= f^0 \\
i &= i^0 \\
\boldsymbol{b}^r \boldsymbol{\omega} &= \boldsymbol{0} \\
\boldsymbol{\eta}_c &= f \boldsymbol{\eta}_c^{in1} + (1 - f) \boldsymbol{\eta}_c^{in2}
\end{aligned}
\tag{2.110}
$$

Given the pressure of the problem and the ideal-gas law, this set of expressions is closed and can therefore be solved. It is a square system consisting of $N+1$ unknowns involved in $N+1$ expressions:

$$
\begin{cases}
\eta_k^s = \sum_{j=1}^{N} b_{kj}^s Y_j = c_k \eta_k^{s,eq} + (1 - c_k) \eta_k^{s,u} \quad , k = 1, .., S \\[2ex]
\sum_{k=1}^{N} b_{kj}^r \omega_j \left(\boldsymbol{Y}, T \right) = 0 \quad , k = 1, .., M \\[2ex]
\eta_c^k = \sum_{j=1}^{N} b_{kj}^c Y_j = f \eta^{c,in1} + (1 - f) \eta^{c,in2} \quad , k = 1, .., E \\[2ex]
h \left(\boldsymbol{Y}, T \right) = i h^{max} + (1 - i) h^{min}
\end{cases}
\tag{2.111}
$$

or $\boldsymbol{F} \left(\boldsymbol{Y}, T; \boldsymbol{c}^0, f^0, i^0 \right) = \boldsymbol{0}$. For the solution of this system, various numerical techniques exist, see e.g. ref. [43]. These methods solve the system of equations iteratively given a suitable initial guess. Here, the exact Newton's method will be used, described by, with $\boldsymbol{x} = \left(\boldsymbol{Y}, T \right)^T$:

$$
\begin{aligned}
\boldsymbol{x}^{k+1} &= \boldsymbol{x}^k + \boldsymbol{s}^k \tag{2.112} \\
\boldsymbol{J} \left(\boldsymbol{x}^k \right) \boldsymbol{s}^k &= -\boldsymbol{F} \left(\boldsymbol{x}^k \right) \tag{2.113}
\end{aligned}
$$

This is an iterative process, which stops when the following convergence criteria are reached:

$$
\begin{aligned}
\left\| \boldsymbol{F}^k \right\| &\leq \epsilon_{RF} \left\| \boldsymbol{F}^{k-1} \right\| + \epsilon_{AF} \tag{2.114} \\
\left| x_i^k \right| &\leq \epsilon_{RYT} \left| x_i^{k-1} \right| + \epsilon_{AYT} \quad , \forall i = 1, .., N \tag{2.115}
\end{aligned}
$$

In this expression, ϵ_{RF} and ϵ_{AF} are the relative and absolute convergence tolerances for the norm of $\boldsymbol{F}$ and ϵ_{RYT} and ϵ_{AYT} the absolute and relative tolerances for $\boldsymbol{Y}$ and T, respectively. Alternatively, the iterations stop when these criteria are not met and either the maximum number of iterations is reached or the iterative results diverge.

System (2.111) is solved for a finite number of points $(\boldsymbol{c}^0, f^0, i^0)$ which cover the space defined by $(\boldsymbol{c}, f, i)^T \in [0, 1]$. The grid spacing Δc_k^0, Δf^0, Δi^0 can be defined in multiple ways, which lay between the extremes of aiming to keep the function value spacing constant, i.e. $\Delta \phi (c, f, i) \simeq$ constant, and of taking a constant grid spacing, allowing $\Delta \phi$ to vary over the grid spacing. The former method yields a constant gradient of ϕ over the grid spacing, avoiding large solution changes between grid points, which yields more accurate results when they are interpolated. However, the latter method is much simpler in its implementation and when the constant grid spacing is chosen in such a way that it is an optimum between an adequate density in areas with large gradients of ϕ and a relatively small total number of grid points, it also yields adequate results. The latter method

is adopted here, the scalars are calculated on $N_\phi + 1$ grid points per scalar, with N_ϕ the number of divisions of scalar ϕ. The values are defined by:

$$\phi_k^j \;=\; j \cdot \Delta\phi_k \tag{2.116}$$

$$\Delta\phi_k \;=\; \frac{1}{N_\phi} \tag{2.117}$$

where $j = 0, .., N_i$, yielding grid points between the extremes 0 and 1 of each scalar. The total number of grid points N_ϕ is N_c for the RPV's, N_f for the mixture fraction, and N_i for the enthalpy scalar.

Calculation procedure

In the database program standard CHEMKIN routines are implemented [28]. Properties such as density, temperature etc. are calculated using CHEMKIN routines, also the species and mechanism properties such as source terms are obtained from these routines. Species and mechanism properties are obtained from a CHEMKIN generated file, the *CHEMKIN link file*. To be able to create the laminar database, the following items need to exist:

- A file containing the species thermochemical properties; the CHEMKIN link file

- A file containing the CSP-generated **b**-matrix

How the **b**-matrix can be generated is described in appendix C. Also, a number of settings need to be defined which are used inside the program. These settings are defined in a input file to the process which is read by the program. Amongst others these are:

- Adiabatic or nonadiabatic calculation

- Number of inlets (1 or 2); premixed or nonpremixed problem

- Chemical composition of each inlet:

    - Species mass fractions and temperature
    - Overall pressure of the problem

- RPV composition used; $\boldsymbol{b}^s$

    - Provided by CSP
    - User-provided

- Square system solver parameters

    - Tolerances ϵ_{RF}, ϵ_{AF} , ϵ_{RYT} and ϵ_{AYT}
    - Maximum number of iterations

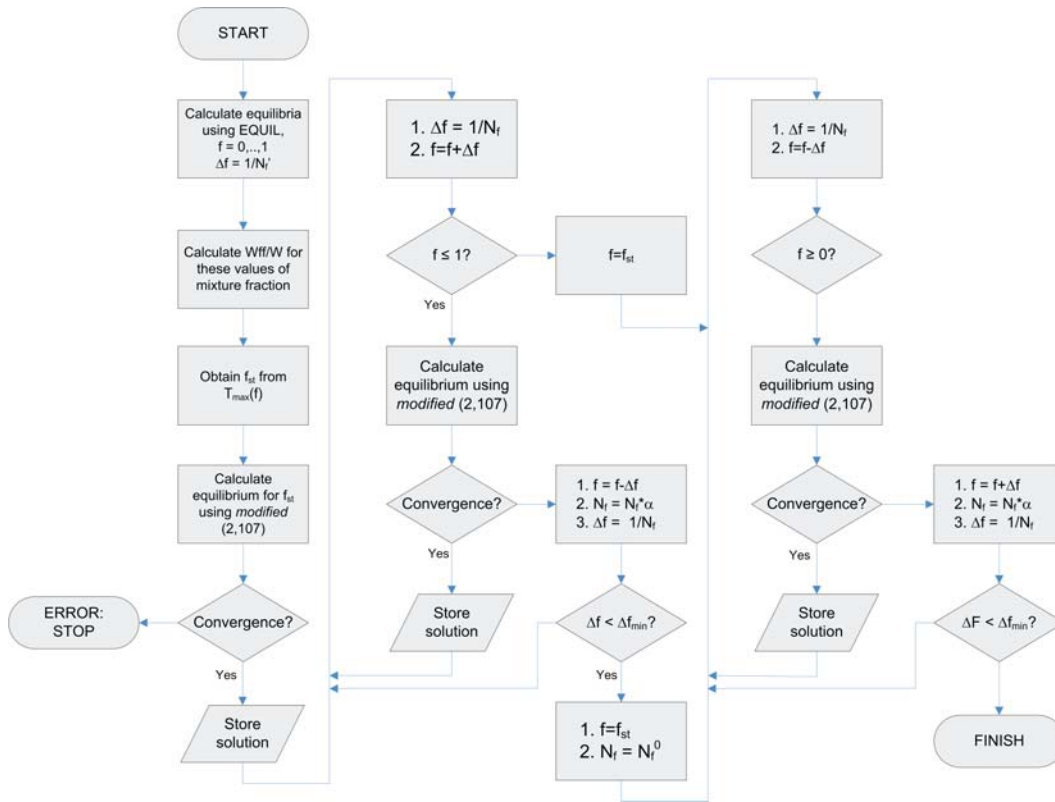- Database density parameters N_c, N_f and N_i

- Stepsize criteria

Figure 2.1: Flow chart of the mixture fraction loop of the laminar database program.

– Stepsize reduction factor α in case of no convergence

– Smallest possible step size in c_k or i, or in f

It can be observed that the user can opt to use the CSP-defined reduced chemistry mapping through η^s or define this himself. The specification of the steady-state species is always provided by CSP. Having these values set, the program can start generating the laminar database. This is done as follows. First the range of mixture fractions is calculated at adiabatic equilibrium, then the enthalpy scalar is looped for all calculated values of f. finally, the RPV scalars are looped for all previously calculated values, creating a grid of values on $(\mathbf{c}, f, i)^T \in [\mathbf{0}, \mathbf{1}]$.

Mixture fraction

The mixture fraction is looped in the sequence depicted in figure 2.1, with $c_k = 1, k = 1, .., S$ and $i = 1$. From this sequence some remarks can be made. The thermodynamic equilibrium is first calculated on a larger number of grid points of mixture fraction (N'_f) than later in the database (N_f). This is done for two main purposes. First it is done to find an accurate value of the stoichiometric mixture fraction, which can be a very small value. For instance, $f_{st} = 0.055$ in atmospheric methane-air combustion. To obtain this value with 2 digits accuracy $N'_f \geq 1000$ which would yield a unacceptably large thermodynamic database if this value was also used for N_f. Second, as will be shown further on in this thesis, the function $\mathbf{W}$ often exhibits a very high gradient around the stoichiometric value. To be

able to yield accurate values of $\boldsymbol{W}_{ff}$ a high grid point density is needed around F_{st} which is provided by N'_f.

After calculating the thermodynamic equilibria, these are recalculated using the chemical reaction mechanism. For this purpose, the RPV equations from expression (2.111) cannot be used. These expressions are:

$$\sum_{j=1}^{N} b_{kj}^s Y_j - c_k \eta_k^{s,eq} + (1 - c_k) \eta_k^{s,u} = 0 \tag{2.118}$$

Since $\boldsymbol{c} = \boldsymbol{1}$ in these expressions, a paradox exists: in order to calculate this expression, $\boldsymbol{Y}^{eq}$ needs to be known, which is supposed to be the solution of this system. Therefore, another approach must be made. The chemical equilibrium is such that all species are in steady-state, and that the source terms of all species are zero, $\omega_i = 0$, $\forall i = 1, .., N$. This means that any linear combination of source terms is also zero, hence:

$$\boldsymbol{b}^s \cdot \boldsymbol{\omega} = \boldsymbol{0} \tag{2.119}$$

is valid too at chemical equilibrium. This expression is used instead expression (2.118) for the kth RPV equation when $c_k = 1$. In essence this expression states that when a RPV c_k has value 1, the RPV is supposed to be in quasi-steady-state and its source term should be 0. The deviation from this solution when $\boldsymbol{c} = \boldsymbol{1}$ with the equilibrium condition calculated using CHEMKIN EQUIL is well within the tolerance criteria defined above.

Calculations are started with f_{st} to ensure this value is always present in the database file. At this value of f the temperature and the chance of a convergent result are highest since the steady-state relations are most valid. It can be argued that when this mixture fraction does not yield a convergent solution of the modified system of expressions (2.111), convergence of this system at any other mixture fraction $f \neq f_{st}$ is highly uncertain. Therefore the iteration process is broken off if a solution is not reached at this mixture fraction and a thermochemical database will not be created. If the calculation is successful, its solution is used as an initial guess for the subsequent iteration. This is done for all iteration steps; the last known good solution is used as an initial guess for the next iteration step.

If a calculation fails, this might originate from a stepsize from the last known good solution which is too high. Therefore, when this occurs, the stepsize is reduced with a factor α and the calculation is attempted again. A minimum stepsize threshold has been inserted to prevent the stepsize approaching zero. It can be observed from the figure that if the minimum stepsize is reached, the iteration procedure is broken off.

Not all solutions are indeed stored. Only those for which $f^0 = j/N_f$ are stored for later use. This is done to prevent that the database size gets out of hand and to prevent numerous solutions of the system being stored with similar values of f, at the edge of the convergence domain. Also, it can be observed that not all values of f ranging from 0 to 1 are calculated. At some mixture fraction, the temperature of the system is so low that the steady-state relations do not apply and the system will only yield unrealistic solutions or yield no solution at all. The minimum or maximum mixture fraction with a valid solution are stored in f_{min} and f_{max}, respectively. Since the temperature is monotonically falling with f increasing away from f_{st} it is assumed that once a certain mixture fraction will not yield a satisfactory solution any mixture fraction even further away from f_{st} will neither. The values f_{min} and f_{max} are interpreted as the flammability limits of the mixture beyond which only mixing occurs.
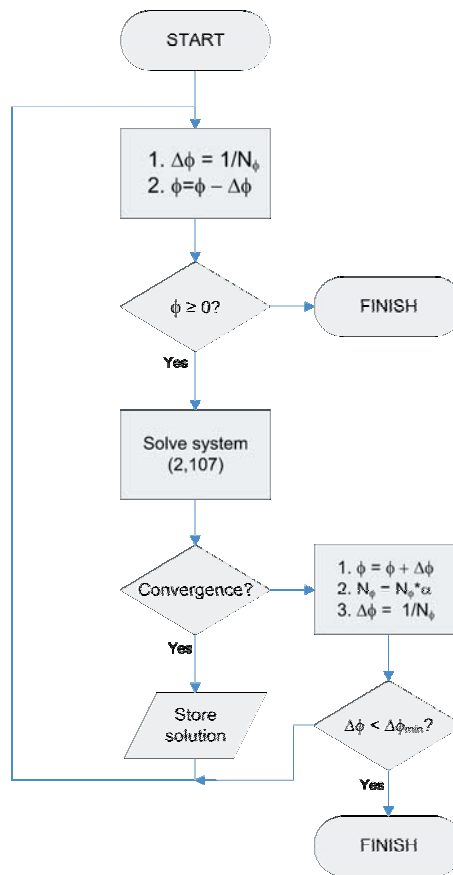
Figure 2.2: Flow chart of the RPV and I loop of the laminar database program.

RPV's and enthalpy scalar

When the equilibria are calculated, for all the converged mixture fractions the enthalpy scalar is looped. Then scalar c_1 is looped for all these grid points, then c_2 etc. until c_S is fully looped and a laminar database with $N_L = (f_{max} - f_{min}) \cdot N_f \cdot N_i \cdot (N_c)^S$ points is created. The main sequence for a scalar $\phi = c_k, i$ is given in figure 2.2. It should be noted that this is the main sequence, the actual sequence is more refined, as is the sequence of f. For instance, when iterations of a reduced stepsize reach a gridpoint j/N_ϕ, the original stepsize $1/N_\phi$ is recovered, accelerating the convergence process in the loop over ϕ.

Also for this sequence, some remarks can also be made. As in the mixture fraction sequence, solutions are only stored on the main grid defined by j/N_ϕ. For the RPV loops, an interpolation routine is executed when the loop exits for whatever reason at $\phi \neq 0$. This routine then fills the database for that loop with values linearly interpolated between the last known good solution and $\phi = 0$, to remain a physically meaningful solution over the entire domain $c_k = [0, 1]$. This is not done for the enthalpy scalar, the value i_{min} at each mixture fraction is stored, beyond these values no RPV loops will be made. Since temperature is monotonically falling with decreasing i, i_{min} is seen as the flammability limit for the given mixture fraction since it will occur when temperatures are low.

2.8.2   Thermochemical properties

Now the mass fraction vector, and temperature are known as functions of c, f and i, the necessary laminar source term quantities can be calculated. These are the source terms ω^c and $S^{rad,i}$ and the derivatives W_i, W_{ii} and V_{ff}. These values are stored along with W_{ff}, the mass fractions, density and temperature in the laminar database file.

2.8.3   The turbulent database program

The turbulent database is created on another grid and includes values of $(\widetilde{c}, \widetilde{c"2}, \widetilde{f}, \widetilde{f"2}, \widetilde{i})$. For each of these values, the laminar database needs to be integrated over the PDF's of each scalar to yield its averaged value. A linear subdivision of the scalar variances is not taken since it is a fact that the β-function differs greatly in shape for small values of the scalar variance. Therefore, a 4th order polynomial dependence of the grid points will be employed here:

$$\widetilde{\phi"2}\left(j\right) = \left(\frac{j}{N_{\widetilde{\phi"2}}}\right)^4 \tag{2.120}$$

where $N_{\widetilde{\phi"2}}$ is the number of grid points (minus 1) for the scalar variance. This ensures that 70% of the grid points for the variance are below $\widetilde{\phi"2} = 0.25$, which is the region where the β-function changes the most. For the means of the scalars, a linear distribution is used:

$$\widetilde{\phi}\left(j\right) = \frac{j}{N_{\widetilde{\phi}}} \tag{2.121}$$

with $N_{\widetilde{\phi}}$ equal to the number of grid points in the means of scalar ϕ, minus 1. At each turbulent database grid point the laminar database is integrated over the PDFs. This is done as follows:

$$
\begin{aligned}
\overline{\phi} &= \int_{c=0}^{1} \int_{f=0}^{1} \int_{i=0}^{1} \phi\left(c, f, i\right) P\left(c_1\right) \cdot ... \cdot P\left(c_S\right) P\left(f\right) P\left(i\right) \mathrm{d}c_1 \cdot ... \cdot \mathrm{d}c_S \mathrm{d}f \mathrm{d}i \\
&\simeq \sum_{k=1}^{N_L} \phi_k\left(c, f, i\right) \int_{c_k^1 = c_k^1 - \Delta c^k}^{c_k^1} P\left(c_1\right) \mathrm{d}c_1 \cdot \\
&\quad .. \quad \cdot \int_{c_k^S = c_k^S - \Delta c^S}^{c_k^S} P\left(c_S\right) \mathrm{d}c_S \int_{f=f^k-\Delta f}^{f^k} P\left(f\right) \mathrm{d}f \int_{i=i^k-\Delta i}^{i^k} P\left(i\right) \mathrm{d}i
\end{aligned} \tag{2.122}
$$

with N_L the number of points in the laminar database. The errors in this Riemann sum are small if the scalar does not vary significantly over the integration interval. It should be noted that the PDFs are still integrated exact, these are the quantities that might vary significantly over the integration interval. This procedure omits the use of a high-accuracy integration procedure, saving valuable computational time and programming efforts at hardly any expense of accuracy, provided the grid point density in the laminar database has been chosen adequately.

It can be seen from the definition of the β-function in expression (2.98) that for $a \geq 0$ to hold, $\widetilde{\phi"2} < \widetilde{\phi}\left(1 - \widetilde{\phi}\right)$. When this is an equality, the β-function takes the shape of a double delta function.

Therefore, the double δ-function is used when the demand $a \geq 0$ is not met:

$$P\left(\phi\right) = \delta(\phi) + \delta\left(1-\phi\right) \quad , \widetilde{\phi''^2} \geq \widetilde{\phi}\left(1-\widetilde{\phi}\right) \tag{2.123}$$

Which is a function which is 1 when $\widetilde{\phi}$ is 0 or 1.

As is observed from the laminar database, the calculated mixture fraction and enthalpy scalars do not cover the full range $[0, 1]$ necessary for the integration. This means that the integration by the Riemann sum of expression (2.122) is not complete. For the remaining parts of the domain, where no database exists, a 'dummy' integration is created over N'_L gridpoints. As described above, these parts of the domain are assumed to be beyond the flammability limits of the mixture and the thermochemical properties will be a function of cold mixing only. The integration for these parts of the domain will be made with the assumption that all source terms are zero, i.e. also functions of W and V and its derivatives are presumed zero, and temperature, density and species mass fractions will only be a function of f. Using this assumption, this part of the domain can be integrated with only the knowledge of the inlet compositions and using a dummy grid for the mixture fraction:

$$\overline{\phi}' \simeq \sum_{k=1}^{N'_L} \phi_k\left(c=1, f, i=1\right) \int_{f=f^k-\Delta f}^{f^k} P\left(f\right) \mathrm{d}f \quad , f_{min} > f > f_{max}, i < i_{min} \tag{2.124}$$

Following the fact that the integral of the PDF alone is identical 1. A dummy grid is used here, consisting of N'_L points with an adequate grid spacing in f to yield an accurate result of the Riemann sum. The value of this integral is then added to the result of expression (2.122), yielding the averaged value of the scalar. For the source terms, functions of W and V and its derivatives this extra integral has no consequence for the result of expression (2.122), only for the species mass fractions, density and temperature. By using this special integral, the memory requirement for the laminar database is dramatically reduced, as is the computational time for the integration, since no array loops are necessary for the regions outside the flammability limits.

The values that are stored in the turbulent database file are, at each grid point $(\widetilde{c}, \widetilde{c''2}, \widetilde{f}, \widetilde{f''2}, \widetilde{i})$:

- Species mass fractions

- Temperature

- Density

- $\overline{\omega^c}$ and $\overline{c\omega^c}$

- $\overline{S^{rad,i}}$ and $\overline{cS^{rad,i}}$

- $\overline{\frac{W_i}{W}}$, $\overline{\frac{W_{ii}}{W}}$, $\overline{\frac{W_{ff}}{W}}$ and $\overline{\frac{V_{ff}}{V}}$

This means that at each grid point $N + 7 \cdot S + 3$ values are stored. The number of grid points is

$$\left(N_{\widetilde{c}} N_{\widetilde{c''2}}\right)^S \cdot N_{\widetilde{f}} N_{\widetilde{f''2}} N_{\widetilde{i}} \tag{2.125}$$

If 16 bits are used to store each scalar and if the scalar grid values are also stored at each point, the total size of the database is then, in Mb:

$$\text{Size} \simeq \frac{16}{1024^2} \left(N_{\widetilde{c}} N_{\widetilde{c''2}} \right)^S \cdot N_{\widetilde{f}} N_{\widetilde{f''2}} N_{\widetilde{i}} \left(N + 9 \cdot S + 6 \right) \quad [Mb] \tag{2.126}$$

For example, if the GRI-Mech 3.0 mechanism [55] is used where $N = 53$, if 1 reaction progress variable is used in the mapping of the remaining chemistry and if $N_\phi = 10$ for all scalars, this yields a database size of approximately $10 Gb$. However, for adiabatic calculations such as will be performed in this thesis, the memory requirement is much less:

$$\text{Size} \simeq \frac{16}{1024^2} \left(N_{\widetilde{c}} N_{\widetilde{c''2}} \right)^S \cdot N_{\widetilde{f}} N_{\widetilde{f''2}} \left(N + 5 \cdot S + 4 \right) \quad [Mb] \tag{2.127}$$

yielding a memory requirement of approximately $10 Mb$ for $N_\phi = 10$.

2.9 Efficient storage, retrieval and interpolation of data

As is described here, the CFI-combustion model allows a variable number of reaction progress variables to be used. The data is stored on a finite grid of scalar values. To be able to use the database in a flow calculation, the data has to be interpolated to yield the necessary function values at the scalar values dictated by the transport equation solver. The grid points necessary for this interpolation can be obtained in several ways. The most arduous is to use a search algorithm that sifts through the database looking for the correct values. But, if on the other hand knowledge exists of how exactly the scalars are stored, this greatly speeds up the lookup routine. In that case, that knowledge can be used to obtain the specific location of the grid point, and it a simple matter to pick that value from the database. Therefore, the turbulent data is stored methodically to allow a fast retrieval.

The interpolation function itself (with all necessary data known), can also be implemented in various ways. An often used method is the method of multilinear interpolation, as is e.g. the case in a previous version of the CFI-model presented by Louis [39]. If the interpolation takes place in N-dimensional space, this method requires 2^N interpolation points. In interpolating turbulent database data, suppose with only 1 RPV and mixture fraction and enthalpy variation, $N = 5$ which yields a 32-point interpolation. Increasing the number of RPVs to e.g. 3 yields a 256-point interpolation. Moreover, the multilinear interpolation algorithm becomes rapidly complex with increasing dimension and more and more difficult to implement. Test calculations showed that using this algorithm with $N = 4$ already takes approximately the same amount of time as direct on-the-fly integration of the laminar database, making the use of the turbulent database almost superfluous, had it not been for the repetitive calculations with (almost) the same turbulent scalar values in case of on-the-fly integration. With N increasing the implementation of the multilinear interpolation algorithm becomes a very arduous task and the result is very time-consuming. Therefore, instead of this algorithm, the piecewise linear interpolation algorithm will be used here (see also ref. [62] for a discussion between the two algorithms). First, the data storage algorithm will be discussed, then the implementation of the piecewise linear interpolation algorithm will be shown, after which the data retrieval algorithm will be explained.

2.9.1 Data storage

A database is to be created of a function $\boldsymbol{F}$ depending on various variables $x_1, .., x_n$. The function is defined as:

$$\boldsymbol{F} : (x_1, .., x_n) \rightarrow \boldsymbol{F}(x_1, .., x_n) \tag{2.128}$$

Here, the function is $\mathbb{R}^n \rightarrow \mathbb{R}^m$. For this function, their values are to be calculated and stored for a unique numerical grid of points $\boldsymbol{x}$. When one wants to create this numerical grid one must first set the following quantities:

- Bounds of each $x_i, i = 1, .., n$, x_i^{min} and x_i^{max}

- Number of 'grid points' per dimension, N_j

- Actual division of each dimension, $\boldsymbol{\chi}_i$

Let $x_i \in [x_i^{min}, x_i^{max}]$ where x_i^{min} is the lower bound and x_i^{max} is the higher bound in x_i. Furthermore, let N_i be the number of grid points in the ith dimension and let $\chi_i(j), j = 1, .., N_i$ be the vector containing the actual grid point values in the ith dimension. The demand on χ is that it is monotonic and rising, without loss of generality. This is utilized later, in the data retrieval. Of course $\chi_i(1) = x_i^{min}$ and $\chi_i(N_i) = x_i^{max}$. Also, the division in the ith dimension is not allowed to be a function of another dimension, $\boldsymbol{\chi}_i \neq \boldsymbol{\chi}_i(x_j)$. This ensures that orthonormal hypercubes can be created, which will be explained later on.

With this division chosen, the database will consist of $K = \prod_{i=1}^{n} N_i$ points on which the function values are calculated and stored. Each point consists of a different combination of $\boldsymbol{\chi}_1, .., \boldsymbol{\chi}_n$. One can think of the database as a polyhedron in n-dimensional space, with each rib in dimension i divided into $N_i - 1$ pieces.

The data storage algorithm has to be such that each grid point $(x_1, .., x_n)$ in the database is unique, and that all K combinations are incorporated. This is done using an algorithm that for the kth grid point in the database, in the ith dimension, yields the value of the pointer to the element $P(k, i)$ in the array $\boldsymbol{\chi}_i$. In essence a loop over the pointers P is created, yielding all K possible combinations of $\chi_i(P), i = 1, .., n$ and $P = 1, N_i$. In this way, for $k = 1$ all the pointers $P(1, i) = 1$ and $k = K$ yields $P(K, i) = N_i$. The storage algorithm is defined as follows:

$$P(k, i) = 1 + \text{INT}\left(\frac{k - 1 - \text{INT}\left(\frac{k-1}{\prod_{j=i}^{n} N_j}\right)\prod_{j=i}^{n} N_j}{\prod_{j=i}^{n} N_{j+1}}\right) \tag{2.129}$$

Here $N_{n+1} \equiv 1$ and INT is the integer function known from programming language which converts values to integers by truncation. Using this algorithm, at each point k the values x_i are known, these are given by:

$$x_i^k = \chi_i\left(P(k, i)\right) \tag{2.130}$$

At each database grid point the unique grid point values can be obtained from this relation. Subsequently, the function values $\boldsymbol{F}$ can be calculated for this set of grid point values $\boldsymbol{x}_k, k = 1, .., K$ and stored along with these. This is done in a loop over all values of k.

The database values are stored in a two-dimensional array $B(k, j)$. The first dimension is used for the point number only. In the second dimension the grid point number and values are stored in

locations 1 and $2..n+1$, respectively. When the function $\boldsymbol{F}$ has, say, m dimensions the values in these dimensions are stored in locations $1, .., m$ and the function values in locations $m + 1, .., n + m$.

In the final database file the following information should be contained:

- The number of dimensions, n

- Dimension of the function $\boldsymbol{F}$, m

- The total number of grid points, K

- The number of grid points in each dimension, N_i

- The bounds of each dimension, x_i^{min} and x_i^{max}

- The actual grid in each dimension, $\chi_i(j), j = 1, .., N_i$

- For each grid point k:

    - The grid point number k, in location $B(k, 1)$
    - its basis $x_1, .., x_n$ in locations $B(k, i + 1), i = 1, .., n$
    - function values $F(1)..F(m)$ at that grid point, at locations $B(k, i + n + 1), i = 1, .., m$

In the present turbulent database, $n = 2S + 3$, $m = N + 6S + 2$. The grid point ordering is $\widetilde{c}, \widetilde{c"2}, \widetilde{f}, \widetilde{f"2}, \widetilde{i}$, therefore the grid point locations are defined as follows:

- $i = 1, .., S : \widetilde{c}_i$

- $i = S + 1, .., 2S : \widetilde{c"2}_i$

- $i = 2S + 1 : \widetilde{f}$

- $i = 2S + 2 : \widetilde{f"2}$

- $i = 2S + 3 : \widetilde{i}$

The function values are stored in locations $i = 2S + 4 + j, j = 1, .., N + 6S + 2$. The higher bound of c_k and i is 1, these values therefore need not to be stored. The lower bound of c_k is 0 and is therefore also not stored, i_{min}, f_{min} and f_{max} may vary and are therefore stored. The number of grid points in each dimension and their grid point values are defined in section 2.8.3.

2.9.2   Piecewise linear interpolation

Linear interpolation in n dimensions can be done in several ways. Depending whether the data grid is known or not, whether it is nicely structured or not, various different methods will be suited to the problem at hand. Here, a linear interpolation method can be applied. For a given interpolation point $\boldsymbol{x}$ in n-dimensional space, a polyhedron of 2^n points can be generated of grid points in the database which are closest to the interpolation point, with in each dimension a grid point just above or equal to the interpolation point in that dimension and one just below or equal to it. This compensates for

the anisotropy and variation in grid point density. A piecewise linear algorithm is used here. In this case, only $n + 1$ of the 2^n edge points of the hypercube are used in the interpolation, contrary to the multilinear interpolation algorithm where all 2^N points are needed.

Before the introduction of the algorithm, some nomenclature etc. will be defined first. Say an interpolation point $\boldsymbol{x}^p = (x_1^p, .., x_j^p, ..x_n^p)$ is given. Then a polyhedron can be created of grid points closest to the interpolation points. In each dimension j, 2 points are needed, a point x_j^L smaller or equal to x_j^p, and a point x_j^H larger or equal to x_j^p. This leads to a polyhedron of 2^n points. If it is assumed that the polyhedron is orthonormalizable (i.e. rib lengths 1 and orthogonal adjacent ribs) the x_j^L, x_j^H are identical for each rib of the polyhedron in that dimension j. Then, the polyhedron becomes a hypercube with rib lengths 1. This is not the case e.g. if x_j^L, x_j^H depend on the other dimensions, they then can have a different value for each hypercube edge point. Using the data storage algorithm of the previous section it is assured that this assumption holds.
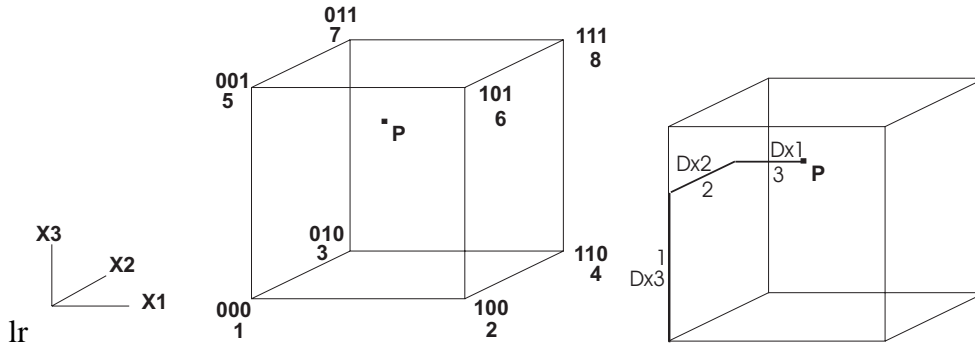
Figure 2.3: Interpolation hypercube for interpolation of point P, 3 dimensions.

In three dimensions the hypercube is depicted on the left in figure 2.3. As can be seen from this figure, the edge points are numbered. A semi-binary interpretation is also denominated to each edge point, originating from the edge point locations. In each dimension a grid point is superscribed '0' if this dimension corresponds to x_j^L and '1' if it corresponds to x_j^H. In three dimensions the point $\boldsymbol{x}_1:(x_1^L, x_2^L, x_3^L)$ is then (000), the point $\boldsymbol{x}_3:(x_1^L, x_2^H, x_3^L) = (010)$ etc. In general, the ith hypercube edge point number is given by the following relation:

$$i = 1 + \sum_{j=1}^{n} b_j 2^{j-1} \tag{2.131}$$

Here, following figure 2.3, b_j is the 0 or 1 in the jth place of the semi-binary representation of the point at hand and $i = 1, .., 2^n$, 8 in this example.

The normalized distances from point 1 to the interpolation point P are given by:

$$\mathrm{D}x_j = \frac{x_j^p - x_j^L}{x_j^H - x_j^L} \tag{2.132}$$

This yields $0 \leq \mathrm{D}x_j \leq 1$. If the hypercube was not orthonormalizable the value of $\mathrm{D}x_j$ would depend on the rib in the x_j^{th} direction this distance is measured on. Then, for example, rib length 1-2 might

not be equal to rib length 7-8, or to length 3-4 or length 5-6. Therefore this restriction is posed on the gridding functions χ. In figure (2.3) on the right these distances are depicted.

The rib lengths can be ordered from large to small, $Dx3 \geq Dx2 \geq Dx1$ for this example, shown in the right sketch of figure 2.3. A vector $\boldsymbol{D}$ is created in which this ordering is stored. Each element D_i contains the dimension with the ith largest Dx_j, in the example $D_1 = 3$, $D_2 = 2$ and $D_3 = 1$.

In piecewise linear interpolation, the dimension in which is interpolated is dictated by the value of Dx_j. The interpolation requires n interconnecting ribs and hence $n + 1$ points. Interpolation is started at the point with x_j^L in all dimensions, the direction in which is traveled is that corresponding to the dimension with the highest value of Dx_j. The interpolation goes from point to point, the ribs that are used are all interconnected. In the example interpolation is started at point $\boldsymbol{x}^1$, (000). The direction with the highest value of Dx_j is Dx_3. The edge points belonging to the rib starting at $\boldsymbol{x}^1$ in the Dx_3-direction are $\boldsymbol{x}^1$ and $\boldsymbol{x}^5$ (001). Dx_2 is next, so the next edge point is acquired by starting at $\boldsymbol{x}^5$ traveling in the x_2-direction, yielding $\boldsymbol{x}^7$ (011). The last point in the example is $\boldsymbol{x}^8$ (111) with direction Dx_1. This is also shown in the right figure (2.3). One can generalize this using the vector $\boldsymbol{D}$. The binary representation of the interpolation point number $j + 1$ is then the one from interpolation point number j with a 1 inserted the position given by D_j, starting at point $\boldsymbol{x}^1$ (or (000)). The vector $\boldsymbol{Q}$ contains these (decimally represented) point numbers and has $n + 1$ dimensions. In the example the subsequent points used are (000):1, (001):5, (011):7 and (111):8, so $\boldsymbol{Q} = (1, 5, 7, 8)$. Suppose one is interested in interpolating the lth function value. The interpolation algorithm now looks as follows:

$$F_l(\boldsymbol{x}^p) = F_l\left(\boldsymbol{x}^{Q(1)}\right) + \sum_{i=1}^{n} \left(F_l\left(\boldsymbol{x}^{Q(i+1)}\right) - F_l\left(\boldsymbol{x}^{Q(i)}\right)\right) Dx(D(i)) \tag{2.133}$$

This interpolation method is suited for use with the turbulent database. What needs to be resolved is what the exact edge points are for a given interpolation point $\boldsymbol{x}^p$ and what the relations are between these edge points to the corresponding point number in the database. For this, information regarding the database structure needs to be known. These topics will be described in the next section.

2.9.3   Data retrieval

Given the interpolation method described by equation 2.133, the function values at the points $\boldsymbol{x}^{Q(i)}$ need to be obtained from the database, as well as the points itself. These can be obtained using a numerical algorithm together with the data storage method described in section 2.9.1.

First, the interpolation point needs to be clipped to within the range of values available in the database: $x_i^p \epsilon [x_i^{min}, x_i^{max}]$. Another approach would be to not interpolate this point if it lies outside the bounds but that approach is not followed here. Then, in each dimension the points x_j^H and x_j^L need to be obtained. This can be done using a search algorithm on the information given in the database of $\boldsymbol{N}$ and χ. There will be a value of j for which $\chi_i(j) \leq x_i^p$ and $\chi_i(j + 1) \geq x_i^p$. These will be stored in the matrix $C(i, j)$ which will for each edge point i of the hypercube in dimension j contains the pointer to χ_i. It should be noted that this is the only search algorithm existing in the present method. The point number k in the turbulent database containing the edge point $\boldsymbol{x}^{Q(i)}$ can then be obtained as follows:

$$k^{Q(i)} = 1 + \sum_{l=1}^{n} (C(m, Q(i)) - 1) \prod_{m=l}^{n} N_m \tag{2.134}$$

The values $x_j^{Q(i)}$ of the edge points involved in the interpolation are now given by:

$$x_j^{Q(i)} = \chi_{Q(i)}(C(Q(i), j)) \tag{2.135}$$

The corresponding function value F_j can be obtained from the turbulent database at locations:

$$F_j\left(\boldsymbol{x}^{Q(i)}\right) = B(k^{Q(i)}, j + n) \tag{2.136}$$

2.9.4 Conclusion

In this section, an algorithm is presented that guides the data storage of the turbulent database. To retrieve this data, another algorithm is presented. Finally, a piecewise multilinear interpolation method is provided to acquire a function value at a given interrogation point $\boldsymbol{x}^P = (\widetilde{c}, \widetilde{c"2}, \widetilde{f}, \widetilde{f"2}, \widetilde{i})^P$. These algorithms allow data storage, retrieval and interpolation in any given (but constant) number of dimensions, with little computational demand. Since data does not need to be searched for but can be retrieved using simple algorithms, a lot of computational time is saved in the interpolation process. Also, a much simpler and less computational demanding algorithm is used than the multilinear interpolation algorithm employed in previous models. It should be noted that these algorithms can be used in any given data storage and retrieval problem, as long as it adheres to the (mild) conditions set in this section.

2.10 Issues

In this section, the CFI combustion model was presented for use in the RaNS transport equations. The necessary source term values are calculated in advance, Favre-averaged and stored in a thermochemical database. For the storage and retrieval of this data algorithms were presented. A multilinear interpolation algorithm was presented to acquire the function values at scalar values dictated by the solution process of the transport equations. In this section, a few remarks are made which are obtained from working with this model and from a numerical assessment of the linear independence of scalars.

2.10.1 Stiffness and the RPV's

Given the CSP-reduced mechanism, described in section 2.5.1, M algebraic steady-state relations of species and the E element conservation relations, N-M-E relations need to be specified, through the matrix $\boldsymbol{b}^s$, to close the system of relations. These relations constitute the remaining chemistry in the system, in the sense that only these relations are able to determine reaction progress out of equilibrium. The constituency of these reaction scalars determines the mapping of reaction progress on the species vector. Two distinct cases can be identified: On the one hand the CSP-defined reaction scalars, which are a linear combination of all species present in the detailed mechanism, and on the other hand the manually defined reaction scalar, which usually consists of only a few species.

As specified in section 2.5.2, the resulting CSP-reduced system is composed of linearly independent relations for the remaining chemistry. These consist of the slowest S modes of the system, reducing the stiffness with respect to the complete set of species transport equations. In contrast, the

steady-state relations constitute the fastest modes of the system, represented by the M species globally most influenced by the M fastest chemical time scales and exhibiting strong participation in the M $\boldsymbol{f}^r \simeq \boldsymbol{0}$ relations.

The $\boldsymbol{b}^s$-matrix is usually fully populated. However, often in literature one finds that the reduced mechanism is *not* mapped onto the slowest modes, but onto a few species, such as CO_2 and H_2O, see e.g. reference [41]. Here it will be assessed what are the consequences of this practice. For this purpose, the following notation is adopted: variables in lower case will denote CSP-defined variables, items in upper case 'manually' defined. A 'manual' $\boldsymbol{B}$ matrix is defined, which consists of the same steady-state and element conservation relations as its CSP-defined counterpart, i.e. $\boldsymbol{B} = [\boldsymbol{b}^r, \boldsymbol{b}^c, \boldsymbol{B}^s]$.

$\boldsymbol{B}^s$ can be expanded using $\boldsymbol{b}$ since that is a orthonormal set of basis vectors:

$$\boldsymbol{B}^s = \boldsymbol{\gamma}\boldsymbol{b} = \gamma_1\boldsymbol{b}^r + \gamma_2\boldsymbol{b}^c + \gamma_3\boldsymbol{b}^s \tag{2.137}$$

Where $\boldsymbol{\gamma}$ can be obtained from:

$$\boldsymbol{\gamma} = \boldsymbol{B}^s\boldsymbol{a} \tag{2.138}$$

Then $\boldsymbol{H}^s$, the vector that describes the remaining chemistry in the 'general' case, can be written as function of the CSP-determined vector $[\boldsymbol{\eta}_r, \boldsymbol{\eta}_c, \boldsymbol{\eta}_s]^T$:

$$\boldsymbol{H}^s = \gamma_1\boldsymbol{\eta}^r + \gamma_2\boldsymbol{\eta}^c + \gamma_3\boldsymbol{\eta}^s \tag{2.139}$$

When $\gamma_3 = 0$ the matrix $[\boldsymbol{b}_r, \boldsymbol{b}_c, \boldsymbol{B}_s]^T$ is defect and therefore does not span an N-dimensional basis. This means that some relations are a linear relation of the others and that the deduced system is poorly defined. Suppose this is not the case, and suppose that there is a combination:

$$[\boldsymbol{b}^r, \boldsymbol{b}^c, \boldsymbol{B}^s]^T \cdot [\boldsymbol{A}_r, \boldsymbol{A}_c, \boldsymbol{A}_s] = \boldsymbol{I} \tag{2.140}$$

Then the following expansion of $\boldsymbol{A}$ can be made using the orthonormal set of basis vectors $\boldsymbol{a}$:

$$\begin{align}
\boldsymbol{A}_r &= \boldsymbol{a}_r\boldsymbol{\kappa}_r + \boldsymbol{a}_c\boldsymbol{\kappa}_c + \boldsymbol{a}_s\boldsymbol{\kappa}_s \tag{2.141}\\
\boldsymbol{A}_c &= \boldsymbol{a}_r\boldsymbol{\lambda}_r + \boldsymbol{a}_c\boldsymbol{\lambda}_c + \boldsymbol{a}_s\boldsymbol{\lambda}_s \tag{2.142}\\
\boldsymbol{A}_s &= \boldsymbol{a}_r\boldsymbol{\mu}_r + \boldsymbol{a}_c\boldsymbol{\mu}_c + \boldsymbol{a}_s\boldsymbol{\mu}_s \tag{2.143}
\end{align}$$

Writing out expression (2.140) part by part leads to:

$$\begin{align}
\boldsymbol{b}^r\boldsymbol{A}_r = \boldsymbol{\kappa}_r &\equiv \boldsymbol{I} \tag{2.144}\\
\boldsymbol{b}^c\boldsymbol{A}_r = \boldsymbol{\kappa}_c &\equiv \boldsymbol{0} \tag{2.145}\\
\boldsymbol{B}^s\boldsymbol{A}_r = \gamma_1\boldsymbol{\kappa}_r + \gamma_2\boldsymbol{\kappa}_c + \gamma_3\boldsymbol{\kappa}_s = \gamma_1 + \gamma_3\boldsymbol{\kappa}_s &\equiv \boldsymbol{0} \tag{2.146}
\end{align}$$

$$\begin{align}
\boldsymbol{b}^r\boldsymbol{A}_c = \boldsymbol{\lambda}_r &\equiv \boldsymbol{0} \tag{2.147}\\
\boldsymbol{b}^c\boldsymbol{A}_c = \boldsymbol{\lambda}_c &\equiv \boldsymbol{I} \tag{2.148}\\
\boldsymbol{B}^s\boldsymbol{A}_c = \gamma_1\boldsymbol{\lambda}_r + \gamma_2\boldsymbol{\lambda}_c + \gamma_3\boldsymbol{\lambda}_s = \gamma_2 + \gamma_3\boldsymbol{\lambda}_s &\equiv \boldsymbol{0} \tag{2.149}
\end{align}$$

$$\begin{align}
\boldsymbol{b}^r\boldsymbol{A}_s = \boldsymbol{\mu}_r &\equiv \boldsymbol{0} \tag{2.150}\\
\boldsymbol{b}^c\boldsymbol{A}_s = \boldsymbol{\mu}_c &\equiv \boldsymbol{0} \tag{2.151}\\
\boldsymbol{B}^s\boldsymbol{A}_s = \gamma_1\boldsymbol{\mu}_r + \gamma_2\boldsymbol{\mu}_c + \gamma_3\boldsymbol{\mu}_s = \gamma_3\boldsymbol{\mu}_s &\equiv \boldsymbol{I} \tag{2.152}
\end{align}$$

Which leads to the following expression for $\boldsymbol{A}$ which forms $\boldsymbol{AB} = \boldsymbol{I}$:

$$[\boldsymbol{A}_r, \boldsymbol{A}_c, \boldsymbol{A}_s] = \left[\boldsymbol{a}_r + \boldsymbol{a}_s\left(-\boldsymbol{\gamma}_3^{-1}\boldsymbol{\gamma}_1\right), \boldsymbol{a}_c + \boldsymbol{a}_s\left(-\boldsymbol{\gamma}_3^{-1}\boldsymbol{\gamma}_2\right), \boldsymbol{a}_s\left(\boldsymbol{\gamma}_3^{-1}\right)\right] \tag{2.153}$$

Now, presume there is a mass fraction vector $\boldsymbol{Y}$. For this $\boldsymbol{Y}$ can be written:

$$\begin{align}
\boldsymbol{Y} &= \boldsymbol{a}_r\boldsymbol{\eta}^r + \boldsymbol{a}_c\boldsymbol{\eta}^c + \boldsymbol{a}_s\boldsymbol{\eta}^s \tag{2.154}\\
&= \boldsymbol{A}_r\boldsymbol{\eta}^r + \boldsymbol{A}_c\boldsymbol{\eta}^c + \boldsymbol{A}_s\boldsymbol{H}^s \tag{2.155}\\
&= \left[\boldsymbol{a}_r + \boldsymbol{a}_s\left(-\boldsymbol{\gamma}_3^{-1}\boldsymbol{\gamma}_1\right)\right]\boldsymbol{\eta}^r + \left[\boldsymbol{a}_c + \boldsymbol{a}_s\left(-\boldsymbol{\gamma}_3^{-1}\boldsymbol{\gamma}_2\right)\right]\boldsymbol{\eta}^c + \left[\boldsymbol{a}_s\left(\boldsymbol{\gamma}_3^{-1}\right)\right]\boldsymbol{H}^s
\end{align}$$

From these expressions it can be concluded that in a manually defined system

1. slow modes enter the steady-state relations and

2. fast modes enter the remaining chemistry equations H^s.

The latter will lead to a stiffer set of governing equations. This can be shown from the original expression:

$$\begin{align}
\frac{\partial \boldsymbol{Y}}{\partial t} &= \boldsymbol{a}_r\boldsymbol{f}^r + \boldsymbol{a}_c\boldsymbol{f}^c + \boldsymbol{a}_s\boldsymbol{f}^s \\
&= \boldsymbol{A}_r\boldsymbol{f}^r + \boldsymbol{A}_c\boldsymbol{f}^c + \boldsymbol{A}_s\boldsymbol{F}^s
\end{align}$$

$$\tag{2.156}$$

where $\boldsymbol{f} = \boldsymbol{b} \cdot \boldsymbol{g}$. This can be simplified assuming that $\boldsymbol{b}^r \cdot \boldsymbol{g} = \boldsymbol{f}^r \simeq 0$ and since $\boldsymbol{b}^c \cdot \boldsymbol{g} = \boldsymbol{f}^c = \boldsymbol{0}$:

$$\frac{\partial \boldsymbol{Y}}{\partial t} \simeq \boldsymbol{A}_s\boldsymbol{F}^s = \boldsymbol{a}_s\boldsymbol{\gamma}_3^{-1}\left(\boldsymbol{\gamma}_1\boldsymbol{f}^r + \boldsymbol{\gamma}_2\boldsymbol{f}^c\right) + \boldsymbol{a}_s\boldsymbol{f}^s \tag{2.157}$$

Here it can be seen that only if $\boldsymbol{\gamma}_3 \neq \boldsymbol{0}$ and $\boldsymbol{\gamma}_1 = \boldsymbol{\gamma}_2 = \boldsymbol{0}$ fast modes do not enter the presumably slow remaining system. These fast modes can be ignored with respect to the results, but not with respect to the dynamics of the solution. For this reason, the $\boldsymbol{\eta}^s$ vectors are defined with CSP in the CFI-mode, rather than manually.

2.10.2 CFI-scalar behavior

It is assumed in the derivation of the CFI combustion model that the scalars c_k, f and i bounded between 0 and 1, and that the vectors $\boldsymbol{\eta}$ are monotonic between their bounds. For the mixture fraction this is definitely the case. However, for the enthalpy and RPVs this assumption might not always hold.

For the enthalpy scalar the minimum enthalpy is an arbitrary one. Therefore the enthalpy scalar should not be allowed to reach values below 0, if this happens it can be attributed to errors made by the user in setting this value. However, in theory the enthalpy at some location can be larger than its adiabatic value. This happens if heat loss in one part of the domain through radiation is absorbed in another region of the domain that happened to be still without any net heat loss. In that case the enthalpy will be super-adiabatic at the latter location. Therefore, if heat loss through radiation is modeled and heat absorbtion is also taken into account, it should be assessed whether super-adiabatic

values are possible and whether measures should be taken by raising the maximum possible enthalpy of the system h^{max} accordingly.

The composed species relations $\boldsymbol{\eta}^s$ on which the RPV scalars are defined are generally a function of the complete mass fraction vector. When η_k^s is composed of only intermediate species, $\eta_k^{s,eq} = \eta_k^{s,u} = 0$ and the resulting RPV c_k is ill-defined. For the same presence of intermediates in c_k, the behavior of the c_k in the flame zone might not be monotonous. Since the basis vectors $\boldsymbol{b}_j$ are linearly independent, linear operations on them are allowed without changing the behavior of the resulting system. These are often employed in the reduced system to improve its behavior and representation. It is observed that when care is taken in the definition of η_k^s, these issues are not present.

2.10.3 Laminar database program

As is noted by other researchers working with reduced chemical systems [41], the expressions (2.111) defining the reduced set sometimes yields unphysical solutions. These are typically originating at a range $c_k \in [0, c_k^0]$, i.e. in the lower temperature range. In this region, the steady-state relations are progressively less valid with decreasing temperature and the low-dimensional manifold becomes ill-defined. To overcome this problem and still retain a progress variable which is physically meaningful over the entire range $c_k \in [0, 1]$, the thermochemical data is linearly interpolated between the last valid grid point with $c_k > c_k^0$ and the cold flow with $c_k = 0$, when this occurs. An extra scalar ζ is created which is 0 when the solution of a grid point is calculated, and 1 when it is interpolated. This scalar is subsequently Favre-averaged along with the other thermochemical data and also stored in the turbulent database. Subsequently, this scalar field in the solution of the turbulent combusting flow shows the local weight of the interpolated points in the averaged result. This scalar can be assessed as an indication of the local quality of the solution. It will be shown later on in this thesis that high values of this scalar ζ are only seen in the cold regions of the flow. The scalar ζ is also set to 1 when interpolation is started due to lack of convergence, as described in section 2.8.1.

From the sequences described in section 2.8.1 it is seen that the laminar database is created in one-dimensional loops, i.e. one scalar is looped at a time. This is done for 2 purposes. First, it is the most simple way to loop through all grid points of the computational domain. Second, the sequence is chosen in such a way that it is ordered in decreasing probability of convergence. By deviating from $f = f_{st}$, $i = 1$ and $c_k = 1, k = 1, .., S$, the temperature lowers and the set of equations becomes harder to solve. This is partly because the steady-state relations become less valid and also since the actual manifold becomes more dimensional as one progresses off equilibrium. Therefore, if the chosen sequence fails at some point, it can be argued that solutions will hardly be found beyond it and further calculations are meaningless and not necessary. However, it can also be argued that the initial guess should be defined more accurately in these situations. Therefore it might be useful to use loops which more naturally proceed off-equilibrium, for instance by first attempting the path $c_1 = c_2.. = c_S = $ constant and then deviate from that. Also, the initial guess can be defined in a multi-dimensional way, ensuring it to lie closer to the attempted solution. For reasons of simplicity of programming and lack of time this was not attempted here, but should be a recommendation to those wishing to improve the database creation sequence.

2.10.4 Calculation of Thermal NO

It is a well-known fact that the production of thermal nitric oxides NO in a flame is a slow process. It is observed in the globally reduced mechanisms presented in ref. [44] that NO is treated as a major species there. It is active in the reported reduced mechanisms with 6 steps or more. However, in the reduced mechanisms employed for turbulent combustion, the number of RPVs is lower, 3 or 4 at most. In these cases NO is treated as a steady-state species. It will be shown further on that this will lead to an overestimation of the NO mass fractions in a flame. For that reason, instead of the steady-state NO, a separate transport equation will be set up to calculate the thermal NO emission through the simplified Zeldovich mechanism, as also reported by Louis [39]. It is assumed that this mechanism is responsible for the majority of NO production in the turbulent flames reported here. The NO produced by the Zeldovich mechanism is assumed not to be influenced by turbulence, yielding to the following transport equation [39]:

$$\nabla \cdot \left(\overline{\rho} \widetilde{\boldsymbol{u}} \widetilde{Y}_{NO} \right) - \nabla \cdot \left(\overline{\rho} D \nabla \widetilde{Y}_{NO} \right) = \overline{S}^{NO} \tag{2.158}$$

where $\overline{S}^{NO}$ is the averaged value of the source term:

$$S^{NO} = 2 M_{NO} \rho^2 k_f \frac{Y_O Y_{N2}}{M_O M_{N2}} \tag{2.159}$$

with $k_f = 1.8 \cdot 10^{11} exp\left(-38369/T\right)$. This value, which is a function of $(\boldsymbol{c}, f, i)$ through the dependence of the O and N_2 mass fractions, is also averaged in the turbulent database program and stored in the thermochemical database. An extra transport equation is solved for the Zeldovich NO, the source term values are obtained from the turbulent database, as described in section 2.9.

Chapter 3

Laminar database assessment

In this chapter, the performance and behavior of laminar CFI-databases will be compared to runs performed with a detailed chemical reaction mechanism and the PREMIX laminar flame code [28]. Comparisons will be made of 1- and 2-step reduced mechanisms, and of CSP- and manually defined 1-step reduced mechanisms. Their performance will be assessed using 2 different atmospheric cases, a stoichiometric flame and a lean flame. Both flames are perfectly premixed and freely propagating methane-air flames. Therefore, only premixed, adiabatic databases ($f \equiv i \equiv 1$) will be discussed. Part of this research is published in references [11] and [12].

3.1 Cases

In the PREMIX code allows the solution of, amongst others, laminar, 1-dimensional freely propagating, perfectly premixed flames using detailed chemical mechanisms. In this case, the GRI-3.0 mechanism is used, which describes the oxidation of methane or natural gas, and contains $N = 53$ species, consisting of $E = 5$ elements, involved in $R = 325$ reactions [55]. The species list is given in table D.1. The mechanism contains a detailed NO-path, a C^1 and a C^2-path and a simple C^3-path. It allows the solution of very lean to very rich methane-air flames. The parameters of the 2 cases that will be discussed here are described in table 3.1, where ϕ_F means the fuel equivalence ratio. The flames are calculated using the mixture-averaged transport properties, without thermal and pressure diffusion effects. Mass is conserved using the correction velocity formalism, see ref. [28] for details. The solution domain has a length of 10 cm, with the flame igniting at approximately 4 cm into the domain, to prevent radical diffusion towards the inlet. The accuracy parameters were 10^{-12} for the relative tolerance, 10^{-6} for the absolute tolerance, and the solution curvature parameters were adjusted to acquire a solution on approximately 300 grid points, which is the preset maximum number for PREMIX.

case	Description	Y_{CH_4}	Y_{O_2}	$p\ [Bar^a]$	$T^{in}\ [K]$	$T^{ad}\ [K]$	ϕ_F
1	Base case	0.0576	0.2195	1.0	400	2282	1.0
2	Lean case	0.0344	0.2249	1.0	400	1759	0.6

Table 3.1: Parameters of the PREMIX runs

3.2   Reduced mechanisms

The global CSP algorithm is used with the result of case 1, to generate a 1- and a 2-step reduced mechanism. With these reduced mechanisms, both the CSP-defined reduced mechanism vector $\widehat{\boldsymbol{b}}^s$ as well as a user-defined one, $\widehat{\boldsymbol{B}}^s$ are used, the selected steady-state species by CSP will be used in both reduced mechanisms, as well as the element conservation relations. The vector $\widehat{\boldsymbol{B}}^s_1$ for the 1-step mechanism contains all zeros except at the location of CO2, which contains a 1, the 2-step mechanism has an additional vector $\widehat{\boldsymbol{B}}^s_2$ which is only 1 at the location of H_2O. Therefore the user-defined reduced chemistry is mapped entirely onto the species CO2, and H_2O in case of the 2-step mechanism. The steady-state species for all reduced mechanisms are taken from the CSP-reduced mechanism. The steady-state species list is given in table D.3 in Appendix D. The species between brackets in these tables is the one that is in steady-state in the one-step mechanism, and becomes a major species in the 2-step mechanism. Summarizing, the 4 cases are:

- 1-step:

    - CSP-defined mechanism mapping: Database A
    - user-defined mechanism mapping: CO_2: Database B

- 2-steps:

    - CSP-defined mechanism mapping: Database C
    - user-defined mechanism mapping: CO_2 and H_2O: Database D

The list of $E+S$ major species is given in table D.2 of Appendix D, where H2 is a major species in the 2-step mechanism only. In the CSP-reduced remaining chemistry description the reduced mechanism acts in CSP-reactions, as described in section 2.5.2. These are:

$$2CO + O_2 \rightleftharpoons 2CO_2 \tag{3.1}$$
$$2H_2 + O_2 \rightleftharpoons 2H_2O \tag{3.2}$$

where reaction (3.2) becomes active in the 2-step mechanism. These reactions are well-known, they describe the conversion of synthesis gas. It can be shown (see ref. [44]) that by increasing the number of steps to 3, methane becomes a major species, and the third reaction step is the conversion of methane to synthesis gas. It can therefore be concluded that the CSP-reactions agree with what one expects to be the overall reaction steps in reduced mechanisms. For an extension to a higher number of steps in the globally reduced mechanism, see ref. [44]. For the manually reduced mechanism, this assessment into CSP-reactions cannot be made, since the formalism that is used in the CSP-derivation is no longer present.

The CSP-generated composed species vectors $\boldsymbol{\eta}^s$ corresponding to the CSP-reactions (3.1) and (3.2) are given in Appendix D, in tables D.4 and D.5 for the 1- and 2-step reduced mechanisms, respectively. The mapping for the first CSP reaction is different since the major- and steady-state species vectors are different, however it can be shown that η^s_1 in the 1-step mechanism is a linear combination of η^s_1 and η^s_2 of the 2-step reduced mechanism. It is immediately obvious from these tables that this result could not have been obtained manually, for mechanisms of this size automated algorithms are a necessity.

3.3   Database properties

As described in section 2.8.1, the database contains the species mass fractions, density, temperature and source terms as function of c, in case of a premixed adiabatic flame as discussed here. In figures 3.1 and 3.2, the database shapes are shown for temperature, for databases A1 and C1 (Databases A and C for case 1). Several remarks can be made here. First, it is noted that both graphs show an almost linear dependence of temperature on c_k. This is true for all the databases created using a CSP-defined b^s and is most likely due to the particular CSP identifications of c_k.
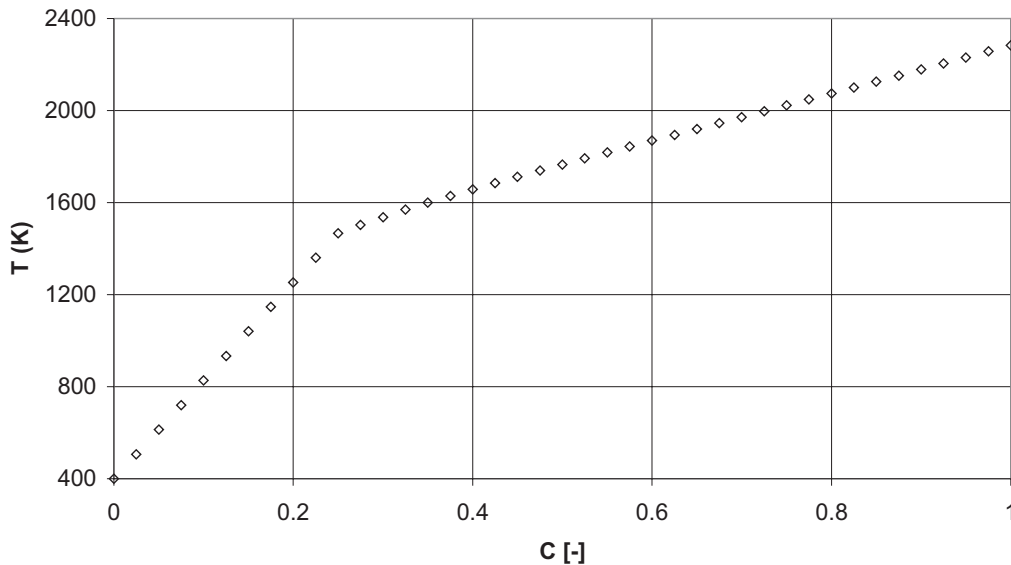
Figure 3.1: Temperature as function of c, database A1.

Second, the temperature dependence of database A1 shows a discontinuity at $c = 0.25$. This is because the system yields unphysical results for values $c < 0.25$, due to the mass fraction of CO2 becoming negative. For this reason, as explained in section 2.10.3, the database is interpolated between the last known good solution and the inlet condition. This shows up as a discontinuity in the graph.

Third, the temperature at $c_1 = c_2 = 0$ is not equal to T^0 which is $400K$, for database C1. It is approximately 1200K, as would the temperature of the 1-step mechanism be at $c = 0$, had there not been interpolated. This shows that at lower values of c_k, where the temperatures are low, the assumptions that were made in the reduction become less valid. In these regions, modifications should be made to correct this behavior. This can be regarded as ignition delay modeling, previous versions of the CFI-model were tested with such a model [58]. However, here a more simple but also effective approach is used. At a certain temperature T^{low}, corresponding to a value $c = c^0$, the database calculations are broken off, and subsequent results are obtained by interpolation between the solution at $c = c^0$ and the cold condition. This 'ignition-delay model' might not be accurate to predict ignition in freely propagating flames, however it will be sufficient in the solution of flames where ignition of
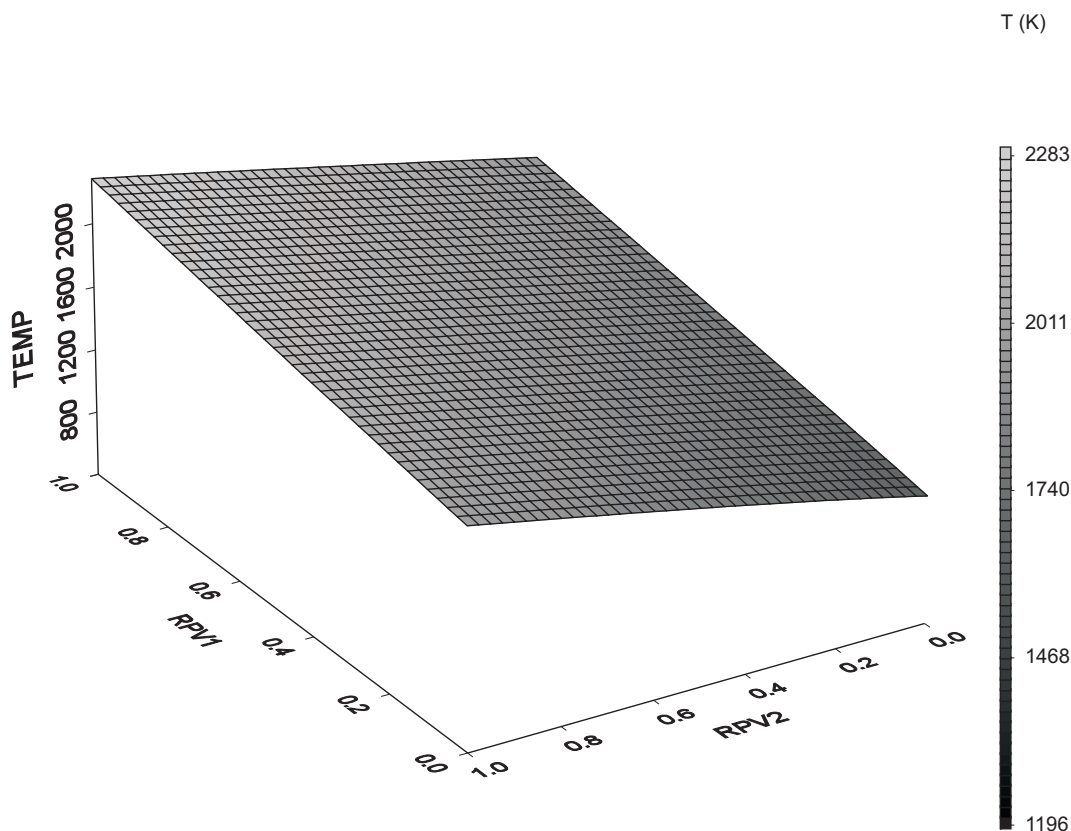
Figure 3.2: Temperature as function of c, database C1.

the fresh mixture is obtained by recirculating hot products. It should be remarked that when this is not present a more refined ignition-delay model might be needed in premixed flows to obtain accurate results. However, the vast majority of industrial continuous-flow burners are stabilized through the recirculation of hot gases and this model is presumed to be efficient. A second reason for using this low-temperature interpolation is to ensure that at the inlets the temperature and density of the mixture is that of the cold condition. Since these quantities are related to c and transport equations are solved only for the reaction scalars, the density and temperature at the inlet are those provided by the database at $c = 0$. Therefore at least at that point the thermochemical data should be concurrent with the data set at the inlet. Usually this means that this point is not obtained from database calculations, but from direct interpolation of the inlet conditions set by the user. To enhance convergence, this region of interpolation is preset to a small region around $c = 0$, typically $c_k < 0.1, \forall k = 1, .., S$. However, in this section, where the database is assessed, this type of interpolation is not used.

In figures 3.3, 3.4 and 3.5, the source terms of databases A1 and C1 are shown, respectively. It can be seen that they are smooth functions of c, an obviously desirable outcome. The interpolation due to the unphysical results for $c < 0.25$ in database A1, as mentioned above, results in the discontinuity in its source term. The source terms are zero at the equilibrium point ($c_k = 1$, $\forall k = 1, .., S$). In database C1, the source terms attain positive as well as negative values while database A1 has a strictly positive source term. This means that the CSP-reaction of the 1-step mechanism will always produce c_1, whereas in the 2-step mechanism the negative source term allows the possibility of c_j
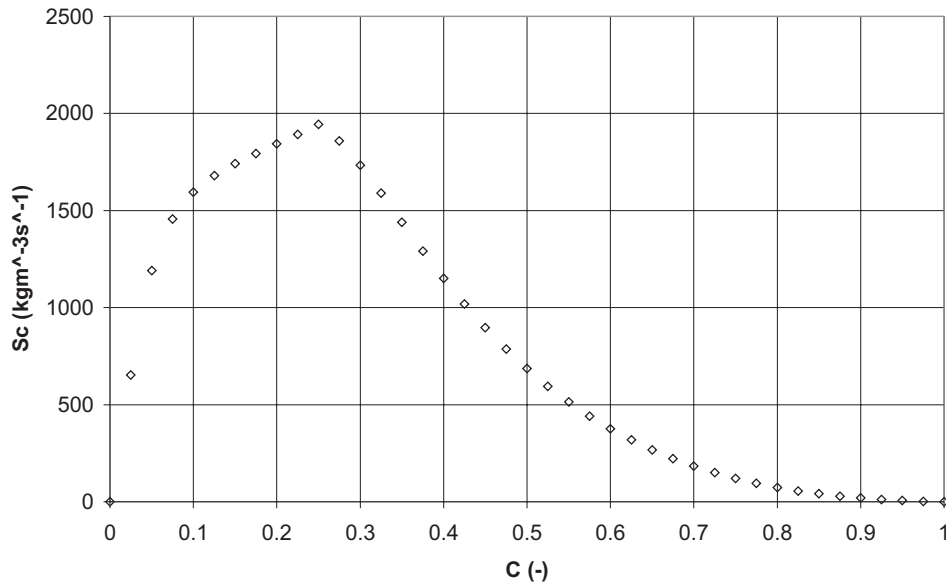
Figure 3.3: Chemical source term of database A1.

moving away from equilibrium for certain values of c_i, $j \neq i$. This is true for ω_1^c for low values of c_2 and high values of c_1, and for ω_2^c in case c_2 is high and c_1 is low. This means that, for conditions near equilibrium, when one of the reaction progress variables is further away from equilibrium than the other, they tend to draw the other RPV away from equilibrium. The result of this fact is that the reaction path will be drawn towards the path $c_1 \sim c_2$. Due to the separation in time scales that exists, the low-dimensional manifold will be built up by roughly equally fast modes. This results in both CSP-reactions being roughly equally fast which will drive the system into this path, as illustrated here.

3.4 Database assessment

In this section, a comparison will be made for the databases using the PREMIX detailed chemistry solution of case 1, the stoichiometric case. Comparisons will be made for the O and OH radicals, since they are important in the production of thermal NO. To be able to make a comparison, at each location x of the detailed solution, the values of $c_k(x)$ are obtained, using definition 2.81 on page 25. Using this relation of c_k to the grid point location x, the database results for these values of c_k can be plotted for this location too. Also, the PREMIX data can be plotted as function of the thus obtained c_k, to be compared to database data in this way. Obviously, the best way to assess the performance of the reduced mechanism databases, is to use them in another laminar flame calculation, this time for the reduced mechanism, and compare the outcomes with the result obtained with the detailed mechanism. A similar approach is taken in ref. [44], however in this paper transport equations were solved for $S + E$ transport equations, ensuring only mass conservation but not element conservation. It proved to be beyond the scope of this work to create such a laminar flame solver for the reduced mechanism involving the element conservation relations, to be able to directly use the CFI-database (which is

S (kg/(m3 s))
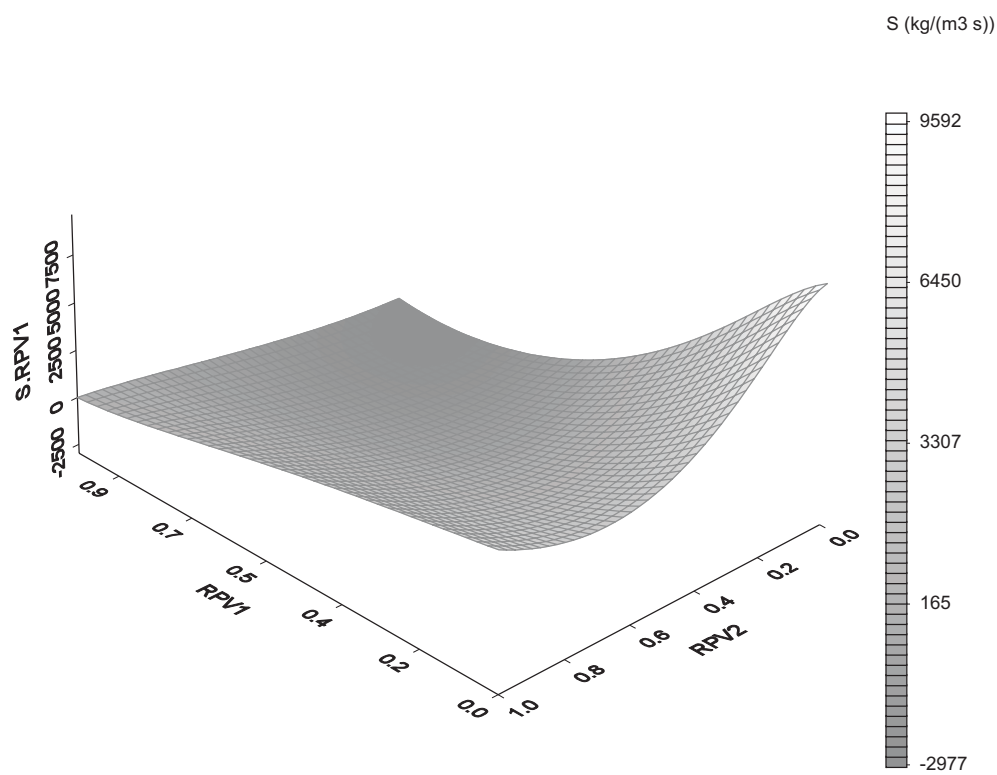
Figure 3.4: Chemical source term of c_1 of database C1.

S (kg/(m3 s))
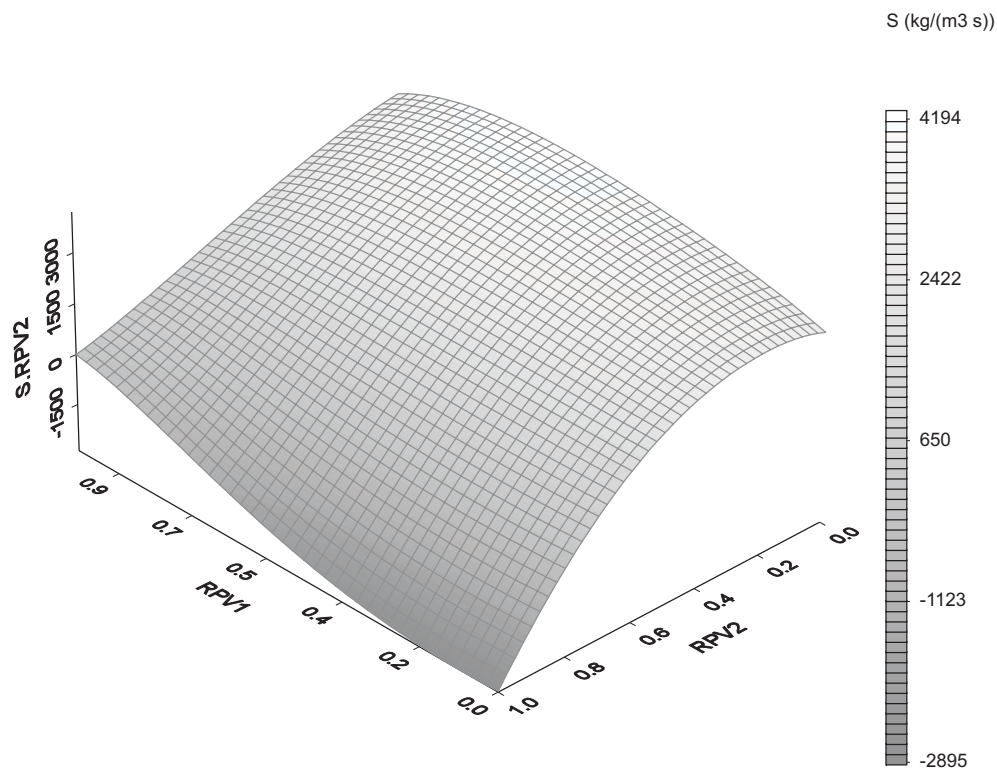
Figure 3.5: Chemical source term of c_2 of database C1.

built up around these relations).

In figures 3.6 and 3.7, the temperature profiles of databases A1 and B1 are compared to those obtained with the detailed mechanism, denoted with "PREMIX," on a RPV basis. The solid lines represent the detailed solution, mapped using the chosen b^s- or B^s-matrix. It can directly be observed that the CSP-mapped reduced mechanism description b^s results in a much smoother mapping than the manually defined B^s, both in the databases as well as in the detailed solution. Database B1 starts deviating at around $c = 0.8$, database A1 follows the detailed solution quite accurately throughout the domain, albeit helped by the interpolation used for $c < 0.25$. It must be remarked that interpolation at the manually mapped c for $c < 0.25$ would have improved this result too.
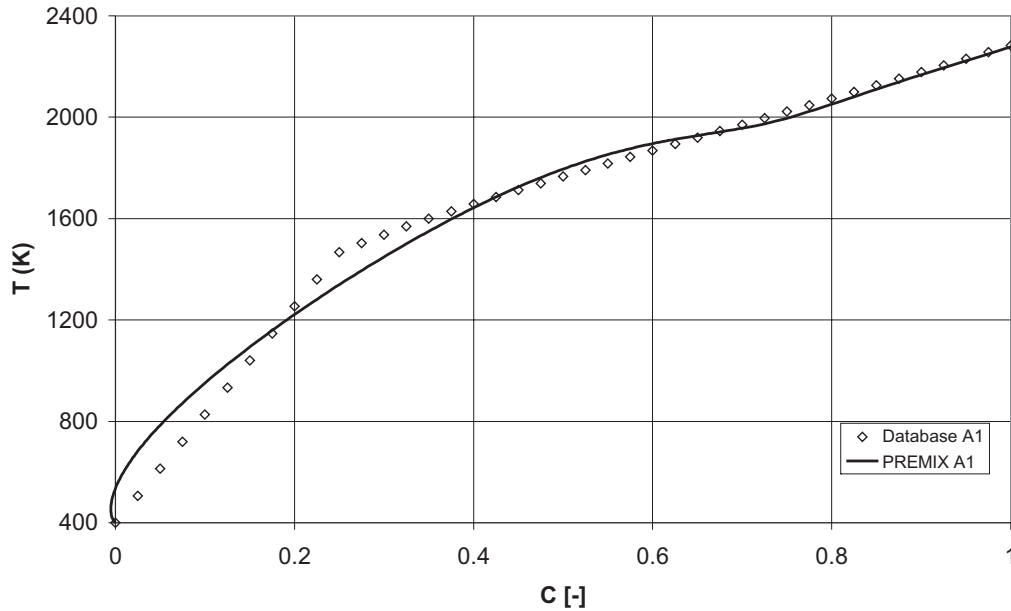
Figure 3.6: Temperature comparison of database A1, on a RPV basis, with the detailed PREMIX solution of case 1.

In figure 3.8 the source terms of databases A1 and B1 are compared with the detailed flow solution, on a RPV basis. It can be seen here that both graphs follow the detailed solution for values of c down to $c \simeq 0.7$. Database A1 yields a source term peak value of the same order of magnitude as the PREMIX solution, database B1 overestimates it by a factor of 2.2. The source term of database A1 is also more similar to the detailed solution source term, and will probably yield more accurate solutions if it were used in a turbulent flame simulatin. Even if B1 would be interpolated for $c < 0.25$, this would still yield an overestimation of the source term of a factor of 1.9 compared to the detailed solution.

In figures 3.9 and 3.10, the O- and OH-radical mass fractions of databases A1 and B1 are compared to the detailed flame solution, on a RPV-basis. It can be seen that the database solution is able to follow the PREMIX solution to roughly $c \simeq 0.7$, for A1 and to 0.8 for B1. The maximum mass fraction predicted by the databases is at lower values for the RPV than those obtained by the detailed solution. Also, the peak values of the OH radical are better predicted than those of the O radical. The CSP-mapped database A1 yields a slightly better overall comparison than the manually mapped B1, deviating from the detailed flow solution at lower values of c.
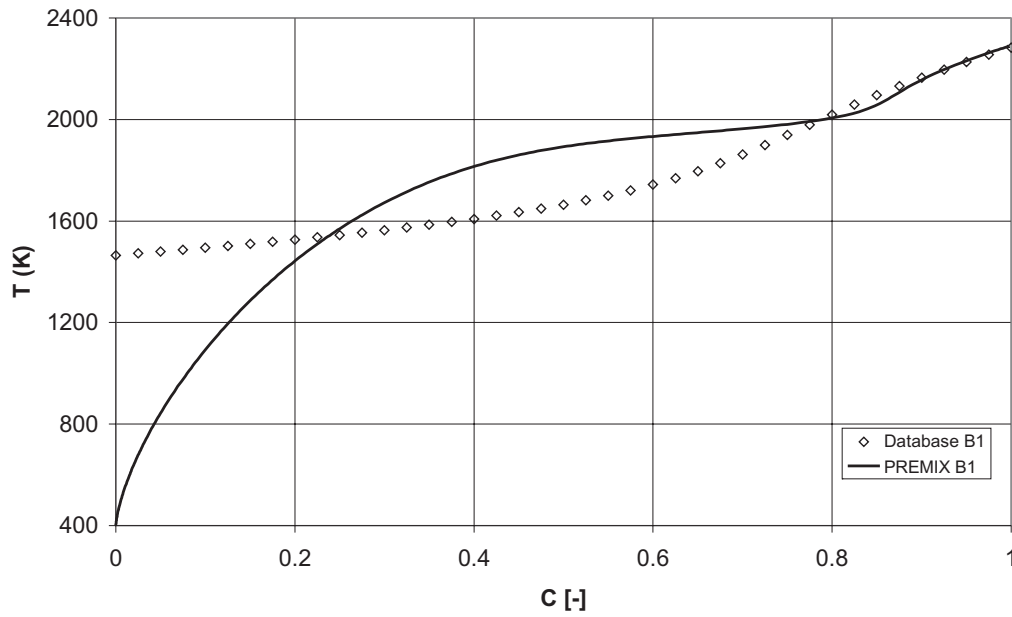
Figure 3.7: Temperature comparison of database B1, on a RPV basis, with the detailed PREMIX solution of case 1.
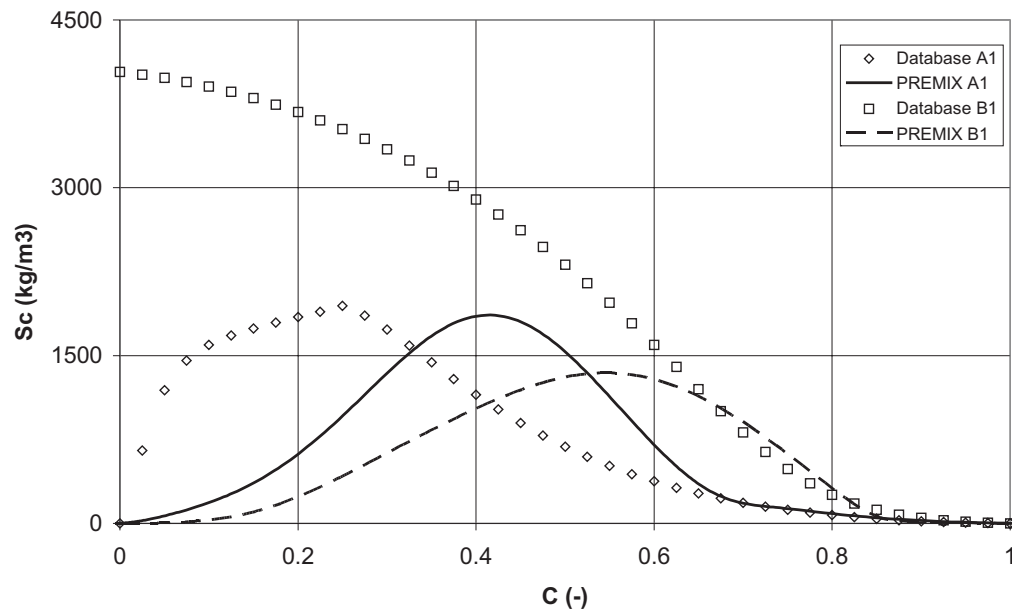
Figure 3.8: Comparison of source term values of databases A1 and B1 with the detailed PREMIX solution, on a RPV basis.

It can be seen from figure 3.9 that the peak mass fraction of the O radical is overpredicted by a factor of almost 2.5, by both 1-step databases. Also the database peak mass fractions are present at lower values of the RPV than those of the detailed solution. How this will affect the results of the
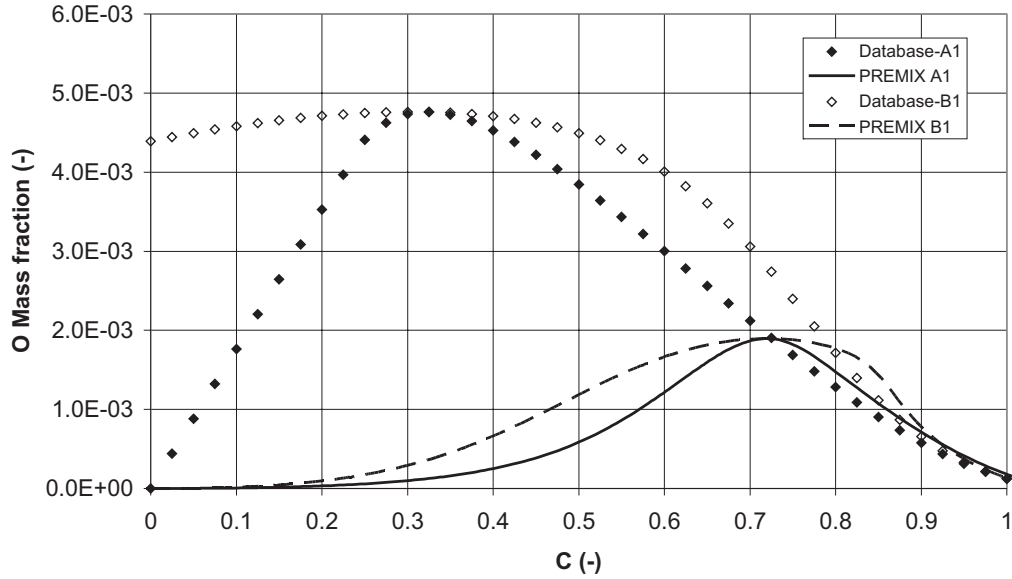
Figure 3.9: Comparison of O mass fractions of databases A1 and B1, on a RPV basis, with detailed PREMIX solution of case 1.
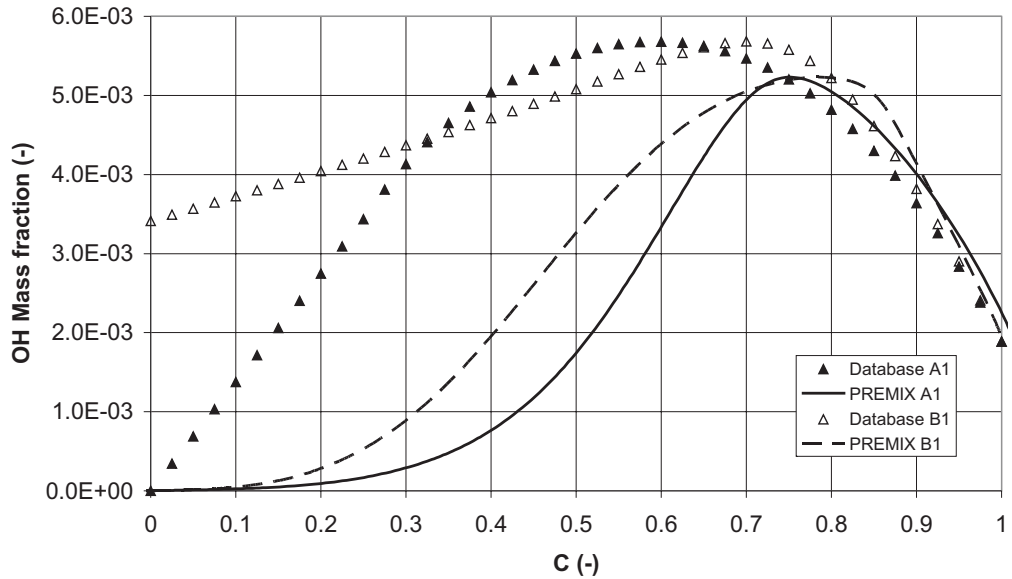
Figure 3.10: Comparison of OH mass fractions of databases A1 and B1, on a RPV basis, with detailed PREMIX solution of case 1.

actual flame solution is seen in figures 3.11 and 3.12. It can be seen there, that due to the very fast rise of c across the flame, the areas where the radical mass fractions are overpredicted are confined to the

flame front area. In these graphs, the temperature of the PREMIX run is included, for an indication of the flame front location. Also, databases C1 and D1 are included in the figure. Database D1 does feature interpolation due to unphysical mass fractions at lower values of c_k, as does database A1.
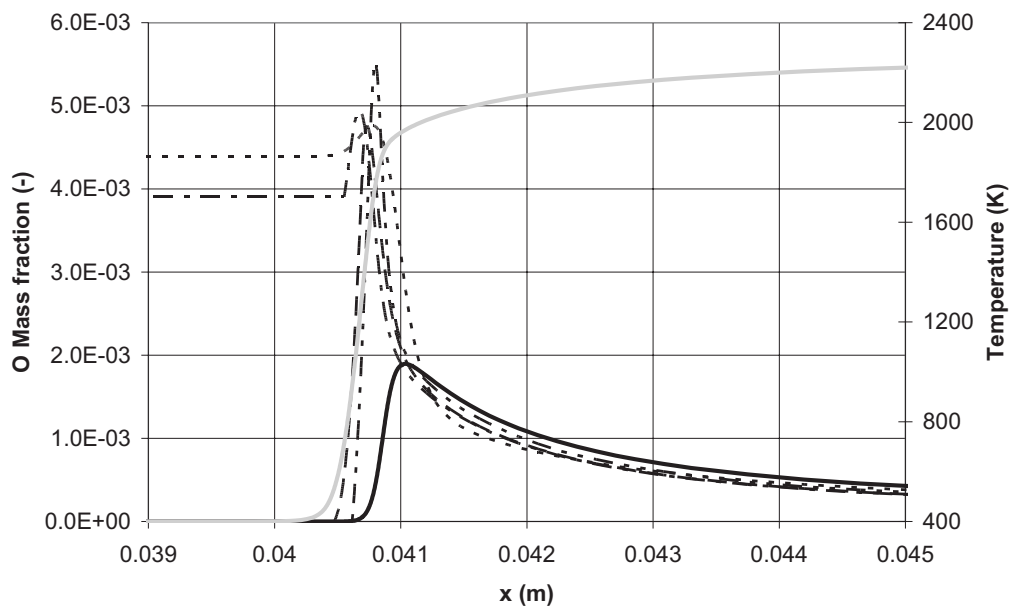
Figure 3.11: Comparison of O profiles with detailed flow solution, case 1. Towards right axis: Temperature (gray solid). Towards left axis: A1 (dashed), B1 (dotted), C1 (dash-dot), D1 (Dash-double dot) and PREMIX solution (black, solid).

From these figures it can be seen that the post flame zone mass fractions are very well predicted, for all cases. The OH profile yields a closer match to the detailed solution than the O profile. Due to the fact that the databases B1 and C1 are not interpolated for low values of c_k, they yield incorrect mass fractions in the pre-flame zone. Databases A1 and D1 yield correct pre-flame mass fractions. Comparing the accuracy of the databases to the detailed flame solution, for the quantities assessed here, in descending order it would be C2-D2-A1-B1. This means that the 2-step mechanism performs better than the 1-step mechanism, and the CSP-mapping is favorable over the manual mapping, for the manual mappings chosen here. It must be said however, that the differences are slight. The 2-step mechanisms do not offer a dramatic improvement of accuracy over the 1-step mechanisms, but the memory requirements of the former are doubled over the latter. Therefore it is concluded that it suffices to use a 1-step reduced mechanism and that if a higher accuracy is required at regions further away from equilibrium, one should opt for 4,5 or even 7-step reduced mechanisms. However, as illustrated in section 2.8.3 this would dramatically increase the memory requirements for the turbulent database, quite probably beyond the capacity of the workstation the calculations are to be performed.

Given the results obtained with databases A1 and B1 shown here, the CSP-mapped b^s of A1 is favored over the manually mapped B^s of B1. The source term prediction is better with database A and the temperature profile is predicted accurately over a large range of values of c. This will result in a better prediction of combusting flow fields in subsequent turbulent simulations, since the temperature and source term values determine the density and the heat release-rate of the flame. Therefore, in
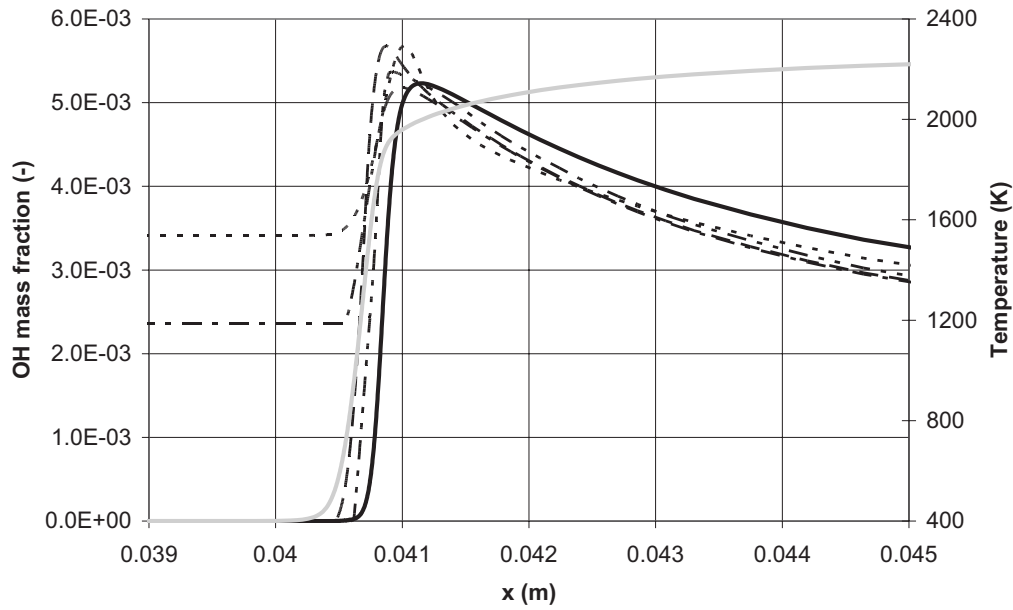
Figure 3.12: Comparison of OH profiles with detailed flow solution, case 1. Towards right axis: Temperature (gray solid). Towards left axis: A1 (dashed), B1 (dotted), C1 (dash-dot), D1 (Dash-double dot) and PREMIX solution (black, solid).

subsequent studies in this thesis the 1-step, CSP-defined reduced mechanism will be used, defined in tables D.3-D.4 and obtained from a CSP-reduction of case 1.
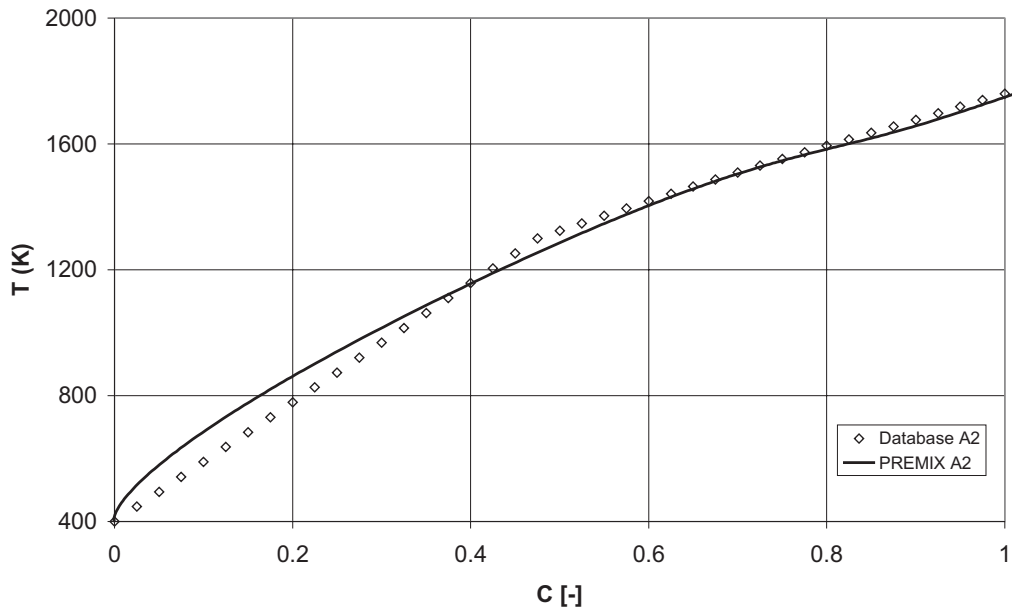

Figure 3.13: Comparison of Temperature profiles of database A2 with the detailed solution of case 2, on a RPV basis.

The 1-step CSP-mapped reduced mechanism is compared to results obtained from the lean case 2.
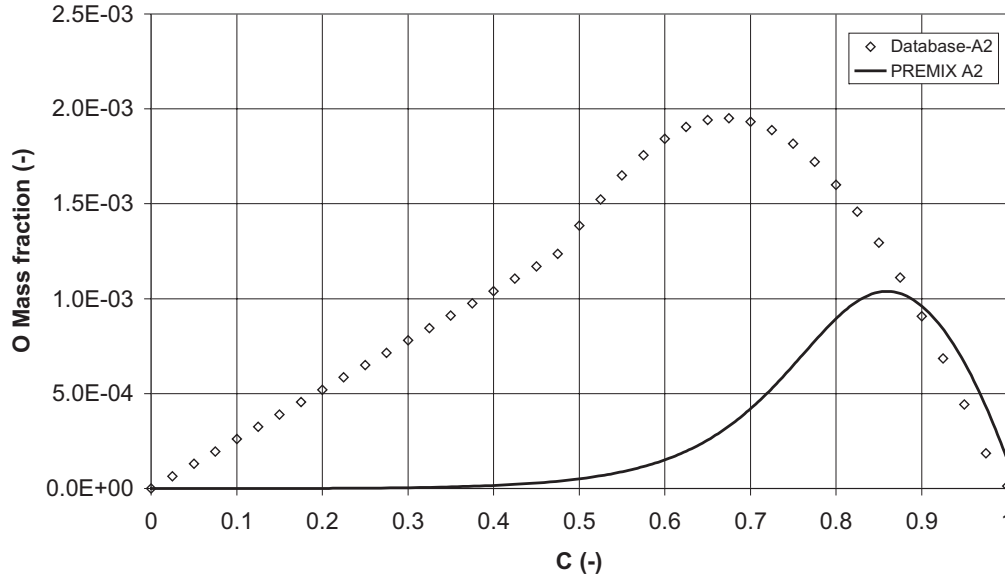
Figure 3.14: Comparison of O mass fraction of database A2, on a RPV basis, with the detailed flame solution of case 2.

For this reason, a database A2 has been created using the 1-step CSP-mapped reduced mechanism for the boundary conditions of this run, which are provided in table 3.1. Then for the detailed PREMIX solution of this case, $c(x)$ was determined to be able to compare the database to the detailed flame result obtained with PREMIX. In the database, interpolation was employed due to negative mass fraction of CO in the solution beyond the threshold value for $c < 0.5$, at which point the temperature is $1300K$. The temperature comparison of database A2 and the premix run is given in figure 3.13. Again the smooth profile of temperature versus RPV is noticed, for both the detailed PREMIX flame solution and the database. In figures 3.14 and 3.15 the O and OH radical mass fractions are compared on a RPV basis. It can be seen that the O radical peak mass fraction is now overestimated by a factor of 1.9, instead of 2.5 for the stoichiometric case 1. Also the O radical profile is more similar to the detailed solution than in case 1, as is the OH profile. However, the PREMIX and database profiles follow each other only for $c > 0.9$, in contrast to $c > 0.7$ of case 1.

How these results influence the actual flow solution comparison is displayed in figures 3.16 and 3.17. It can be seen that the database profiles fall off earlier than the detailed PREMIX flame solution, which was less the case in the stoichiometric comparison. The OH peak value of the database compares equally well to the detailed solution as in the stoichiometric case, the O peak value comparison is better than in case 1. Again, thanks to the steep rise in c across the flame front, the region of overpredicted radical concentrations is limited to a small region in space, as was the case in the stoichiometric comparison. However, it can be concluded from these results, that the lean case yields less accurate results than the stoichiometric case, as was to be expected. The lower overall temperatures in the lean case yield less valid steady-state relations over a broader range of c than case 1.
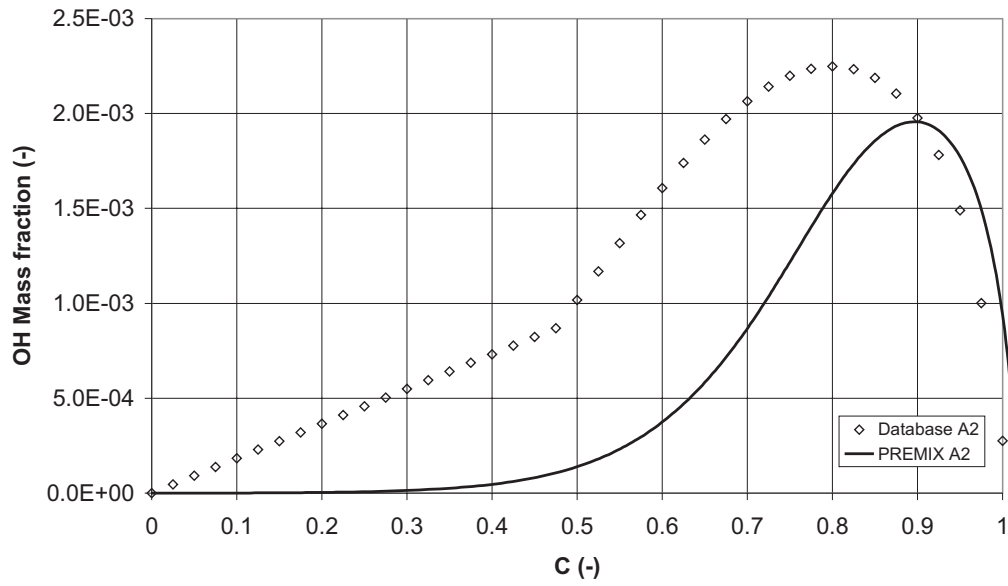
Figure 3.15: Comparison of OH mass fraction of database A2, on a RPV basis, with the detailed flame solution of case 2.
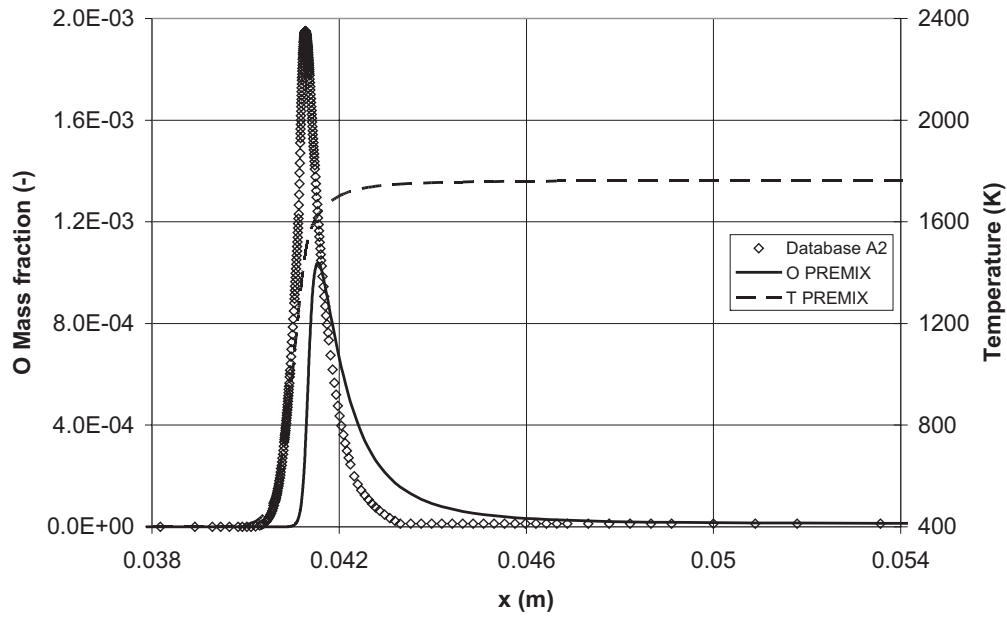

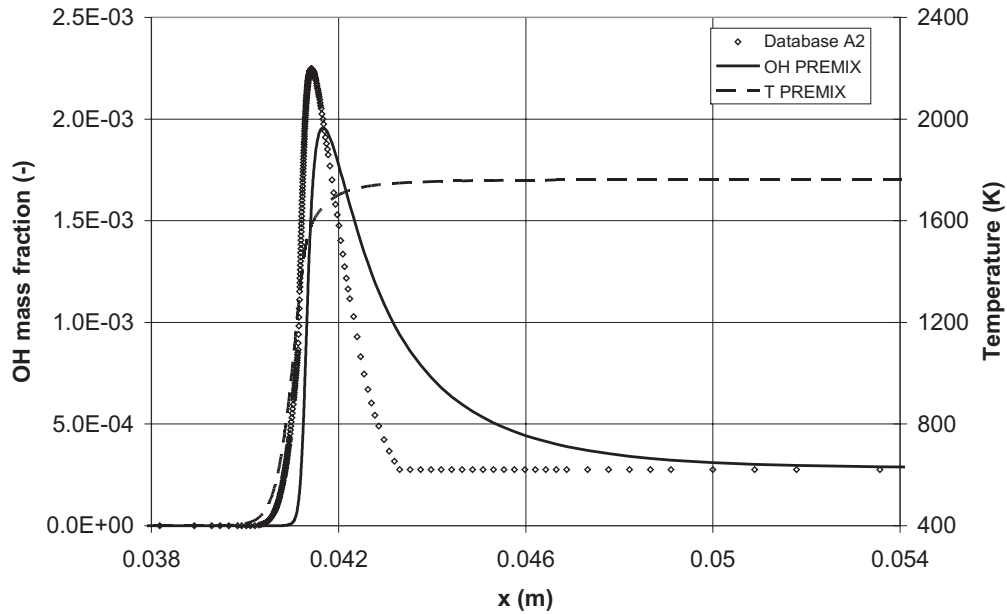Figure 3.16: Comparison of O mass fraction of database A2 with the detailed flame solution of case 2.

Figure 3.17: Comparison of OH mass fraction of database A2 with the detailed flame solution of case 2.

3.5   Prediction of NO

In section 2.10.4 the Zeldovich thermal NO mechanism was presented as the means to calculate the NO emissions by the flame. Here, it will be shown that the steady-state assumption of NO will not yield accurate results. In figure 3.18, a logarithmic NO plot is made as function of x. It can be seen from this result that the database prediction is half a decade off with respect to the detailed flame solution. For case 2 and database 2A, this is even worse. Using the steady-state assumption for NO will therefore lead to overpredictions of the NO emissions of flames. For that reason the Zeldovich mechanism is used to predict NO emissions, presented in section 2.10.4. It requires the solution of an extra transport equation, for which the source term is calculated and stored in the turbulent database.

The NO predicted from the Zeldovich mechanism depends on the O radical concentration, which is predicted with much higher accuracy than is NO. However, from the previous section it can be estimated that using the database together with the thermal NO mechanism to predict emissions from lean premixed turbulent flams might yield an underestimation of the thermal NO emissions. This is because of the under estimation of the O radical concentration in the high-temperature region of the flame. However, for a verification of this assumption, comparisons must be made with NO measurements of turbulent flames.

3.6   Conclusion

In this chapter, laminar databases were assessed, created for the simulation of premixed, adiabatic flames. Both CSP-defined as well as manually defined reduced chemistry mappings were employed. They were compared to results of laminar flame solutions with the full chemical reaction mechanism.
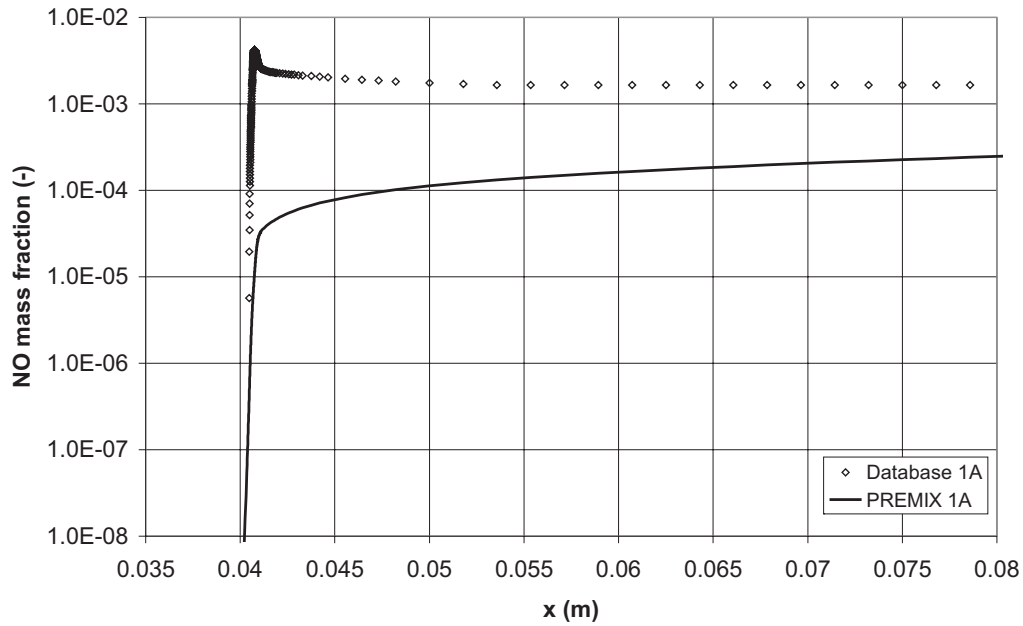
Figure 3.18: NO mass fraction comparison of case 1 with database 1A.

It is shown that at the stoichiometric case, the reduced mechanisms compared well to the detailed flow solution. The comparison was best for CSP defined reduced chemistry, and for the 2-step reduced mechanisms. However, the differences between the 1-step and the 2-step mechanisms were too slight to necessitate the use of the 2-step mechanism in subsequent turbulent flame simulations. Also, the results obtained with the 1-step CSP-mapped reduced mechanism were better than those obtained with the manually mapped 1-step reduced mechanism, in the comparison of temperature and source term values. For this reason, the 1-step, CSP-mapped reduced mechanism is chosen for use in subsequent turbulent flame simulations.

It was shown that the use of the steady-state relation NO will lead to overpredictions of NO emissions if this was to be used in turbulent flame simulations. Instead the Zeldovich mechanism will be employed, which is described in section 2.10.4. It is estimated that the use of this mechanism together with the CFI database might yield an underestimation of NO emissions in premixed, lean turbulent flame simulations, but this needs to be verified in comparisons of NO measurements and simulations of turbulent flames.

From a comparison of a database of the 1-step, CSP mapped reduced mechanism with a detailed laminar flame solution of a lean premixed laminar flame, it is shown that the comparison is less accurate than for the stoichiometric case. The reason is sought in the fact that the steady-state relations might be less valid in this case, where temperatures are lower, and that the low-dimensional manifold might be less adequately defined there. However, the peak radical mass fractions compared to the detailed flame solution equally well as was the case in the stoichiometric comparison, and the exit profiles were also predicted accurately.

Chapter 4

The influence of steam on combustion

As described in the introduction, one of the means of improving the gas turbine performance is the injection of steam upstream of the combustion chamber, e.g. by injecting water into the compressor, or by installing a evaporator behind the compressor exhaust. On the influence of steam on premixed or partially premixed combustion, little information is available. In this section, the influence of steam on combustion will be assessed using turbulent flow calculations in a scale model of a gas turbine combustor and using laminar flame calculations with the CHEMKIN PREMIX code. The turbulent combustor comprises a swirling, partially premixed, atmospheric flame, with methane as fuel. The burner geometry originates from DLR (Deutsches Zentrum fur Luft und Raumfahrt), measurements with this burner on dry atmospheric combustion are published in refs. [13], [19] and [61].

In the cases of this study the adiabatic flame temperature is kept constant to eliminate its effects on the production of NO. It is a well-known fact that lowering the flame temperature, e.g. by reducing the fuel equivalence ratio to leaner values or by adding diluents without modifying the fuel-air mixture, reduces NO emissions, see e.g. ref. [5]. The simulations deal with partially or fully premixed flames. The reducing effect of peak temperature reduction on the emission of NO by steam admission, as described by Bhargava *et al.* [5] is avoided here. The effect of fuel dilution by nitrogen or steam on emissions will be eliminated by plotting the emissions on a g/GJ basis, using the lower heating value of the fuel. To assess the chemical effect of added steam to the flame a case is created where the water volume flow is replaced with an equal amount of nitrogen.

Description	Fuel	Air	Diluent	T^{in}	T^{ad}	ϕ_F	ω	Power
	$[g\,min^{-1}]$	$[g\,min^{-1}]$	$[g\,min^{-1}]$	$[K]$	$[K]$			$[kW]$
Base case	38.93	1094.8	0	400	1757	0.60	0	32.5
Steam case	40.84	930.58	107.47 (H_2O)	400	1757	0.73	2.63	34.1
N2 case	38.84	930.58	159.43 (N2)	400	1757	0.69	4.10	32.4

Table 4.1: case descriptions. ω is defined as the ratio of mass flows of diluent and fuel, ϕ_F is based on the air and fuel flows only.

The cases that are performed are summarized in table 4.1. A few remarks can be made with respect to these cases and their setup. It is assumed that there are 2 basic inlets, one for fuel and one for oxidizer. The diluent is added through the oxidizer inlet. Adding diluent in high quantities, such as those required for evaporative cycles such as HAT, through the fuel inlet requires modification of

the fuel nozzles, or even the complete burner. This will therefore not be the the preferred choice for a burner developer. Replacing air flow by diluent, keeping the total volume flow through the oxidizer inlet constant, does not require modifications of the burner and does not modify the burner flow field significantly. This choice is adopted here. However, when this is done, the power of the burner has to be modified accordingly when adding diluents to maintain a constant overall adiabatic flame temperature. This is reflected in table 4.1, it can be seen however that the fluctuation in power is only about 5% between the different cases.

The boundary conditions for the Base case are a modified version of those presented by Weigand *et al.* [61] as case A. In that reference measurement results are shown on the DLR test combustor that is also adopted here. This case proved to burn very stable, therefore it has been chosen as a basis for the numerical simulations. The overall adiabatic flame temperature of case A is around 1750 K, at an inlet temperature of 295 K. The inlet temperature has been raised to 400 K here. This ensures that all H_2O is present in gaseous form. The burner power has been modified accordingly to keep the adiabatic flame temperature constant. This results in the Base case. From this base case, 15 vol.% of steam is included, keeping the total volume flow constant. This volume is according to the requirements for mixed cycle combustion, described in section 1.3. The burner power is adjusted to keep the adiabatic flame temperature identical to that of the Base case. This results in the Steam case, with 11.6% of the air mass flow in the form of steam. In the N2 case, the volume flow of steam is replaced by nitrogen, again modifying the burner power to yield a constant overall adiabatic flame temperature. This means the added N2 mass flow is 17% of the air flow in this case.

Although the volume flows through the oxidizer inlet are equal in all cases, the mass flows are different. This might affect the momentum flow of the oxidizer inlet. However, it can be assumed that the flow is Reynolds independent. This means that the flow is independent of the (air) boundary condition, for Reynolds numbers greater than a certain threshold. Measurement results in ref. [61] show that this is the case for the flames considered there, with air flows changing from 281 to 1095 $g\,min^{-1}$. It can therefore be assumed that the flames simulated here will also be in the independent Reynolds number range. The influence of the fuel jet can be neglected with respect to the air jets in the burner mouth. The total heat capacity flow of the oxidizer inlet is nearly constant, yielding the identical adiabatic flame temperature as in the Base case for almost the same burner power.

The calculations are performed adiabatic, the enthalpy scalar i is taken identical 1. This methodology will not reveal any differences due to radiation between the cases. However, measurements on a similar partially premixed laboratory-scale burner with approximately identical adiabatic flame temperatures, presented in ref. [34], showed that radiation was not a significant factor there. This can be concluded from the graphs of $ln(\text{NO})$ versus the inverse of temperature, consisting of straight lines. This is especially the case for the highest Reynolds number flow considered, the 20 kW, 1 bar case. The results of this case will also be discussed in this chapter.

For these 3 cases, both laminar and turbulent simulations will be performed. The laminar simulations will be done presuming the mixture is perfectly mixed at the overall values mentioned in table 4.1. A perfectly premixed, freely propagating methane-air flow will be simulated using the CHEMKIN PREMIX package [28]. The turbulent flame simulations are performed using the commercially available package CFX-5.6 from Ansys [3].

The setup for this chapter is as follows. First, the laminar calculations will be presented and discussed. Then the burner and turbulent calculation setup will be presented and finally the results of the 3 cases discussed.

4.1 Laminar assessment

The laminar flames are calculated with the 1-dimensional premixed flame code PREMIX [28]. The calculations were performed in an identical manner to those in section 3.1. The final number of grid points is approximately 300, the absolute and relative tolerances are 10^{-6} and 10^{-12}, respectively, the velocity correction formalism is used to ensure mass conservation and mixture averaged transport properties are used. The computational domain is $10\,cm$ in length. The GRI-Mech 3.0 mechanism [55] is again used.

A zoom of the temperature profiles of the 3 cases is shown in figure 4.1. Although inlet and adiabatic flame temperature are different, there are minute differences in the temperature rise across the flame front. The onset of the temperature rise is equal in all cases, but the slope is slightly different. The Steam case has the lowest slope, followed by the N2 case and the Base case, respectively.
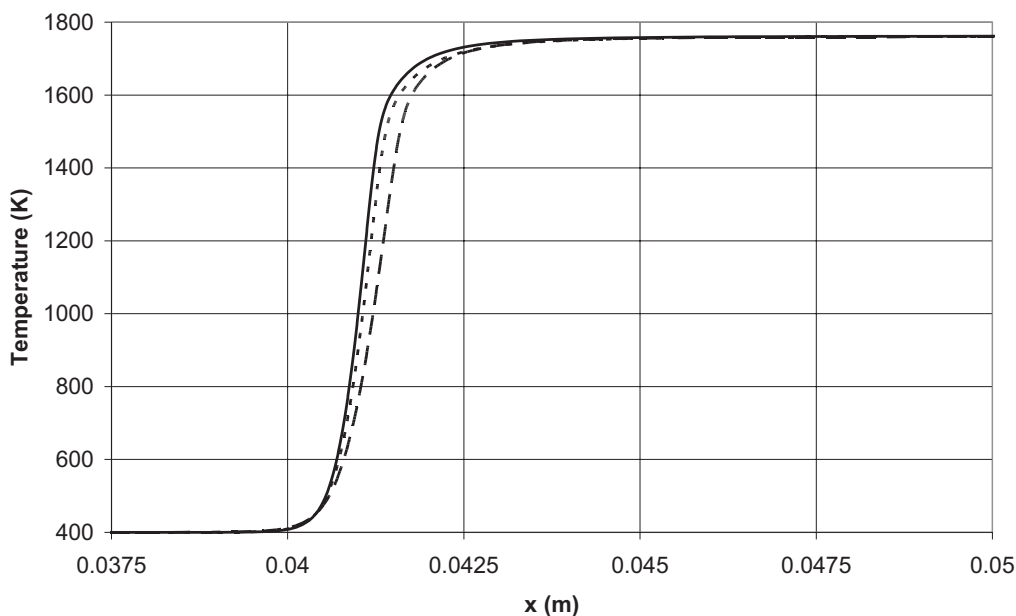
Figure 4.1: PREMIX calculations, temperature profiles of the base case (solid), steam case (dashed) and N2 case (dotted).

The NO profiles of the different cases are shown in figure 4.2. It can be seen that although the temperature profiles are almost exactly identical, there is a large difference in the production of NO. The plots are normalized with the fuel heat release rate, which is $50.145\,10^{-6}\,GJ\,g^{-1}$, to compensate for the dilution caused by nitrogen and steam, respectively. The NO mass fractions at domain exit ($x = 0.1m$) are 2.5, 1.8 and 3.2 $g\,(GJ)^{-1}$ for the Base case, Steam case and nitrogen case, respectively. To explain these differences and to illustrate the formation of NO in this flame, a plot is shown in figure 4.3 of selected mass fractions and their source terms. Mass fractions are represented by solid lines and refer to the right vertical axis, source terms are represented by dashed lines and refer to the left vertical axis. It should be noted that only the N2 source term is plotted, not its mass fraction.

From this figure it can be observed that the source term of NO (1a) initially becomes negative, before NO (1b) is even present. This can be explained using the NO2 (4a, 4b) graphs. Above ap-
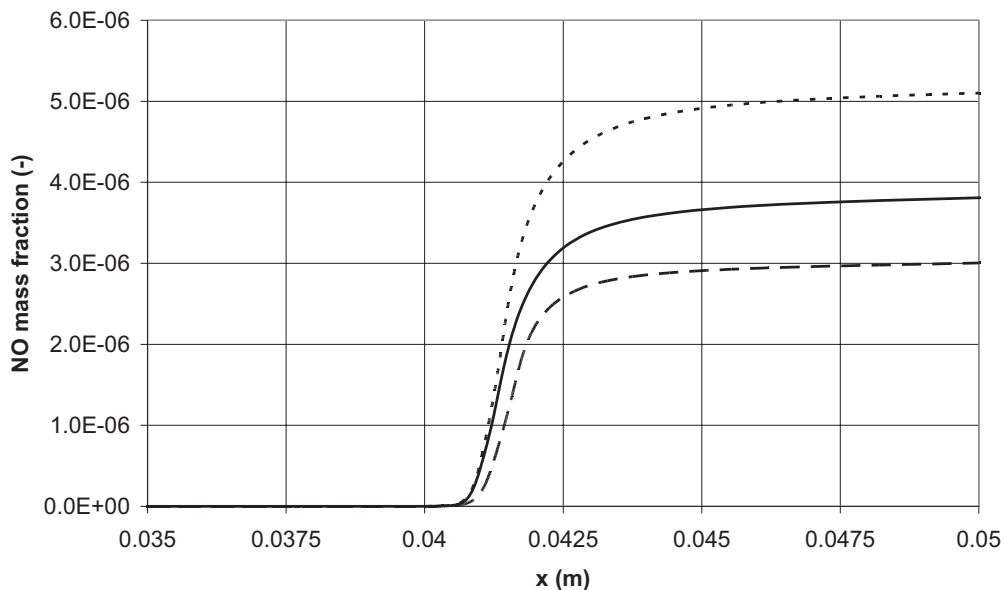
Figure 4.2: PREMIX calculations, NO profiles, in g per GJ of the base case (solid), steam case (dashed) and N2 case (dotted).
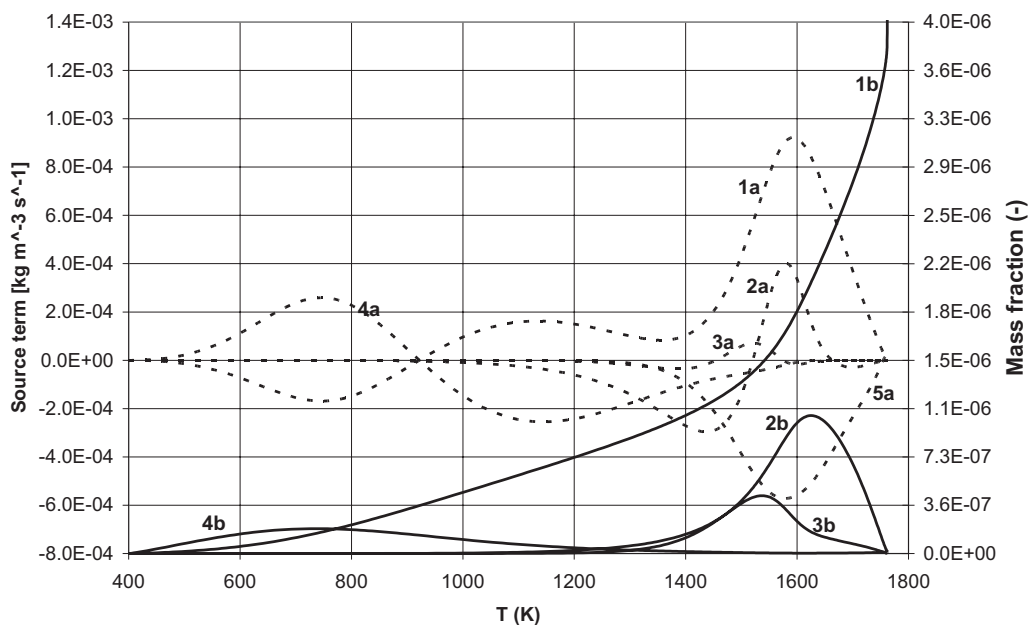

Figure 4.3: PREMIX Base case, mass fractions and source terms plotted as function of temperature. 1: NO, 2: O, 3: N, 4: NO2, 5: N2. Dashed lines (a): source term (linked to left axis), solid lines (b): mass fraction (linked to right axis).

proximately 1250 K, N2 starts to dissociate and NO is formed. This NO, amongst others, diffuses upstream. At low temperatures, this is immediately transformed to NO2, as the NO- (1a) and NO2 (4a) source terms show. At temperatures above 920 K, the NO source term is positive. At first, this is because NO2 is consumed back to NO, as the NO2 source term shows. At temperatures above approximately 1380 K, the majority of the NO production originates from the thermal mechanism, through the association of N (3) and O (2) radicals. The dip in the NO source term around that temperature shows that the NO2 - NO mechanism is fading while the thermal NO mechanism has not yet initiated. At around 1600 K the NO source term reaches its peak. Beyond this temperature there is a linear decay of the source term in temperature, which is an exponential decay in space (not shown here). The growth of the NO mass fraction in the post-flame zone is small compared to the growth in the flame zone, although it is still significant, about 18%.

The thermal mechanism is responsible for the majority of the NO production. As shown here, the production of NO through NO2 is mostly originating from NO2 that was formed from upstream diffused NO in the pre-flame zone and does therefore not yield a significant net production of NO. The thermal NO mechanism is dependent of temperature, and of the O and N mass fractions. From figure 4.3 it can be seen that the O radical mass fraction already decays while the N radical mass fraction has not yet reached its peak. This misalignment reduces the possible NO production in the flame zone of this case: not all O radicals convert to NO since at that region in the flame there is a shortage of N radicals needed for recombination.

The major origin of the exhaust NO value lies in the peak value of the source term which is attained just behind the flame zone. after this peak value, the temperature is constant and identical for all cases, and the decay of the NO source term is also identical for all cases. Therefore, the higher the peak NO source term value will be, the higher the exhaust NO mass fraction will be, for the cases considered here. Indeed, in the Steam case this peak value is lower, while in the N2 case it is higher than the Base case value. In figures 4.4 and 4.5, the mass fraction- and source term graph versus temperature of the Steam case and the N2 case are shown, respectively. In these figures, the origin of the differences in peak source term values can also be traced. Since the thermal NO mechanism is dependent on the N- and the O mass fraction, both play a role here. In the N2 case, the N- as well as the O mass fraction have an overlap of areas with high mass fractions. It can also be seen that, due to the chemical action of H_2O, the peak O radical value in the Steam case is a factor of 2 reduced with respect to the Base case, while the N2 case shows an almost identical peak O value to the Base case. The N mass fraction is increased in both the Steam case and in the N2 case. The combination of high N- and O mass fractions at higher temperatures and in a wider range of temperatures than in the Base case, yields the higher peak NO source term of the N2 case. In the Steam case on the other hand, the peak value of O being lower than the N peak value in the high-temperature range, causes the NO source term peak value to be lower than in the Base case.

It can be concluded from this assessment that the differences in NO emissions of these flames originate in a very delicate system. In the onset of the NO production, in the N2O - NO path, diffusion plays an important role. In the thermal NO production, the locations of the peak N and O mass fractions with respect to the local temperature determine the peak NO source term value and hence the final NO mass fraction of these flames. This is due to the fact that the initial and final temperatures are identical in these cases, which yields an identical post-flame behavior for the NO production. It can be anticipated that in turbulent flames, where diffusion is much more efficient due to turbulence action, the reasonings and explanations given here cannot easily be translated. Turbulent fluctuations,
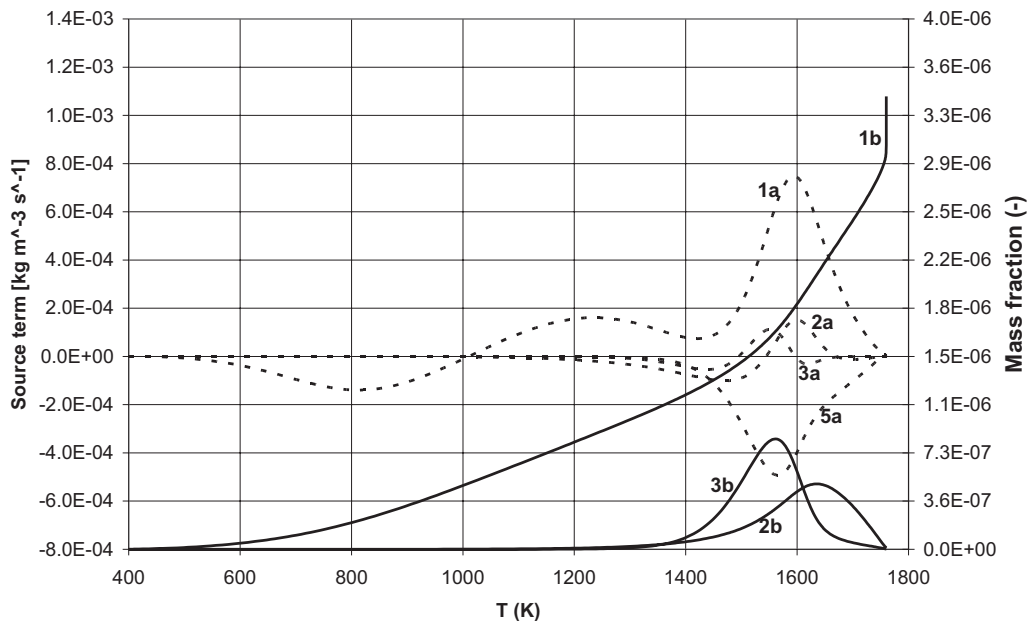
Figure 4.4: PREMIX Steam case, mass fractions and source terms plotted as function of temperature. 1: NO, 2: O, 3: N, 5: N2. Dashed lines (a): source term (linked to left axis), solid lines (b): mass fraction (linked to right axis).
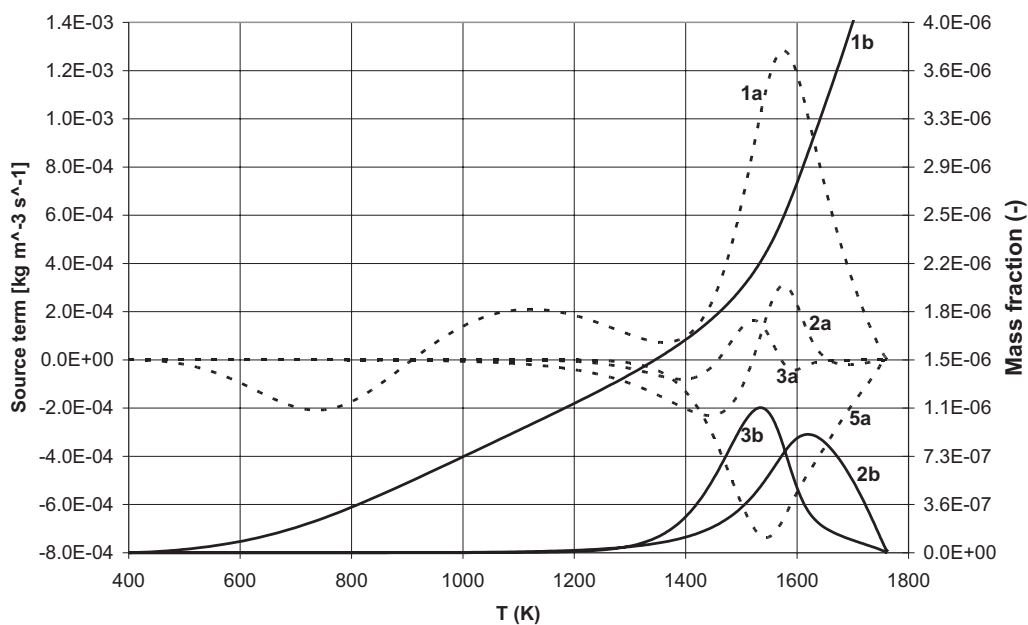

Figure 4.5: PREMIX N2 case, mass fractions and source terms plotted as function of temperature. 1: NO, 2: O, 3: N, 5: N2. Dashed lines (a): source term (linked to left axis), solid lines (b): mass fraction (linked to right axis).

not only in the fluid but also in the reacting scalars, play a dominant role, yielding a completely different picture than the one presented here for laminar, 1-dimensional premixed flames. Moreover, in the turbulent flames presented here, the local mixture fraction value and variation can also play a major role in the production of NO. In the subsequent section, the influence of steam on the production of NO in turbulent flames will be assessed.

4.2 Turbulent combustor

The influence of steam on turbulent combustion will be assessed using the DLR test combustor geometry, described in [13], [19] and [61]. It is a modified version of a gas turbine combustor. A schematic of the combustor is shown in figure 4.6. Air is supplied to the combustion chamber through a central nozzle and an annular nozzle, both equipped with radial swirlers. The swirl direction is the same in both swirlers. The central nozzle ("central swirler")has a diameter of 15 mm, the annular nozzle ("outer swirler") has an inner diameter of 17 mm and an outer diameter of 25 mm contoured to 40 mm, ending on a flange with diameter 85 mm and thickness 4.5 mm. The outer swirler provides roughly 60 mass% of the air to the combustion chamber, the inner swirler roughly 40%. Both swirlers are fed through a single air inlet, located upstream of the swirlers, at the lower end of the cylinder with diameter 79mm. The outer swirler is connected to the air inlet via 24 tubes of 5mm diameter. Fuel is injected in an annular nozzle between the 2 air inlets, and is not swirling. The nozzle consists of 72 channels of 0.5×0.5 mm, ensuring a good cylindrical symmetry. The fuel nozzle is fed through 3 tubes, located equidistantly on the circumference, again for reasons of cylindrical symmetry. The exit planes of the fuel nozzle and central air swirler are located 4.5 mm below the exit plane of the outer swirler. The origin of the frame of reference for measurements is taken on the rotational symmetry axis, at the exit plane of the outer swirler.

The combustion chamber is square with 85 mm sides. It consists of quartz glass walls connected by steel posts of diameter 10 mm. Its length is 114 mm, as shown in the figure. A circular contraction is fitted at the exit of the combustion chamber, avoiding flows of the exhaust back into the combustion chamber. The quartz walls allow a very good optical access to the combustor flow field.

4.3 Numerical simulations setup

The numerical simulations are performed using the commercially available package CFX-5.6 from Ansys [3]. The finite-volume flow solver uses a single-cell, collocated grid to overcome the decoupling of pressure and/or velocity. The equations are solved using a coupled flow solver, solving the hydrodynamic equations as a single system. The solution approach uses a fully implicit discretization of the equations. For more details regarding the package and its solution procedure, the reader is referred to the manual, ref. [4]. The calculations are performed on a Linux cluster, consisting of 5 units. Each unit is equipped with 2 Xeon 2.6MHz CPUs and 2GB of RAM memory. The clusters are interconnected through a 1Gbit local area network. The package Redhat is used as operating system. Each calculation is performed on 5 CPUs, allowing 2 jobs to run at the same time.

The CFI combustion model is used, as described in chapter 2. The detailed reaction mechanism is mapped onto 1 scalar, the CSP-defined mapping of section 3.2, described in Appendix D is used for
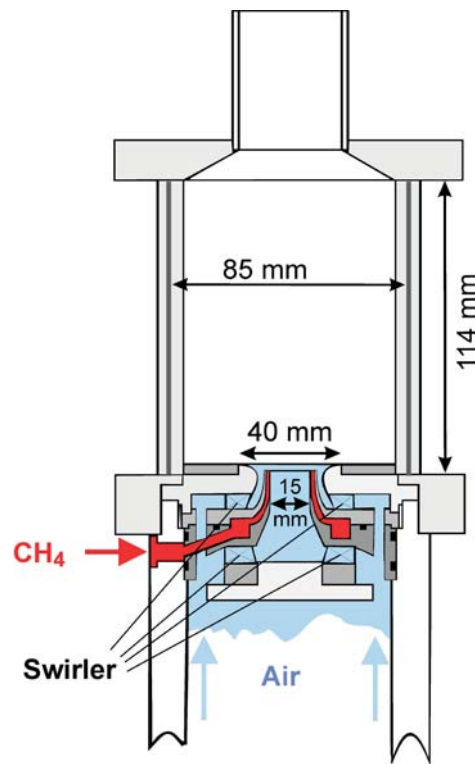
Figure 4.6: Schematic drawing of combustor. Taken from [61], with permission.

all cases. For the laminar database, 40 points were used in the division of the c scalar, the increment in the f scalar is $\frac{1}{400}$. In the turbulent databases, the number and division of mixture fractions obtained in the laminar database calculations is used for the mean of mixture fraction. Means of c and variances of c and f are calculated for 11 values, with a linear division for the means and a 4th order polynomial for the variances. Only solutions with a temperature larger than $1100\ K$ were stored in the database, other values were obtained by linear interpolation.

In the numerical simulations, the means and variances of mixture fraction and reaction progress variable are solved. The $k - \varepsilon$ turbulence model, described in section 2.4 is used.

It was decided to model the entire combustor, from fuel inlet to combustor exhaust. This is done to ensure an accurate flow field into the combustion chamber from the air swirlers. The fuel inlet, which consists of numerous small rectangular ducts, is replaced by an annulus with identical cross sectional area. This greatly simplifies numerical simulations at hardly any cost of accuracy. The impulses and the mixing of these individual fuel jets with the incoming air jets will be underestimated by using a single annular inlet, but since the impulse differences between the air and fuel streams are large, this is expected to be insignificant. The ducts were created to improve axial symmetry of the fuel inlet, which is guaranteed by the inlet conditions of the numerical simulations. The fuel supply lines are also removed from the flow domain, it is assumed that the fuel will enter perpendicular to the fuel inlet annulus, again an assumption that is thought to be accurate. Furthermore, in the actual combustor the inner swirler is held by a flange which is connected to the main body with 2 screws. It is believed that the flow obstruction that arises at the inner swirler inlet, due to these screws, has negligible consequences for the flow inside the combustor. For this reason these screws have been
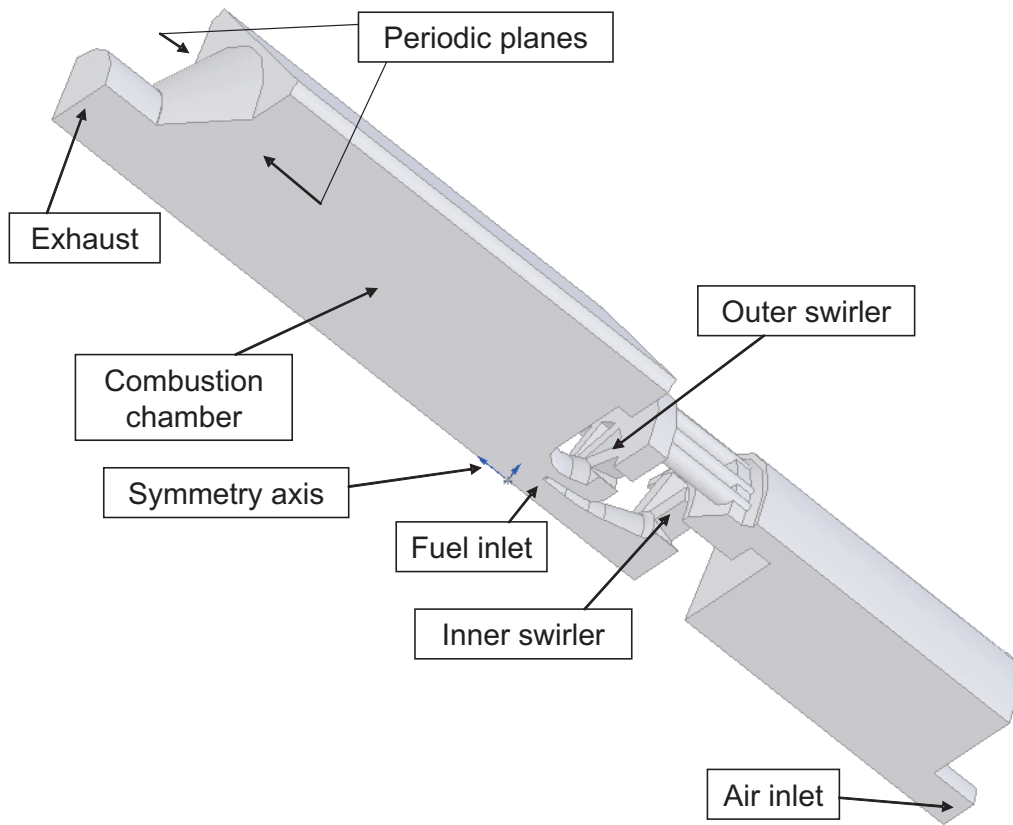
Figure 4.7: Flow domain used for numerical simulations. Flow direction is from bottom right towards top left.

removed in the final flow geometry

With the fuel supply lines and connecting screws removed and the fuel inlets replaced by a single annulus, the flow geometry is axial symmetric, with symmetry planes through the mid-planes of the side walls of the combustor. Using these symmetry considerations, it is possible to resolve only a quarter of the domain in the numerical simulations and compensate using periodic boundary conditions for these symmetry planes. This greatly reduces the memory and computational requirements of the simulation, at little cost of accuracy. Using this symmetry will not resolve non-symmetrical features of the flow, such as a precessing vortex core. However, this was not reported to exist in the publications with this combustor, for the case chosen to use as a basis for the simulations [61]. The resulting flow domain is given in figure 4.7, a closeup of the swirlers (in reverse angle) is shown in figure 4.8. The sides of the quarter slice of the combustion chamber represent the periodic boundaries. From these figures it can be observed that both air swirlers are fed through the same air inlet. The outer swirler is connected to the air inlet through the axial tubes, as can be seen in figure 4.8.

To further reduce the computational requirements of the combusting flow simulations, an extra measure was taken. It proved to be beyond the capabilities of the used cluster to create a grid dense enough for an accurate combusting flow simulation in the geometry described above. Therefore it was chosen to simulate only the cold flow with this geometry. A second geometry is created, which consisted only of the combustion chamber, the fuel inlet and part of the swirler exhaust piping. At the cut-plane the velocity and turbulence fields are recorded and used as inlet boundary conditions
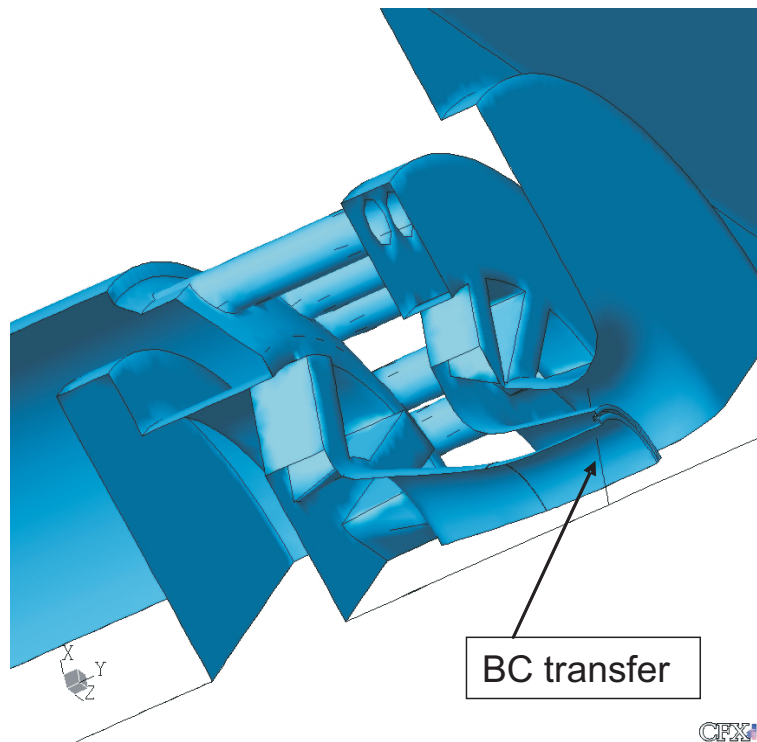
Figure 4.8: Swirler detail shown in reverse angle of figure 4.7. Flow direction is from bottom left to top right. Also shown here is the line 'BC transfer' on which data is taken for boundary condition transfer between complete and reduced geometry.

for the simulations with the reduced geometry. Here axial symmetry of these quantities is assumed, which allows the data transfer based on the line data shown in this figure. The line on which the data is recorded for boundary condition transfer is shown in figure 4.8. This figure shows a detail of the swirlers and fuel inlet. In the grid independency simulations shown in appendix E, this axial symmetry proved indeed to exist. Moreover, it was ensured in test calculations that recirculating hot gases do not enter this cut-plane and that it only contains (cold) flow *in*to the combustion chamber. For this reason this boundary condition transfer is allowed and will not affect the results. The boundary condition transfer plane is located 8 mm upstream of the burner exit plane. The burner exit plane is also the origin of the coordinate system.

   Axial cross sections of the grids that are created for the simulations are shown in figure 4.9. At the wall boundaries, a inflated boundary has been created of 1 mm thickness, consisting of 4 layers. These layers enhance the quality of the simulation in the near-wall regions, for more details see ref. [3]. The complete geometry consists of $930 \cdot 10^3$ elements, the reduced one of $840 \cdot 10^3$ elements. This means that the grid density is much higher in the reduced geometry, improving the quality of the flow simulation there. Cold test calculations with both geometries showed grid independence in the combustion chamber, between the grids on these two geometries. It is assumed that this will also be the case for the combusting flow simulations on the reduced geometry. Unfortunately, due to the limitations of the used cluster this could not be tested. The grid independency study is presented in appendix E.

   In the following subsections, first a discussion will be presented on the results of the Base case,
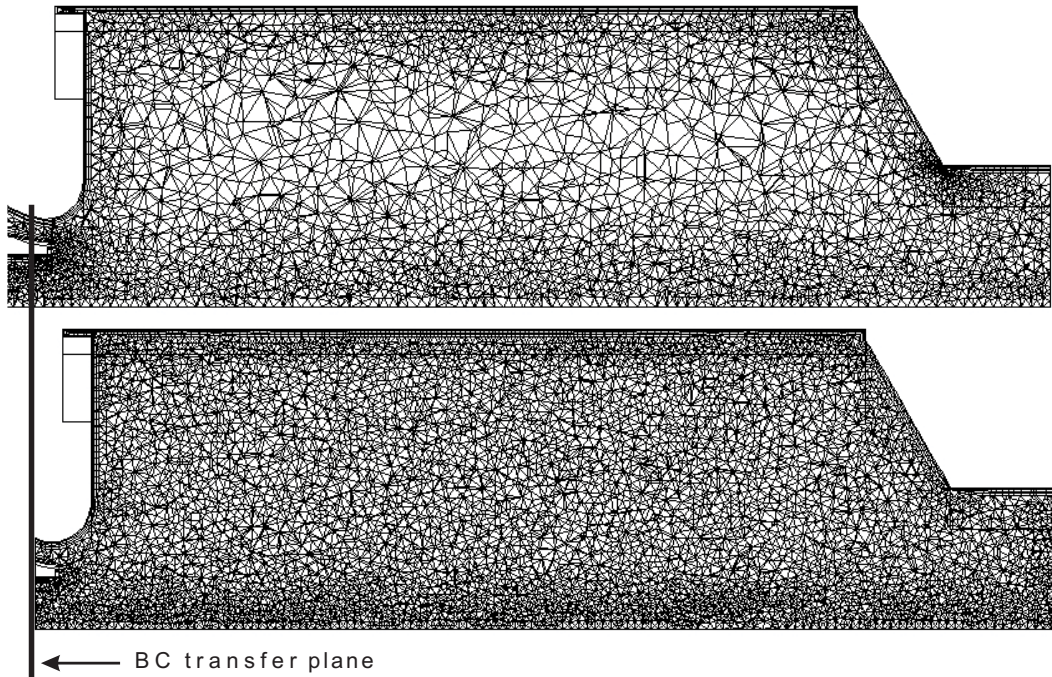
Figure 4.9: Grids created in complete geometry (above) and reduced geometry (below). Shown is an axial cross section through the mid-plane of a combustor side wall. Flow direction is from left to right.

with respect to the laminar database that is used, and with respect to the combusting flow field. Then the different cases will be discussed.

4.3.1 Base case

The base case, as shown in table 4.1, is a dry case, with a fuel equivalence ratio of 0.6 and a burner power of 32.5 kW. With an inlet temperature of 400 K this yields an overall adiabatic flame temperature of 1757 K. The laminar database that is used consists of cold compositions varying between methane at the fuel inlet and air at the oxidizer inlet. First, some features of the laminar database that is used (in Favre-averaged form) in the turbulent flame simulation are shown. Then the turbulent flame results will be discussed.

4.3.2 Laminar Database

In figure 4.10, the interpolation scalar is shown as a function of c and f. Values identical 0 mean that that the function values at that point are the solution of the system of equations, defined in expressions (2.111), rather than obtained by interpolation. In the latter case a value of 1 is assigned to this point. Therefore, in figure 4.10 all calculated points can be obtained. The figure shows only values of $c > 0.4$. This is done since the actual flame simulations will not reach values below this value of c. Also, the temperatures are much lower in this region than their adiabatic values. It can be argued that the steady-state relations are less valid in this region and that the low-dimensional manifold is ill-defined. Also, only the region is shown where at least the equilibrium point is obtained by calculation.

This is for mixture fractions $0.0175 < f < 0.1475$. Numerical results with mixture fractions beyond these values were below the threshold of 1100 K and were assumed to be beyond the flammability limit of the mixture.

It can be seen that in the region around the stoichiometric value of mixture fraction $f = 0.0575$, for values of $0.03 \lesssim f \lesssim 0.1$, all values are obtained by calculation. Starting at $f \simeq 0.11$, a region is seen where, starting from $c = 1$, less points are obtained by calculation. This means that values of $c < 1$ are obtained in increasing number by interpolation. This region increases up to $f = 0.12$ where only the equilibrium point is obtained by calculation. For values of $f \gtrsim 0.12$, a small region exists where results are again obtained by calculation. The size of this calculated rich region increases with mixture fraction, until the threshold temperature is reached for the solution at $f = 0.1475$, where the calculation procedure is broken off since the rich flammability is reached. It shows the power of the method, that it is able to solve the system of equations for values at and away from equilibrium from lean towards rich mixture fractions.

From this figure an item of the discussion in section 2.10.3 can also be outlined. It can be seen that at a mixture fraction of 0.03 solutions have only been obtained up to RPV values of 0.975, which is 1 grid point away from equilibrium. However, the neighboring loops of RPV, at slightly different mixture fractions, converge up to RPV values of around 0.5. This illustrates that the calculation procedure could have benefitted from a multidimensional initial guess, which would have lied closer to the actual solution at that point.

In figure 4.11, the temperature is plotted of the laminar database of the Base case. The maximum temperature is located at equilibrium (RPV $= c = 1$) and at the stoichiometric mixture fraction, $f = 0.0575$, as one might expect. Also, temperature decreases for values of c further away from
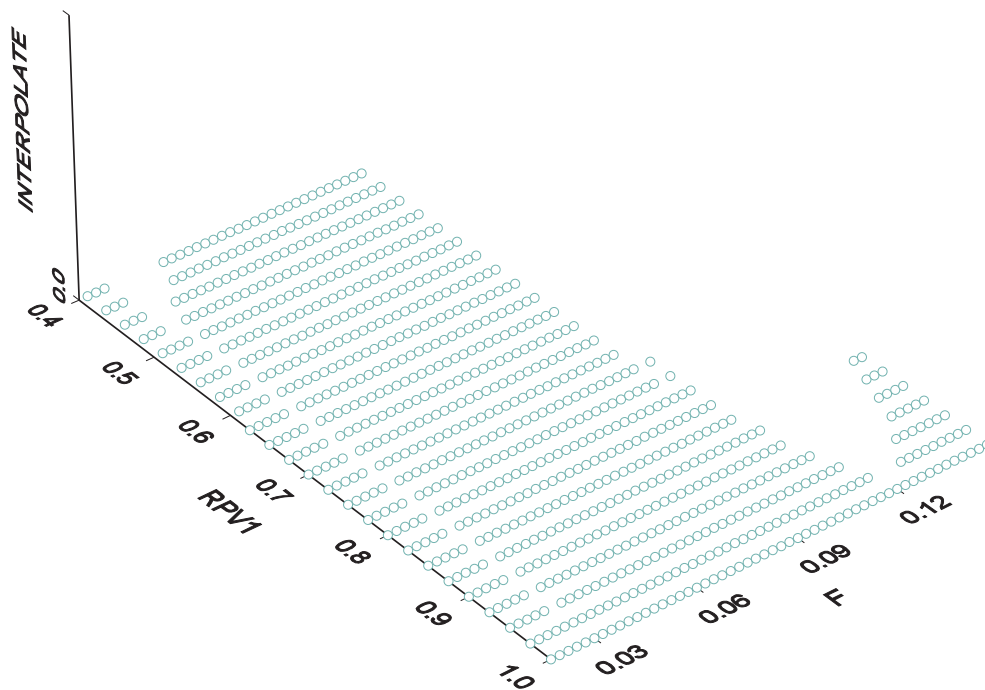

Figure 4.10: Values of the interpolation scalar, as a function of mixture fraction and RPV value for the laminar database of the Base case. Points indicate calculated than interpolated values.
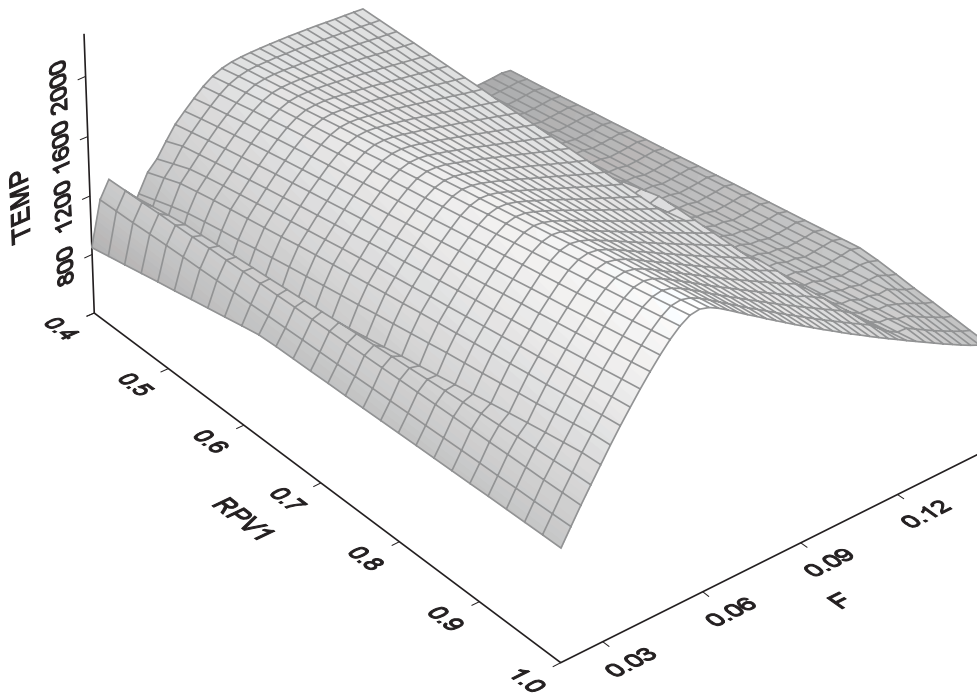
Figure 4.11: Values of temperature, in $[K]$, as a function of mixture fraction and RPV value for the laminar database of the Base case. Points indicate calculated than interpolated values.

equilibrium, i.e. smaller than 1. It can be seen that for all points obtained by calculation, the graph is linear in RPV value, for every resolved mixture fraction. This was also observed in chapter 3. In the fuel-rich region of the database that is obtained by calculation, it can be seen that the temperature goes up when moving out of equilibrium. This phenomenon is also observed by Albrecht [2] in the simulation of rich natural gas combustion for synthesis gas production. The behavior in the graph at the location of $f = 0.03$ can be explained by the convergence behavior, illustrated by the interpolation scalar and described above. At $f = 0.03$ only 2 grid points are obtained by calculation, around this value convergence goes down to values of $c = 0.5$. The consequences for the turbulent flame simulations will be negligible since the region of the solved flow field that consists of interpolated points is small and almost completely confined to the pre-flame zone.

In figure 4.12 the source term of the reaction progress variable (RPV) is plotted as a function of mixture fraction and RPV value. It can be seen that the source term does not peak around the stoichiometric mixture fraction, but shows 2 separate peaks around it instead. This is probably due to the particular CSP identifications of the reaction progress variable c. It can also be observed that in the rich region, already at values of $f \gtrsim 0.11$ the source term value is negligible. Also in the lean region the source term approaches zero inside the solution domain. This means that, at least for the heat-release rate prediction, the user-defined flammability limits (by setting a threshold temperature in the equilibrium calculation) is a correct assumption.
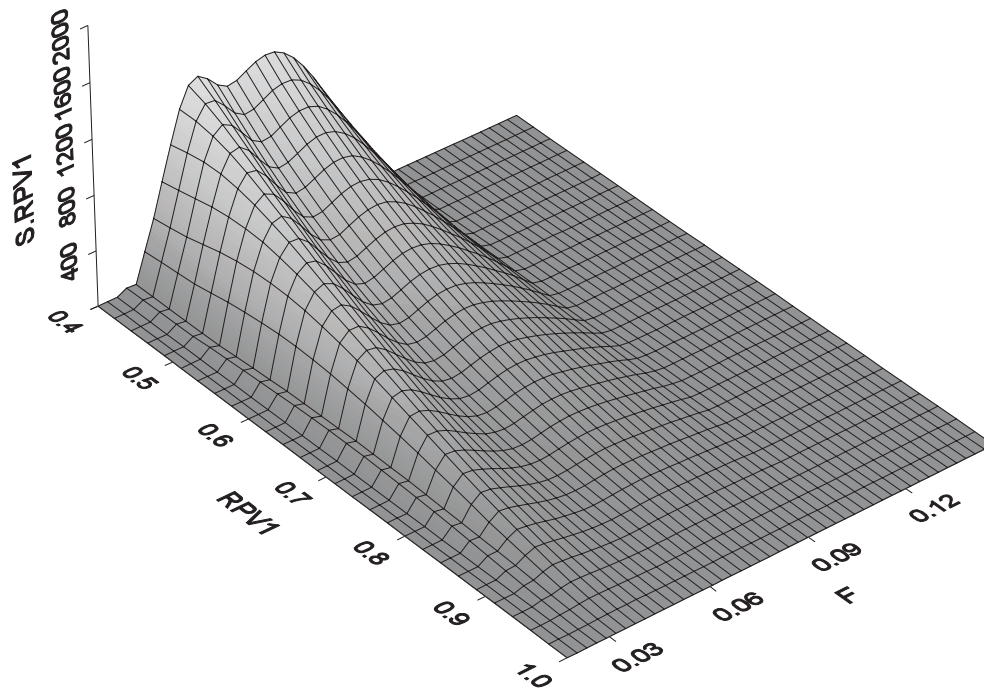
Figure 4.12: Source term of RPV 1, as a function of mixture fraction and RPV value, for the laminar database of the Base case.

4.3.3   CFD results

In figure F.1 of appendix F, temperatures and values of the presumed-PDF integrated interpolation (ITPL-) scalar are shown, for the axial plane through the mid-plane of a combustor side wall. If the ITPL value is identical 1, it means that in the averaging procedure, all integration points of the laminar database with nonzero values of the scalar PDFs have value 1 (interpolation) for the ITPL scalar. A value of zero means that only calculated (value 0) results have been used in the integration. It can be interpreted a measure of the weight factor of interpolated points in the local numerical result. Comparing in figure F.1 the ITPL scalar to the temperature plot, it can be observed that only the cold zone at the combustor entrance, in the lower part of the figure, is calculated using interpolated points. In the cold part of the fuel jet, and in intersection regions of hot and cold layers, some regions consist of values obtained partly with interpolated values. The flame zone and post-flame zone are completely consisting of calculated database points.

In figure F.2 of appendix F, another plot is given of the temperature profiles. In this plot, also velocity vectors are plotted in the axial mid-plane. From this plot it can be seen that a cold zone exists until almost the combustor exit. Thanks to the contraction, it mixes with the hot combustion gases before leaving the combustor. These jets exist thanks to the square combustor geometry and the heavy swirl that is created by the outer air inlet, it is present in all 4 corners of the combustion chamber. The maximum temperature in the domain is 2011 K, more than 250 K higher than the overall adiabatic flame temperature.

From the velocity vectors of figure F.2 it can be observed that a small outer recirculation zone exists, and a large, dominating, inner recirculation zone. Also a stagnation point exists at the back of the inner recirculation zone. The stagnation point is visible just left to the third cut-plane, seen from

the left. In test calculations with a complete circumference, i.e. without periodic boundaries, it was also present. From this figure it can also be observed that the flame ignites in the shear layers between the air jets and the fuel jet, it is stabilized through the inner recirculation zone. The inner recirculation zone exists to within the burner mouth, as can be seen from a detailed investigation of the velocity vectors.

In figure F.3 of appendix F, various quantities are plotted at the axial mid-plane of the combustor. From top to bottom these are temperature, O mass fraction, NO source term and NO mass fractions. From these graphs the origin and region of the NO production can be assessed. As in the laminar flame calculations, the O mass fraction peaks before the flame reaches its peak temperatures. It can also be seen that the O radical is produced in the shear layers between the fuel and the 2 air jets, creating two, partly overlapping, regions of high O mass fractions. In the region where both O is present and the temperature is high, the NO source term is active. It can be seen that the NO source term peaks behind the region of peak O mass fractions. The resulting NO mass fraction profile reaches its peak just behind the zone where the NO source term is most active. At that location NO buildup is highest since it has not yet diluted in the post-flame zone. At the exit of the combustor,just before the contraction, the NO concentration is reduced since there the combusted gases mix up with the fresh air jet that has surpassed the flame zone, as described above and shown in figure F.2, shown in appendix F.

The main differences in chemistry between the thermal NO mechanism employed here and the detailed NO mechanism used in the PREMIX calculations described in section 4.1, is that here the nitrogen atom has been presumed to be in steady state, and that all NO is produced by the thermal NO mechanism. Although the latter is shown to be the case too in the laminar calculations, there the NO2-NO path is active in the pre-flame zone, causing a retardation of the NO buildup in the flame. Eventually, also in the laminar calculations, most of the NO present in the domain exit originates from the thermal mechanism. From the laminar calculations it can also be seen that the N source term is very small, it is 10^6 smaller than the O source term, and still roughly 10^{-3} of the NO source term. For this reason the steady state approximation employed in the turbulent calculations can be presumed to be valid.

The main difference in the flow fields between the laminar and the turbulent case is the fact that in the latter the diffusion is much more efficient due to turbulence action. This enlarges the flame front in the turbulent simulation, as can be observed from figure F.3, depicted in appendix F. Turbulence acts to 'smear out' differences arising in the flow field. Also differential diffusion is largely compensated by turbulence action, due to the large differences in values of these two processes. This makes it difficult to extrapolate conclusions obtained from the laminar flame solution to the turbulent flow results.

4.3.4 Comparison of the turbulent flow cases

In this section the Steam case and N2 case will be compared to each other and to the Base case. The solution fields of the 3 cases are almost identical. This is logical since the burner power, inlet and overall adiabatic flame temperatures and the oxidizer inlet momentum have all been kept as constant as possible in the case study. Flow velocity profiles are almost identical for the 3 cases. Furthermore, the temperature profiles are also very similar to the base case shown in the top plot of figure F.3, and differ only in peak temperature value in the flame zone. The peak temperatures are $2012\ K$, $1894\ K$

and 1904 K for the Base case, Steam case and N2 case, respectively. Also the O mass fractions are similar for all cases to that presented in figure F.3, second from above. The peak O mass fractions are less in the Steam and N2 than in the base case, although they are lowest in the Steam case. The differences between the Steam and N2 case are due to the chemical action of H_2O, as is also the case in the laminar assessment of section 4.1. The NO source term peak values are conforming the trend in the O- and temperature values of the different cases. Production is less in the N2 case than in the Base case and even less in the Steam case. This results in the lowest peak NO mass fraction in the Steam case, followed by the N2 case while the Base case shows the highest NO peak mass fraction. In appendix F, for all cases the quantities mentioned here are shown. The reader is referred to this appendix for a detailed graphical comparison of the 3 cases.

It can be concluded that both N2 and H_2O injection reduce the emissions of NO in these turbulent flames, where the adiabatic flame temperature has been kept constant. This is achieved through reduction in peak temperatures and in O mass fractions in the flame front area by the introduction of the diluent. However, due to the chemical action of H_2O in reducing the O mass fraction, H_2O injection yields an extra reduction in NO emissions.

4.4   Comparison to measurements

In a series of measurements performed during this thesis work, the influence of steam on turbulent combustion was assessed. A test-scale gas turbine combustor was used, provided by Winnox Combustion Systems B.V. which provides a partially premixed methane-air flame. The combustor is a nozzle-mix burner similar to the DLR test combustor used in the simulations presented here. It consists of a single air swirler (versus 2 in the DLR test combustor) with fuel injection holes in the swirler vanes. Behind the swirler a contraction is fitted to enhance mixing. The combustion chamber is cylindrical in shape, with a diameter of 120 mm. The ratio of burner mouth to combustion chamber diameter is roughly identical to that in the DLR test combustor, which is 1:3. A baffle plate is inserted at the end of the combustion chamber, behind which a measurement probe is fitted. The efficient mixing that arises behind the baffle plate ensures that the measured concentrations represent the overall concentrations well. The adiabatic flame temperature is calculated from the measured burner inlet temperature and the inlet composition. A detailed discussion on the combustor and the performed measurements is given in reference [33].

The combustor is operated at atmospheric pressure, at a burner power of 20 kW, in the case discussed here. Steam is generated and injected into the air stream at a location upstream of the combustor, to ensure a good mixing. The steam to fuel ratio ω was 2.6, identical to the value used in the numerical simulations presented here. As is the case here, also in the measurements the injected steam was replaced by an equal molar volume of nitrogen, in a subsequent measurement session. A dry session was also run for comparison. In each measurement run, the air factor was changed to yield a varying adiabatic flame temperature. At each set point, the setup was given time to equilibrate. The results of the run at 20 kW at atmospheric pressure is reprinted here, in figure 4.13.

What also can be observed from this graph is that it confirms the trend observed in the turbulent flame simulations shown in this chapter, that both N2 and H_2O reduce NO emissions, but that H_2O is more effective than N2. This confirmation is even stronger when the measured exhaust NO emissions, on a g per GJ basis, are compared to the emissions from the numerical simulations. For this reason,
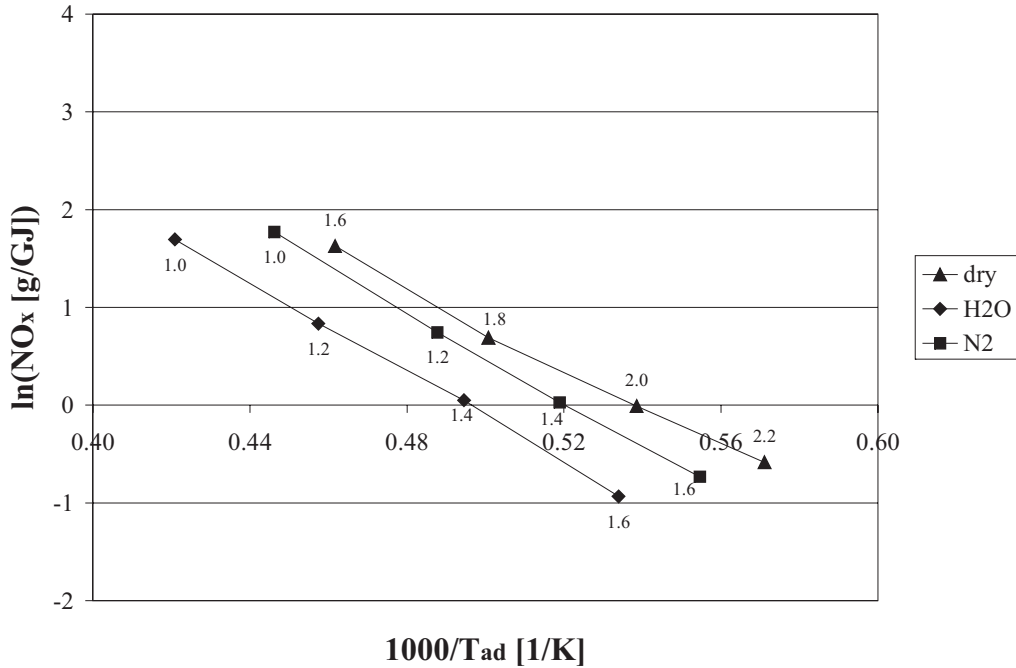
Figure 4.13: Log of NO emissions as a function of the inverse temperature, 20kW-1Bar case. Also published in [34].

the emission graphs of figure 4.13 are extrapolated to the overall adiabatic flame temperature of the numerical calculations. The data is shown in table 4.2. As can be observed from this table, the order of magnitude of the emission values also compares accurately to the values obtained by the simulations.

case	NO $g\,(GJ)^{-1}$	NO Landman $g\,(GJ)^{-1}$
Base case	0.99	0.56
Steam case	0.11	0.18
N2 case	0.30	0.33

Table 4.2: NO emissions of the different cases, comparison to measurements, ref. [34].

Although the data comparison is made between two combustors that are not identical, similarities between them can be drawn. Both are nozzle mix burners with a high degree of swirl. The flow pattern in the combustor will probably be similar, with a dominating central recirculation zone and a small outer recirculation zone. Only the residence time is very different in the 2 cases. Since the burner power of the measurements is nearly half that of the numerical simulations the residence time is roughly twice as large, at comparable combustion chamber dimensions. However, the NO mass fractions at the simulations at the centerline are constant for a large part of the domain. This is depicted in figure 4.14. Therefore, even at half the residence time, which translates to roughly halfway in the computational domain, the NO concentrations are identical to those in the combustor exhaust. This means that the NO emissions in this case are fairly independent to residence time, as
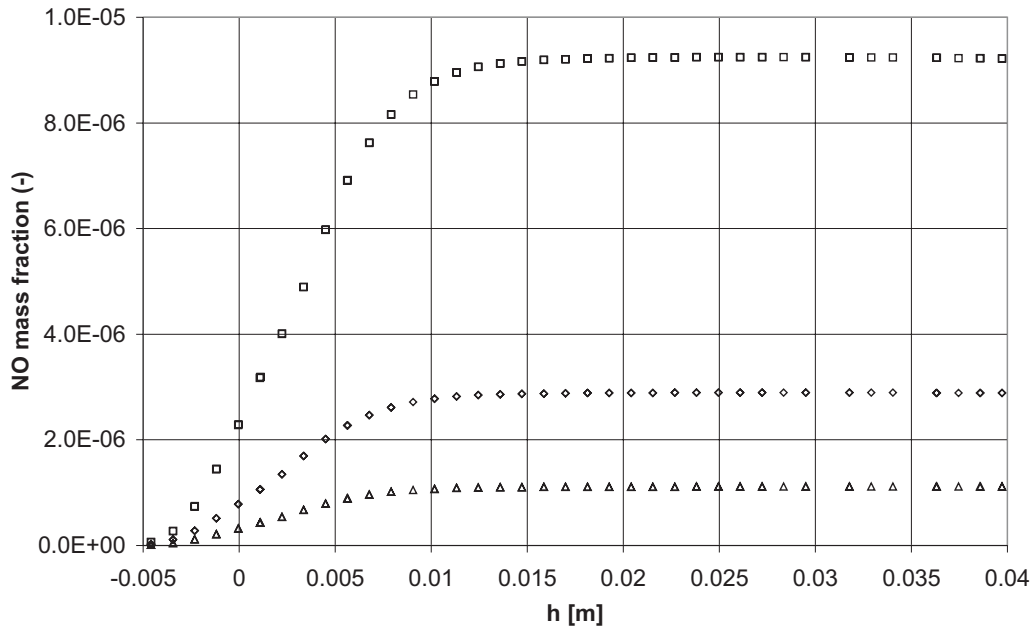
Figure 4.14: NO mass fractions at centerline, turbulent combustion simulations. Base Case: □; Steam Case: △; N2 Case: ◇.

long as they are taken in the post-flame zone. For these reasons, it is presumed reasonable to compare the NO emissions obtained by the numerical simulations in the DLR test combustor to those obtained by measurements on this combustor as described in references [33] and [34].

In the numerical calculations, it was assumed the combustion was adiabatic, i.e. without any heat loss and not taking radiation into account. In these calculations, the reducing effect of nitrogen and H_2O is apparent, although radiation differences between these species is not accounted for in these simulations. Measurements of NO emissions, presented in refs. [33] and [34], show that radiation differences are not present in the measurement results. The graphs of the logarithmic of NO emission versus the inverse temperature are straight lines. Also, the slope of the graphs is equal for all 3 cases. If radiation would have played a role, these trends would change slope for progressively lower temperatures. Also the slopes would be different for the 3 cases considered if radiation differences would have played a role. This means that the NO abatement due to differences in radiative properties of the diluents does not pose the single explanation to the differences arising in NO emissions, differences due to different chemical action of these diluents is a factor in the NO emissions of these flames.

4.5   Consequences for mixed cycle combustion chambers

The influence of steam on combustion has been assessed in the previous section. From these calculations on a scale model of a industrial gas turbine combustor, some conclusions can be drawn for mixed cycle gas turbine combustion.

As described in the previous section, the preferred injection location for steam is via the oxidizer stream. In most thermodynamic studies of the mixed cycle this is also the case. In evaporative cycles

such as the HAT water is employed in direct-contact heat exchangers where it mixes with the air stream. If in these cycles the total volume flow is kept as constant as possible under mixed combustion with respect to the design point of the burner for dry combustion, it is shown that the burner flow field is hardly affected. From the case study it is also apparent that the flame front location also hardly moves when steam is injected.

Steam injection has a positive, lowering, effect on peak temperatures, even when the overall adiabatic flame temperature is kept constant. This was noticed in diffusion flames [5] and is also shown to be the case in this partially premixed combustor. This is beneficial for the design and operation of mixed cycle combustion chambers. Since mixed cycles are often recuperated, the combustor oxidizer inlet temperature is higher than in simple cycle combustion chambers. This reduces the efficiency of using this stream as coolant. The reduction of peak flame temperatures yields a reduction in coolant flow or, adversely, allows an increase of this coolant flow in temperature. Therefore the limiting effect of the increase in oxidizer (and therefore coolant) temperature is partly compensated by the reduction in peak flame temperatures in the combustion chamber.

The exhaust temperature profiles of the Base case and the Steam case are shown in figure F.4 of appendix F. For a gas turbine design it is very important to have detailed knowledge of this temperature profile since these are used in the design of the first gas turbine stage. From this figure it can be seen that there is little difference in these profiles between the Base and the Steam case. The temperature extremes are almost identical in value, as are the locations of the hot and cold spots. This is beneficial for mixed cycle combustor design. It means that, given a constant volume flow in the dry and the steam case, the temperature profile might not be significantly dependent of steam injection. Given the fact that the flow patterns in the entire combustion chamber are almost identical, it can be assumed that this is also the case if the exhaust location is shifted.

Steam has a lowering effect on NO emissions. This can be employed in 2 different ways. It can be used to improve cycle efficiency and/or specific work output of the cycle while maintaining a constant NO emission level. Alternatively, steam can be employed as a means of reducing emissions in novel designs. Both alternatives will in any case result in a higher cycle efficiency of the mixed cycle than the simple cycle, as described in chapter 1.

Concluding, from a perspective of burner and combustor design, the design of mixed cycles should aim at creating a cycle with a comparable total steam plus air volume flow to the air flow of an existing dry system. The overall adiabatic flame temperature should also be kept as constant as possible. This ensures that the burner flow field of the mixed flow cycle is changed the least from the dry cycle. This may still require a redesign of some key parts such as the turbine, but that is always simpler and cheaper than creating a completely new gas turbine cycle. It also allows a knowledge transfer from a known gas turbine cycle to the new, mixed cycle.

Chapter 5

Conclusions and recommendations

Turbulent measurements and simulations were performed on the influence of steam on combustion. This work shows that steam injection is beneficial for the emissions of NO in a partially premixed turbulent methane-air flame. Steam reduces the emissions more effective than nitrogen dilution, probably because of the chemical action of H_2O on the O radical. Also, steam injection reduces peak temperatures. This can partly compensate for the higher combustor inlet temperatures of the oxidizer which makes it less suited as a coolant medium for the combustor liner. If the total oxidizer volume flow is kept constant, the combustor flow field is not affected by the injection of steam. This is also the case for the exhaust temperature profiles. These 2 factors are beneficial for the design and operation of mixed cycle gas turbine combustion chambers. It allows a redesign of an existing gas turbine, rather than necessitating a design for a completely novel gas turbine.

In order to investigate in detail the processes leading to NO emission in steam injected flames, a novel combustion model is developed that allows the numerical simulation of combustion of adiabatic or nonadiabatic flames which can be premixed, partially premixed or nonpremixed. The model is designed for the Favre averaged framework although it may also be employed in Large Eddy- or Direct Numerical simulations. Progress of reaction, mixing and heat loss are incorporated through the use of dimensionless scalars c, f and i, respectively, hence the model acronym CFI. It uses a separate preprocessing code to calculate and subsequently average the source terms of the scalar transport equations. CSP is employed to map a detailed chemical reaction mechanism onto the dimensionless scalars using element conservation- and steady state relations. CSP both determines the optimal choice of steady-state relations as well as the optimal mapping of the reduced mechanism onto the scalars that account for combustion. Further, a novel algorithm is presented for the storage and retrieval of data based on the piecewise linear interpolation algorithm.

The performance of the model was assessed using numerical calculations of laminar, 1-dimensional, premixed, freely propagating methane-air flames using a detailed chemical reaction mechanism. By mapping the flame solution onto the reaction scalars c and subsequently compare the results of the detailed reaction mechanism with values obtained from laminar databases, both solutions can be compared. The comparison is better for a 2-step than for a 1-step reduced mechanism, and better for CSP-determined reduced mechanism mapping than for manually determined reduced mechanism mapping. The comparison is also better for a stoichiometric flame than for a lean flame. However, the differences between the 1-step and the 2-step mechanisms are too little to necessitate the use of a 2-step reduced mechanism in flame simulations. Also the memory requirements and computational

time for the 2-step mechanisms is significantly higher, for little improved performance. For these reasons, further flame simulations were done using a 1-step mechanism, with CSP-defined reduced mechanism mapping. The steady-state assumption of NO is so poor in these 1- and 2-step mechanisms that it was chosen to use a separate transport equation accounting for the NO produced via the Zeldovich mechanism in subsequent turbulent flame simulations.

A laminar assessment was performed, using detailed laminar, 1-dimensional, premixed, freely propagating flame simulations, on the influence of steam on the flame. Three cases were studied, a Base case consisting of a methane-air flame with no dilution. Subsequently a case was set up with steam dilution, the Steam case, and with nitrogen dilution, the N2 case. The overall adiabatic flame temperature was kept constant, as well as the inlet temperature to eliminate the effect of temperature on NO emissions. The fuel mass fraction was modified in the steam- and in the nitrogen case to maintain a constant overall adiabatic flame temperature for all cases. It was concluded that in all cases the thermal NO mechanism was responsible for the bulk of the NO production. Furthermore, the N2 case had the highest emissions of NO, followed by the Base case and the Steam case, subsequently. The differences originate in the peak values of the N and O mass fractions. Where both radicals are present in large mass fractions at high temperatures, the NO source term is large. In the N2 Case, this is the case, resulting in the highest peak NO source term value. In the Steam case, the O radical mass fraction is suppressed due to the chemical action of H_2O. In the Base case, N is lower. The origin of the differences lies in a very delicate system, where interspecies diffusion plays a major role.

A numerical assessment was performed on the influence of steam on turbulent combustion. For this purpose, a scale model of an industrial gas-turbine combustor was used which is created by DLR (Deutsches Zentrum fr Luft und Raumfahrt). As a basis for the simulations a set point has been chosen which measurements showed to burn very stable. From this set point, the initial temperature is raised to ensure that injected H_2O with the oxidizer is present in the form of steam. Subsequently, the same 3 cases as used for the laminar assessment were solved, this time in the turbulent combustor. Diluents were injected perfectly premixed with the oxidizer stream. The burner power was adjusted to maintain an identical overall adiabatic flame temperature for all 3 cases, identical to the flame temperature of the laminar assessment. By also keeping the volume flow through the oxidizer inlet constant for all cases, the burner flow field was identical for the 3 cases considered. In contrast to the laminar flame simulations, the turbulent simulations showed that both N2 and H_2O reduce NO emissions, although steam yields the highest reduction with respect to the Base case. Diluents reduced the peak temperatures and O peak mass fractions, reducing the production of NO through the thermal mechanism. A main difference between the turbulent and the laminar simulations is the more effective turbulent diffusion present in the former. This smooths differences arising in the flame, also acting to thicken the flame front. Differential diffusion is also largely compensated by turbulence action, due to the large differences in magnitude of these processes. These results illustrate illustrate very clearly that results and trends, obtained by laminar simulations, cannot always be directly translated to a similar turbulent situation.

Measurements were performed on a turbulent, partially premixed model gas turbine combustor. Steam was injected at an equal steam-to-fuel ratio as in the simulations. in a subsequent run, an equal volumetric flow of nitrogen replaced the steam flow. A dry run was also made. Steam and nitrogen both reduce NO emissions, although steam yields a larger reduction, on a g per GJ basis, than nitrogen. Arrhenius plots of the logarithmic of NO versus the inverse temperature showed a linear trend for each separate case. The slope of the cases was nearly identical and constant over the

measured domain. This indicates that radiation is not a major factor in differences between the results. If this were the case, the slope would be a function of temperature and the slopes would be different for the cases considered.

Regarding the combustion model, a few recommendations can be made. First of all, as was also shown in the results in this thesis, the solution procedure would benefit from an improved initial guess. At the moment this is simply the previous solution of a certain loop, but a solution might be at hand which with scalar values closer to those set for the calculation to be attempted. This might improve the range of convergence of the laminar database. Also, the solution path could be improved, by creating a path that more smoothly takes the solution further away from chemical equilibrium. Rather than scalar for scalar, a multidimensional loop might be created that moves all scalars from equilibrium more simultaneously.

Unfortunately, it was not feasible to perform a turbulent validation of the CFI combustion model. Differences were observed between calculations and measurements of the cold flow. Unfortunately, time lacked to resolve this problem. For this reason this work was not completed. However, it is recognized that this constitutes a gap in the work presented here and it is strongly recommended to complete this validation work in the near future.

The influence of radiation on combustion was not assessed here. However, in the laminar database program the enthalpy scalar that can incorporate for these effects is already implemented. It needs implementation in the turbulent database program, where some source terms need to be added, as well as in the interface between the flow solver and the turbulent thermochemical database. Also a transport equation needs to be created that accounts for this scalar. It is very interesting to investigate the effects and role of radiation on the cases presented here.

Appendix A

Nomenclature

Symbol	Description	Dimension
A_i	Species i	
$[A_i]$	concentration of species i	$mol\,cm^{-1}$
$\boldsymbol{a}$	matrix of right eigenvectors	
$\boldsymbol{B}$	database array	
$\boldsymbol{b}$	matrix of left eigenvectors	
$\boldsymbol{C}$	hypercube grid point value matrix	
c_k	reaction progress variable	
$c_{p,i}$	specific heat of species i at constant pressure	$J\,kg^{-1}\,K^{-1}$
$\boldsymbol{D}$	coordinate distance pointer vector	
D_i	local CSP-pointer	
D_{ij}	binary diffusion coefficient	
D_i^T	thermal diffusion coefficient	
$\boldsymbol{Dx}$	coordinate distance vector	
E	number of elements	
e	internal energy	$kJ\,kg^{-1}$
F	function	
f	mixture fraction	
h	enthalpy	$J\,kg^{-1}$
$\boldsymbol{I}$	unit tensor	
I_i	integrated CSP-pointer	
i	enthalpy scalar	
K	total database point number	
k	turbulence kinetic energy	$m^s\,s^{-2}$
Le	Lewis number	
M	molar mass	$kg\,kmol^{-1}$
M	number of steady-state species	
N	number	
$\boldsymbol{P}$	stress tensor	Pa
$\boldsymbol{P}$	pointers matrix	

Symbol	Description	Dimension
P	probability density function	
p	hydrostatic pressure	
$\boldsymbol{Q}$	point number vector	
$\boldsymbol{q}$	heat flux vector	$W\,m^{-3}$
R	Number of reactions	
R_g	gas constant	$m^2\,s^{-2}\,K^{-1}$
Re	Reynolds number	
S	number of steps	
Sc	Schmidt number	
T	temperature	K
t	time	s
T_{ad}	adiabatic flame temperature	K
$\boldsymbol{u}$	velocity vector	$m\,s^{-1}$
V	normalization function for the enthalpy scalar	
$\boldsymbol{V}_i$	diffusion velocity vector	$m\,s^{-1}$
W_i	normalization function for the reaction progress variable	
$\boldsymbol{X}$	mole fraction vector	
$\boldsymbol{x}$	coordinate	m
$\boldsymbol{x}^p$	interpolation point	m
$\boldsymbol{Y}$	species vector	
Greek	**Description**	**dimension**
$\triangle$	finite difference	
ε	turbulence eddy dissipation	$m^s\,s^{-3}$
$\boldsymbol{\eta}$	CSP-vector	
κ	bulk viscosity	$Pa\,s$
λ	heat conductivity	$W\,m\,K^{-1}$
μ	molecular viscosity	$Pa\,s$
ν'_{ij}	stoichiometric coefficient of forward reaction	
ν''_{ij}	stoichiometric coefficient of backward reaction	
ω	rate of change	$kg\,m^{-1}\,s^{-1}$
ρ	density	$kg\,m^{-3}$
χ	grid point division vector	
Superscripts	**Description**	
$\overline{}$	(Reynolds) mean	
$'$	Reynolds fluctuation	
$\sim$	Favre mean	
$''$	Favre fluctuation	
T	transpose	
$\widehat{}$	molar dimension	
c	conservation	
r	rapid	
s	slow	

Appendix B

Derivation of the CFI transport equations

In this appendix a detailed derivation is given of the enthalpy and RPV transport equations of the CFI combustion model.

B.1   Transport equation for a RPV

Given the vectors $\boldsymbol{\eta}^s$ and their normalization to reaction progress variables according to definition (2.81), the following transport equation for a reaction progress variable c can be obtained by inserting (2.81) into the species transport equation (2.22):

$$
\underbrace{\frac{\partial}{\partial t}\left(cW(f,i)+\eta^{s,u}(f)\right)}_{1}+\underbrace{\rho\boldsymbol{u}\nabla\left(cW(f,i)+\eta^{s,u}(f)\right)}_{2}=
$$
$$
\underbrace{\nabla.\left\{\rho D\nabla\left[cW(f,i)+\eta^{s,u}(f)\right]\right\}}_{3}+\omega^c \tag{B.1}
$$

where $\omega^c = \boldsymbol{b}_k^s \cdot \boldsymbol{\omega}$ and the subscript k for the kth RPV is dropped. This expression will be rewritten term by term, in the following sections. For convenience subscripts will denote partial derivation towards that variable.

Term 1

$$
\frac{\partial}{\partial t}\left(cW(f,i)+\eta^{s,u}(f)\right)=W\frac{\partial\rho c}{\partial t}+\eta^{s,u}\frac{\partial\rho}{\partial t}+\rho cW_f\frac{\partial f}{\partial t}+\rho cW_i\frac{\partial i}{\partial t}+\rho\eta_f^{s,u}\frac{\partial f}{\partial t} \tag{B.2}
$$

using the rule $\frac{\partial W(f,i)}{\partial t}=\frac{\partial W}{\partial f}\frac{\partial f}{\partial t}+\frac{\partial W}{\partial i}\frac{\partial i}{\partial t}$.

Term 2

$$
\begin{aligned}
\rho\boldsymbol{u}\nabla\left(cW(f,i)+\eta^{s,u}(f)\right) &= W\nabla\left(\rho\boldsymbol{u}c\right)+\rho\boldsymbol{u}cW_f\nabla f+\rho\boldsymbol{u}cW_i\nabla i\\
&+ \eta^{s,u}\nabla\left(\rho\boldsymbol{u}\right)+\rho\boldsymbol{u}\eta_f^{s,u}\nabla f+\rho\boldsymbol{u}\eta_i^{s,u}\nabla i
\end{aligned} \tag{B.3}
$$

91

Term 3

Term 3 is somewhat more cumbersome since it involves second derivatives.

$$\nabla.\left\{\rho D\nabla\left[cW(f,i)+\eta^{s,u}(f)\right]\right\} \;=\; \underbrace{\nabla.\left(\rho Dc\nabla W\right)}_{3A}+\underbrace{\nabla.\left(\rho DW\nabla c\right)}_{3B}$$
$$+\;\; \underbrace{\nabla.\left(\rho D\nabla\eta^{s,u}\right)}_{3C} \tag{B.4}$$

Term 3A:

$$
\begin{aligned}
\nabla.\left(\rho Dc\nabla W\right)=\ldots \;=&\; \rho Dc\left(\nabla f\right)^2 W_{ff}+\rho Dc\nabla f\nabla iW_{fi}\\
+&\; W_f c\nabla\left(\rho D\nabla f\right)+W_f\rho D\nabla f\nabla c\\
+&\; \rho Dc\left(\nabla i\right)^2 W_{ii}+\rho Dc\nabla i\nabla fW_{if}\\
+&\; cW_i\nabla\left(\rho D\nabla i\right)+W_i\rho D\nabla i\nabla c
\end{aligned} \tag{B.5}
$$

Term 3B:

$$\nabla.\left(\rho DW\nabla c\right)=\ldots=\rho D\nabla c\nabla fW_f+\rho D\nabla c\nabla iW_i+W\rho D\nabla.\left(\rho D\nabla c\right) \tag{B.6}$$

Term 3C:

$$\nabla.\left(\rho D\nabla\eta^{s,u}\right)=\ldots=\eta_f^{s,u}\nabla.\left(\rho D\nabla f\right)+\rho D\left(\nabla f\right)^2\eta_{ff}^{s,u} \tag{B.7}$$

Resulting expression

This results in the following expression:

$$
\begin{aligned}
&\eta^{s,u}\left(\frac{\partial\rho}{\partial t}+\nabla\left(\rho\boldsymbol{u}\right)\right)\\
+&\;\left(cW_f+\eta_f^{s,u}\right)\left\{\rho\frac{\partial f}{\partial t}+\rho\boldsymbol{u}\nabla f-\nabla.\left(\rho D\nabla f\right)\right\}\\
+&\;cW_i\left\{\rho\frac{\partial i}{\partial t}+\rho\boldsymbol{u}\nabla i-\nabla.\left(\rho D\nabla i\right)\right\}\\
+&\;W\left\{\frac{\partial\rho c}{\partial t}+\nabla\left(\rho\boldsymbol{u}c\right)-\nabla.\left(\rho D\nabla c\right)\right\}\\
=&\;\rho Dc\left(\nabla f\right)^2 W_{ff}+\rho Dc\nabla f\nabla iW_{fi}+\rho D\nabla f\nabla cW_f+\rho Dc\left(\nabla i\right)^2 W_{ii}\\
+&\;\rho Dc\nabla i\nabla fW_{if}+2W_i\rho D\nabla i\nabla c+\rho D\nabla c\nabla fW_f+\rho D\left(\nabla f\right)^2\eta_{ff}^{s,u}+\omega^c
\end{aligned} \tag{B.8}
$$

In this expression, the term behind $\eta^{s,u}$ is the mass conservation equation and is therefore equal to zero. The terms in brackets behind cW_f and behind $\eta_f^{s,u}$ vanish since they comprise the conservation equation for the mixture fraction scalar. The term behind cW_i is equal to the source term of the enthalpy scalar, i, which will be discussed in section B.2.

Since $\boldsymbol{Y}$ and hence $\boldsymbol{\eta}^s$ are linear in f, $Y_{ff}^u = 0$, and the second last term on the right hand side disappears (In a premixed problem, consisting of only 1 inlet, all terms containing derivatives to f disappear). The laminar mass fraction equation of a RPV is therefore:

$$
\begin{aligned}
&\frac{\partial \rho c}{\partial t} + \nabla \left(\rho \boldsymbol{u} c \right) - \nabla . \left(\rho D \nabla c \right) \\
&= -c \frac{W_i}{W} S^i + \rho D c \left(\nabla f \right)^2 \frac{W_{ff}}{W} + \rho D c \nabla f \nabla i \frac{W_{fi}}{W} + \rho D \nabla f \nabla c \frac{W_f}{W} + \rho D c \left(\nabla i \right)^2 \frac{W_{ii}}{W} \\
&+ \ \rho D c \nabla i \nabla f \frac{W_{if}}{W} + 2 \frac{W_i}{W} \rho D \nabla i \nabla c + \rho D \nabla c \nabla f \frac{W_f}{W} + S^c
\end{aligned} \tag{B.9}
$$

Here, the source term of the transport equation for i is included. This term contains all but the convection-diffusion and time derivative terms of the i-transport equation (see the following section for a derivation). Furthermore, $S^c = \frac{\omega^c}{W}$.

B.2 Transport equation for the enthalpy scalar

The laminar static enthalpy equation is given in expression (2.23), and repeated here:

$$
\frac{\partial \rho h}{\partial t} + \nabla . \left(\rho \boldsymbol{u} h \right) - \nabla . \left(\rho D_{im} \nabla h \right) = q^{rad} \tag{B.10}
$$

A enthalpy scalar i is defined according to definition 2.86. Inserting this expression into expression (2.23) and rearranging the terms, in a manner analogous to what is done in rewriting the RPV transport equation in the previos section, yields the following transport equation for the enthalpy scalar i:

$$
\frac{\partial \rho i}{\partial t} + \nabla . \left(\rho \boldsymbol{u} i \right) - \nabla . \left(\rho D \nabla i \right) = \rho D \left(\nabla f \right)^2 \frac{V_{ff}}{V} \left(i - 1 \right) + 2 \rho D \nabla i \nabla f \frac{V_f}{V} - S^{\mathrm{rad}, i} \tag{B.11}
$$

Here the fact that $h_{ff}^{ad} = 0$ is used. Since the adiabatic enthalpy is almost a linear function in mixture fraction, the second derivative towards f can be ignored.

B.3 Favre-averaging the transport equations

B.3.1 Mean of c

The laminar equation is given in expression (B.9)):

$$
\begin{aligned}
&\frac{\partial \rho c}{\partial t} + \nabla \left(\rho \boldsymbol{u} c \right) - \nabla . \left(\rho D \nabla c \right) \\
&= -c \frac{W_i}{W} S^i + \rho D c \left(\nabla f \right)^2 \frac{W_{ff}}{W} + \rho D c \nabla f \nabla i \frac{W_{fi}}{W} + \rho D \nabla f \nabla c \frac{W_f}{W} + \rho D c \left(\nabla i \right)^2 \frac{W_{ii}}{W} \\
&+ \ \rho D c \nabla i \nabla f \frac{W_{if}}{W} + 2 \frac{W_i}{W} \rho D \nabla i \nabla c + \rho D \nabla c \nabla f \frac{W_f}{W} + S^c
\end{aligned}
$$

The CFI-scalars and velocities are decomposed into a Favre mean and fluctuating part. Subsequently the equation is averaged where the rules apply that $\overline{\rho \phi''} \equiv 0$, $\overline{\widetilde{\phi}} = \widetilde{\phi}$ and $\overline{\rho \phi''^2} = \overline{\rho} \widetilde{\phi''^2}$. After rewriting the scalars and applying these rules, the remaining equation reads:

$$
\nabla.\left(\overline{\rho}\widetilde{\boldsymbol{u}}\widetilde{c}\right) - \nabla.\left(\overline{\rho}D\nabla\widetilde{c}\right) + \underbrace{\nabla.\overline{\rho\boldsymbol{u}"c"}}_{1} = \underbrace{\overline{\rho}\widetilde{c}\left(\nabla\widetilde{f}\right)^{2}\overline{D\left(\dfrac{W_{ff}}{W}\right)}}_{2}
$$

$$
+ \quad \underbrace{\overline{\widetilde{c}\left(\dfrac{W_{ff}}{W}\right)\rho D\nabla f"\nabla f"}}_{3} + \underbrace{2\nabla\widetilde{f}\overline{\left(\dfrac{W_{ff}}{W}\right)\rho Dc"\nabla f"}}_{4}
$$

$$
+ \quad \underbrace{2\overline{\rho}\widetilde{c}\nabla\widetilde{f}\nabla\widetilde{i}\overline{D\left(\dfrac{W_{fi}}{W}\right)}}_{5} + \underbrace{2\nabla\widetilde{i}\overline{\left(\dfrac{W_{fi}}{W}\right)\rho Dc"\nabla f"}}_{6}
$$

$$
+ \quad \underbrace{\overline{2\rho D\left(\dfrac{W_{f}}{W}\right)\nabla\widetilde{f}\nabla\widetilde{c}}}_{7} + \underbrace{\overline{2\left(\dfrac{W_{f}}{W}\right)\rho D\nabla f"\nabla c"}}_{8} + \underbrace{\widetilde{c}\rho D\overline{\left(\dfrac{W_{ii}}{W}\right)}\left(\nabla\widetilde{i}\right)^{2}}_{9}
$$

$$
+ \quad \underbrace{\rho D\overline{\left(\dfrac{W_{i}}{W}\right)}\nabla\widetilde{i}\nabla\widetilde{c}}_{10} + \underbrace{\overline{S^{c}}}_{11} - \underbrace{\overline{\left(\dfrac{W_{i}}{W}\right)\widetilde{c}\widetilde{S}^{i}}}_{12} - \underbrace{\overline{\left(\dfrac{W_{i}}{W}\right)c"S^{i"}}}_{13} \tag{B.12}
$$

This is the exact, rewritten equation. In this expression several terms can be ignored. Terms 4, 6 and 8 are zero because of the independence of the scalars. Terms 2, 5, 7, 9 and 10 are assumed to have negligible contribution [59]. This leaves the modeling of terms 1, 3, 12 and 13. Furthermore, fluctuations of W and its derivatives will be neglected.

Term 1 is modeled using a gradient assumption:

$$
\nabla.\overline{\rho\boldsymbol{u}"c"} = -\nabla.\left(\dfrac{\mu_{T}}{\mathrm{Sc}_{T}}\nabla\widetilde{c}\right) \tag{B.13}
$$

where Sc_{T} is a turbulent Schmidt number.

Term 3 is modeled as follows:

$$
\overline{\widetilde{c}\left(\dfrac{W_{ff}}{W}\right)\rho D_{im}\nabla f"\nabla f"} = \widetilde{c}\left(\dfrac{W_{ff}}{W}\right)\overline{\rho D_{im}\nabla f"\nabla f"} = \dfrac{1}{2}\overline{\rho}\widetilde{c}\widetilde{\left(\dfrac{W_{ff}}{W}\right)}R_{T}\dfrac{\varepsilon}{k}\overline{f"^{2}} \tag{B.14}
$$

In this expression, $\overline{f"^{2}} \equiv g$ for which a transport equation is solved. Here R_{T} is set to 2.

Term 12 yields in combination with term 13:

$$
\overline{\left(\dfrac{W_{i}}{W}\right)}\left(\overline{c"S^{i"}} + \widetilde{c}\widetilde{S}^{i}\right) = \overline{\left(\dfrac{W_{i}}{W}\right)}\overline{cS^{i}} \tag{B.15}
$$

Term $\overline{cS^{i}}$ can be rewritten further. Rewriting the i-scalar source term yields:

$$
\overline{cS^{i}} = \overline{\rho Dc\left(\nabla f\right)^{2}\dfrac{V_{ff}}{V}\left(i-1\right)} + \overline{2c\rho D\nabla i\nabla f\dfrac{V_{f}}{V}} - \overline{cS^{\mathrm{rad},i}} \tag{B.16}
$$

Taking into consideration the statements above regarding ignoring terms with averaged scalars containing D and removing statistical independent terms, this yields:

$$\overline{cS^i} = \overline{\rho} \widetilde{c} \overline{\left(\frac{V_{ff}}{V}\right)} \left(\widetilde{i} - 1\right) R_T \frac{\varepsilon}{k} g - \overline{cS^{\mathrm{rad},i}} \tag{B.17}$$

This yields the following expression for the mean of a reaction progress variable c:

$$\nabla. \left(\overline{\rho}\widetilde{u}\widetilde{c}\right) - \nabla. \left(\overline{\rho} D_T \nabla \widetilde{c}\right) = \overline{S^c} + \overline{\left(\frac{W_i}{W}\right)} \overline{cS^{\mathrm{rad},i}}$$
$$+ \ \left(\overline{\left(\frac{W_{ff}}{W}\right)} + \left(1 - \widetilde{i}\right)\overline{\left(\frac{W_i}{W}\right)} \cdot \overline{\left(\frac{V_{ff}}{V}\right)}\right)\overline{\rho}\widetilde{c}\frac{\varepsilon}{k}g \tag{B.18}$$

where $D_T = D + \frac{\mu_T}{\mathrm{Sc}_T}$

B.3.2 Mean of i

The laminar transport equation equation reads (See expression (B.11) on page 93):

$$\frac{\partial \rho i}{\partial t} + \nabla\left(\rho \boldsymbol{u} i\right) - \nabla.\left(\rho D \nabla i\right) = \rho D\left(\nabla f\right)^2 \frac{V_{ff}}{V}\left(i - 1\right) + 2\rho D\nabla i\nabla f\frac{V_f}{V} - S^{\mathrm{rad},i}$$

Here it will be assumed that fluctuations of V and its derivatives are negligible and that only its mean Favre-averaged quantities remain. After averaging and removing the terms that are per definition zero the following expression arises:

$$\nabla.\left(\overline{\rho}\widetilde{u}\widetilde{i}\right) + \underbrace{\nabla.\left(\overline{\rho u'' i''}\right)}_{1} - \nabla.\left(\overline{\rho} D\nabla\widetilde{i}\right) = \underbrace{\rho D\overline{\left(\frac{V_{ff}}{V}\right)}\left(\nabla\widetilde{f}\right)^2\left(\widetilde{i} - 1\right)}_{2}$$

$$+ \ \underbrace{2\nabla\widetilde{f}\overline{\left(\frac{V_{ff}}{V}\right)\rho D\nabla f'' i''}}_{3} + \underbrace{\left(\widetilde{i} - 1\right)\overline{\rho D\nabla f'' \nabla f''\left(\frac{V_{ff}}{V}\right)}}_{4}$$

$$+ \ \underbrace{\overline{\left(\frac{V_{ff}}{V}\right)\rho D\nabla f''\nabla f'' i''}}_{5} + \underbrace{2\rho D\overline{\left(\frac{V_f}{V}\right)}\nabla\widetilde{i}\nabla\widetilde{f}}_{6} + \underbrace{2\rho D\overline{\left(\frac{V_f}{V}\right)\nabla i''\nabla f''}}_{7} - \overline{S^{\mathrm{rad},i}} \tag{B.19}$$

In this expression, terms 3, 5 and 7 are zero because of the assumed linear independence of the scalars. Terms 2 and 6 will be neglected since they contain the laminar diffusion coefficient D_{im} which is typically in the order of 10^{-5}, it is assumed that hence these terms have negligible contribution. Term 1 is modeled using a gradient assumption analogous to term 1 in expression (B.13); the Reynolds averaged expression in term 4 is modelled as in expression (B.14) on page 94. This yields the following expression for the favre average of i:

$$\nabla.\left(\overline{\rho}\widetilde{u}\widetilde{i}\right) - \nabla.\left(\overline{\rho} D_T\nabla\widetilde{i}\right) = \overline{\rho}\left(\widetilde{i} - 1\right)\overline{\left(\frac{V_{ff}}{V}\right)}\frac{\varepsilon}{k}g - \overline{S^{\mathrm{rad},i}} \tag{B.20}$$

B.3.3   Variance of c

The variance equation is obtained by multiplying expression (B.9) on page 93 with $c"$ and subsequently apply the averaging operation:

$$
\begin{aligned}
&\overline{c" \nabla(\rho \boldsymbol{u} c)} - \overline{c" \nabla.(\rho D \nabla c)} \\
=\ & \overline{c" \rho D c (\nabla f) \frac{W_{ff}}{W}} + \overline{c" \rho D c \nabla f \nabla i \frac{W_{fi}}{W}} + \overline{c" \rho D \nabla f \nabla c \frac{W_f}{W}} + \overline{c" \rho D c (\nabla i)^2 \frac{W_{ii}}{W}} \\
+\ & \overline{c" \rho D c \nabla i \nabla f \frac{W_{if}}{W}} + \overline{2 c" \frac{W_i}{W} \rho D_{im} \nabla i \nabla c} + \overline{c" \rho D \nabla c \nabla f \frac{W_f}{W}} + \overline{c" S^c} - \overline{c" c \frac{W_i}{W} S^i} \quad \text{(B.21)}
\end{aligned}
$$

In the averaging operation, averages of fluctuations of products of different scalars, such as $\overline{f" c"}$, $\overline{c" i"}$ etc., disappear because of the independence of the scalars. Also fluctuations of W and its derivatives will be assumed to be negligible. This leads to the following expression:

$$
\begin{aligned}
& \frac{1}{2} \nabla \overline{\rho} \widetilde{\boldsymbol{u}} \widetilde{c"^2} + \underbrace{\widetilde{\boldsymbol{u}" c"}}_{1} \nabla \widetilde{c} + \frac{1}{2} \underbrace{\nabla \widetilde{\boldsymbol{u}" c"^2}}_{2} - \underbrace{\overline{c" \nabla.(\rho D \nabla \widetilde{c})}}_{3} - \underbrace{\frac{1}{2} \nabla.\left(\overline{\rho D \nabla c"^2}\right)}_{4} \\
+\ & \underbrace{\overline{\nabla.(\rho D \nabla c" \nabla c")}}_{5} = -\widetilde{c"^2} \frac{\overline{W_i}}{W} \overline{S^i} + \underbrace{\overline{\rho D \frac{W_{ff}}{W} c"^2 \nabla f" \nabla f"}}_{6} \\
+\ & \frac{1}{2} \underbrace{\overline{\rho D \frac{W_f}{W} \nabla c"^2} \nabla \widetilde{f}}_{7} + \frac{\overline{W_{ii}}}{W} \left(\underbrace{\overline{\rho D c"^2}}_{8} \left(\nabla \widetilde{i}\right)^2 + \underbrace{\overline{\rho D c"^2 \nabla i" \nabla i"}}_{9} \right) \\
+\ & \underbrace{\overline{\rho D \frac{W_{if}}{W} c"^2} \nabla \widetilde{i} \nabla \widetilde{f}}_{10} + \underbrace{\overline{\rho D \frac{W_i}{W} \nabla c"^2} \nabla \widetilde{i}}_{11} + \frac{1}{2} \underbrace{\overline{\rho D \frac{W_f}{W} \nabla c"^2} \nabla \widetilde{f}}_{12} \\
+\ & \overline{c S^c} - \widetilde{c} \widetilde{S^c} \quad \text{(B.22)}
\end{aligned}
$$

This expression contains several unclosed terms, underbraced 1 through 12. Terms 3, 4, 7, 8, 10, 11 and 12 are nonzero but are expected to be small in high-Reynolds number flows [59] and are therefore neglected. Term 9 is zero since fluctuations of the i-scalar are ignored. Term 1 is modelled using a gradient assumption [59]:

$$
\overline{\rho \boldsymbol{u}" c"} = -\frac{\mu_T}{\mathrm{Sc}_T} \nabla \widetilde{c} \quad \text{(B.23)}
$$

Term 5 is modeled as follows, see expression (B.14) in section B.3.1:

$$
\overline{\nabla.(\rho D \nabla c" \nabla c")} = \frac{1}{2} R_T \overline{\rho} \frac{\varepsilon}{k} \widetilde{c"^2} \quad \text{(B.24)}
$$

Term 6 is split up and modeled as:

$$
\overline{\rho D c"^2 \nabla f" \nabla f"} = \widetilde{c"^2} \cdot \overline{\rho D \nabla f" \nabla f"} = \widetilde{c"^2} \cdot \frac{1}{2} R_T \overline{\rho} \frac{\varepsilon}{k} \widetilde{f"^2} \quad \text{(B.25)}
$$

This leads to the following equation for $\widetilde{c''^2}$, after multiplying the expression with 2, inserting $R_T = 2$ and rearranging of the terms:

$$\nabla. \left(\overline{\rho} \widetilde{u} \widetilde{c''^2} \right) - \nabla. \left(D_T \nabla \widetilde{c''^2} \right)$$

$$= 2 \frac{\mu_T}{\mathrm{Sc}_T} (\nabla \widetilde{c})^2 - 2 \overline{\rho} \frac{\varepsilon}{k} \widetilde{c''^2} \left(1 - \frac{\overline{W_{ff}}}{W} g \right) - 2 \widetilde{c''^2} \frac{\overline{W_i}}{W} \overline{S^i} + 2 \overline{c S^c} - 2 \widetilde{c} \overline{S^c} \qquad \text{(B.26)}$$

This expression can be rewritten some further, using the expression for the enthalpy scalar i from expression (B.20). The term S^i refers to the complete source term of the i-equation, which is:

$$\overline{S^i} = \overline{\rho} \left(\widetilde{i} - 1 \right) \overline{\left(\frac{V_{ff}}{V} \right)} \frac{\varepsilon}{k} g - \overline{S^{\mathrm{rad},i}} \qquad \text{(B.27)}$$

When this is inserted in expression (B.26) this results in:

$$\nabla. \left(\overline{\rho} \widetilde{u} \widetilde{c''^2} \right) - \nabla. \left(D_T \nabla \widetilde{c''^2} \right)$$

$$= 2 \frac{\mu_T}{\mathrm{Sc}_T} (\nabla \widetilde{c})^2 - 2 \overline{\rho} \frac{\varepsilon}{k} \widetilde{c''^2} \left(1 - g \left(\frac{\overline{W_{ff}}}{W} - 2 \left(\widetilde{i} - 1 \right) \frac{\overline{V_{ff}}}{V} \cdot \frac{\overline{W_i}}{W} \right) \right)$$

$$+ \quad 2 \overline{c S^c} - 2 \widetilde{c} \overline{S^c} + 2 \widetilde{c''^2} \frac{\overline{W_i}}{W} \overline{S^{\mathrm{rad},i}} \qquad \text{(B.28)}$$

B.3.4 The Favre-averaged equations

Summarizing the efforts from the above sections, the CFI transport equations are as follows, where the mixture fraction equations have been included for completeness:

Reaction progress variable, c

$$\nabla. (\overline{\rho} \widetilde{u} \widetilde{c}) - \nabla. (\overline{\rho} D_T \nabla \widetilde{c}) = \overline{S^c} + \overline{\left(\frac{W_i}{W} \right) c S^{\mathrm{rad},i}}$$

$$+ \quad \left(\overline{\left(\frac{W_{ff}}{W} \right)} + \left(1 - \widetilde{i} \right) \overline{\left(\frac{W_i}{W} \right)} \cdot \overline{\left(\frac{V_{ff}}{V} \right)} \right) \overline{\rho} \widetilde{c} \frac{\varepsilon}{k} g \qquad \text{(B.29)}$$

$$\nabla. \left(\overline{\rho} \widetilde{u} \widetilde{c''^2} \right) - \nabla. \left(D_T \nabla \widetilde{c''^2} \right) = 2 \frac{\mu_T}{\mathrm{Sc}_T} (\nabla \widetilde{c})^2$$

$$- \quad 2 \overline{\rho} \frac{\varepsilon}{k} \widetilde{c''^2} \left(1 - g \left(\frac{\overline{W_{ff}}}{W} - 2 \left(\widetilde{i} - 1 \right) \frac{\overline{V_{ff}}}{V} \cdot \frac{\overline{W_i}}{W} \right) \right)$$

$$+ \quad 2 \overline{c S^c} - 2 \widetilde{c} \overline{S^c} + 2 \widetilde{c''^2} \frac{\overline{W_i}}{W} \overline{S^{\mathrm{rad},i}} \qquad \text{(B.30)}$$

Mixture fraction, f

$$\overline{\rho}\widetilde{\boldsymbol{u}}\nabla\widetilde{f} = \nabla\left(\overline{\rho}D_T\nabla\widehat{f}\right) \tag{B.31}$$

$$\overline{\rho}\widetilde{\boldsymbol{u}}\nabla g = \nabla\left(D\nabla g\right) + 2\frac{\mu_T}{\mathrm{Sc}_T}\left(\nabla\widehat{f}\right)^2 - \frac{\mu_T}{\mathrm{Sc}_T}g \tag{B.32}$$

Enthalpy scalar, i

$$\nabla.\left(\overline{\rho}\widetilde{\boldsymbol{u}i}\right) - \nabla.\left(\overline{\rho}D_T\nabla\widetilde{i}\right) = \overline{\rho}\left(\widetilde{i}-1\right)\overline{\left(\frac{V_{ff}}{V}\right)}\frac{\varepsilon}{k}g - \overline{S^{\mathrm{rad},i}} \tag{B.33}$$

Appendix C

Using the global CSP algorithm

The global CSP algorithm reduces a detailed reaction mechanism based on the result (at the moment) of a 1-dimensional numerical solution of a laminar, freely propagating, perfectly premixed flame. This result can be obtained with either the RUN-1DL code [53] or the PREMIX code [28]. Any other flame can be used as reference, but at the moment this type is used, also in ref. [44]. Based on this flame result, a global reduced mechanism is obtained. The necessary inputs for the CSP code are the following:

- CHEMKIN link file containing detailed reaction mechanism info and thermochemical data

- Desired number of steps in reduced mechanism, S

- File containing laminar flame solution, from RUN-1DL or PREMIX

It must be noted that the species ordering as it is provided in the CHEMKIN link file will be used throughout the code. It is essential that this link file is identical to the one used to create the premixed flame solution. Since usually the last species is not solved but obtained by truncation of the other species in the laminar flame solver, N2 should always be the last species in the list.

The code first reads in the input files, then the mechanism is reduced onto the element conservation relations, the steady-state relations and the reduced mechanism. Various files are created by the program. The most important are the files *redmec.out* and *b.mat*. The text file *redmec.out* contains the information of the reduced mechanism. In it the following information is displayed:

- Dimensions:

    - Number of species in detailed mechanism N
    - Number of elements in detailed mechanism E
    - Number of reactions in detailed mechanism K
    - Number of steady-state relations M
    - Number of steps chosen in reduced mechanism $N - M - E$

- CSP-reactions of reduced mechanism

- Global reaction rates of CSP reactions

- Steady-state species and their relations to the reactions in the detailed mechanism

- Steady-state species and major species list

The text file $b.mat$ is a textual representation of the $\widehat{\boldsymbol{b}}$-matrix created by CSP. The columns in this text file represent the species. The ordering is determined by the CHEMKIN link file. The rows represent:

- 1 to M: Steady state species: $\widetilde{\boldsymbol{b}}^{r}$

- M+1 to N-S: element conservation relations: $\widehat{\boldsymbol{b}}^{c}$

- N-S to N: the matrix $\widehat{\boldsymbol{b}}^{s}$

All elements b_{ij}^{r} will contain zeros, except for the mth steady-state species for which $\widehat{b}_{im}^{r} = 1$, for $m = 1, .., M$. The elements $\widehat{b}_{ej}^{c}$ contain the number of moles of element e in species j, $e = 1, .., E$. Finally, the elements of $\widehat{b}_{sj}^{s}$ contain the number of moles of species j in composed species vector s, $s = 1, .., S$.

Appendix D

The reduced mechanisms

The species list of the GRI-3.0 mechanism is given in table D.1. The steady-state species list of the 1- and 2-step reduced mechanisms is given in table D.3. The species between brackets is only in steady-state in the 1-step mechanism. The major species are presented in table D.2, with the species between brackets only present in the 2-step mechanism. In tables D.4 and D.5 the CSP mapping of the reduced mechanism, $\widehat{b}^s \cdot X$ is shown.

H2	H	O	O2	OH
H2O	HO2	H2O2	C	CH
CH2	CH2(S)	CH3	CH4	CO
CO2	HCO	CH2O	CH2OH	CH3O
CH3OH	C2H	C2H2	C2H3	C2H4
C2H5	C2H6	HCCO	CH2CO	HCCOH
N	NH	NH2	NH3	NNH
NO	NO2	N2O	HNO	CN
HCN	H2CN	HCNN	HCNO	HOCN
HNCO	NCO	AR	C3H7	C3H8
CH2CHO	CH3CHO	N2		

Table D.1: Species list of the GRI-3.0 mechanism.

CO	CO2	O2	H2O	(H2)
N2	AR			

Table D.2: Major species list of the reduced mechanisms.

NNH	H2CN	HCNN	HOCN	CN
HNO	NH3	NH2	HCNO	NCO
NH	NO2	C3H7	N2O	N
C2H	HNCO	HCCOH	CH2CHO	C
HCN	CH2(S)	CH2OH	CH	HCCO
C3H8	C2H3	H2O2	CH3O	CH3CHO
C2H5	HCO	CH3OH	CH2	CH2CO
HO2	C2H2	C2H4	CH2O	C2H6
NO	O	CH3	H	OH
CH4	(H2)			

Table D.3: Steady-state species list of the reduced mechanisms.

-0.50 H	-1.00 O	-1.00 O2	-0.50 OH	-1.50 HO2
-1.00 H2O2	-1.00 C	-0.50 CH	+0.50 CH3	+1.00 CH4
-0.50 HCO	-0.50 CH2OH	-0.50 CH3O	+1.50 C2H	+2.00 C2H2
+1.50 C2H3	+2.00 C2H4	+1.50 C2H5	+1.00 C2H6	+0.50 HCCO
+2.00 CH2CO	+2.00 HCCOH	-1.00 N	-0.50 NH	-1.00 NH2
-0.50 NH3	-0.50 NNH	-1.00 NO	-1.00 NO2	-1.00 N2O
-0.50 HNO	+0.50 HCN	-0.50 HCNN	-0.50 HCNO	+0.50 HOCN
-0.50 HNCO	+2.50 C3H7	+2.00 C3H8	+1.50 CH2CHO	+1.00 CH3CHO

Table D.4: Composed species $\widehat{\eta}_1^s$ of the 1-step reduced mechanism.

RPV 1:				
-0.50 H2	-0.75 H	-0.50 O	-0.25 OH	-0.75 HO2
-0.50 H2O2	-1.50 C	-1.25 CH	-1.00 CH2	-1.00 CH2(S)
-0.75 CH3	-0.50 CH4	-0.75 HCO	-0.50 CH2O	-1.25 CH2OH
-1.25 CH3O	-1.00 CH3OH	0.25 C2H	0.50 C2H2	-0.25 C2H3
-0.75 C2H5	-1.50 C2H6	-0.25 HCCO	1.00 CH2CO	1.00 HCCOH
-1.00 N	-0.75 NH	-1.50 NH2	-1.25 NH3	-0.75 NNH
-0.50 NO	-0.50 N2O	-0.25 HNO	-0.50 CN	-0.25 HCN
-1.00 H2CN	-1.25 HCNN	-0.75 HCNO	0.25 HOCN	-0.75 HNCO
-0.75 C3H7	-1.50 C3H8	0.25 CH2CHO	-0.50 CH3CHO	
RPV 2:				
0.50 H2	+0.25 H	-0.50 O	-1.00 O2	-0.25 OH
-0.75 HO2	-0.50 H2O2	+0.50 C	+0.75 CH	+1.00 CH2
+1.00 CH2(S)	+0.25 CH3	+1.50 CH4	+0.25 HCO	+0.50 CH2O
+0.75 CH2OH	+0.75 CH3O	+1.00 CH3OH	+1.25 C2H	+1.50 C2H2
+1.75 C2H3	+2.00 C2H4	+2.25 C2H5	+2.50 C2H6	+0.75 HCCO
+1.00 CH2CO	+1.00 HCCOH	+0.25 NH	+0.50 NH2	+0.75 NH3
+0.25 NNH	-0.50 NO	-1.00 NO2	-0.50 N2O	-0.25 HNO
+0.50 CN	+0.75 HCN	+1.00 H2CN	+0.75 HCNN	-0.25 HCNO
+0.25 HOCN	+0.25 HNCO	+1.00 C3H7	+3.50 C3H8	+1.25 CH2CHO
+1.50 CH3CHO				

Table D.5: Composed species $\widehat{\eta}_1^s$, $\widehat{\eta}_2^s$ of the 2-step reduced mechanism.

Appendix E

Grid independency study

The cold flow of the Base case has been calculated twice, once with the complete geometry and once with the reduced geometry with the transferred boundary conditions. In this appendix the comparison between the two calculations is presented. Since the grid density in the combustion chamber is almost half in the complete geometry with respect to the reduced one, this assessment can also be interpreted as a grid independency study.

In figures E.1, E.2 and E.3 the axial profiles of the axial velocity, k and ε are plotted on the centerline of the combustor. The variable h is 0 in the burner exit. From these graphs is can be observed that the agreement is excellent. In figures E.4 to E.7, data is plotted at 1.5 mm above the burner exit plane. The direction is through the mid-plane of the combustor side wall. Again, the comparison is excellent, although the peak values of k and ε differ slightly. It can be shown that the comparison of these quantities improves further away from the burner mouth.
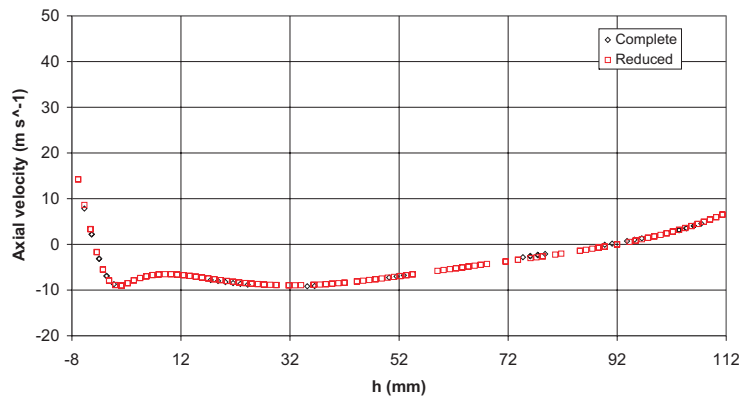
Figure E.1: Axial velocity profiles at centerline.
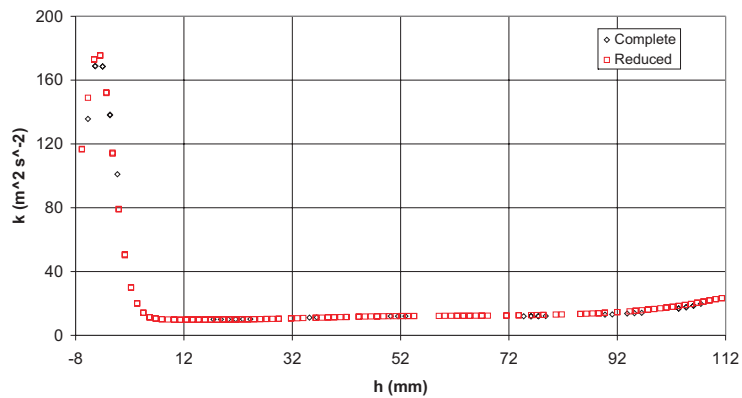
Figure E.2: Profiles of k at centerline.
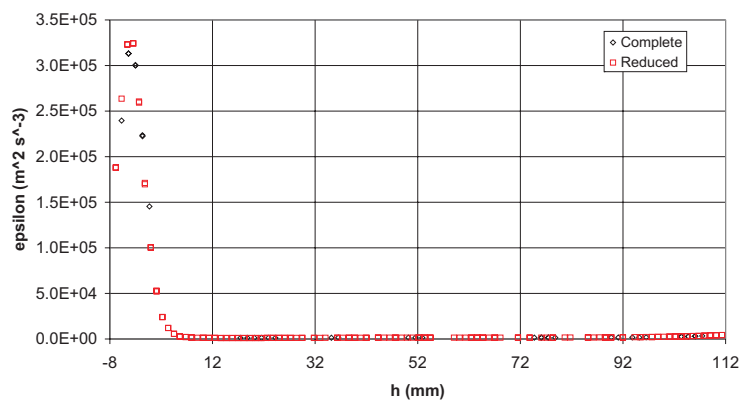
Figure E.3: Profiles of ε at centerline.
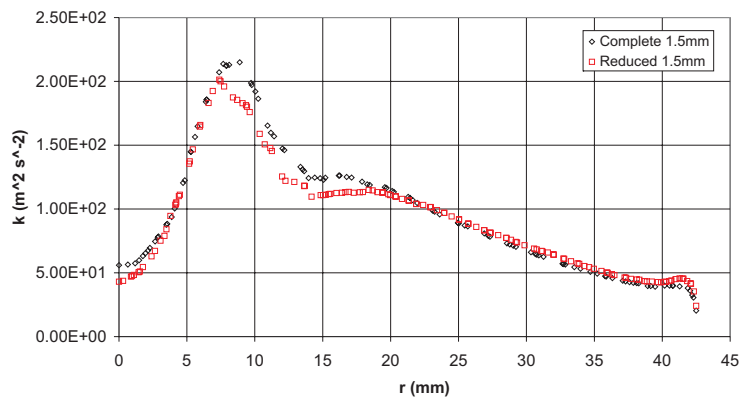
Figure E.4: Profiles of k at 1.5 mm from the burner exit.
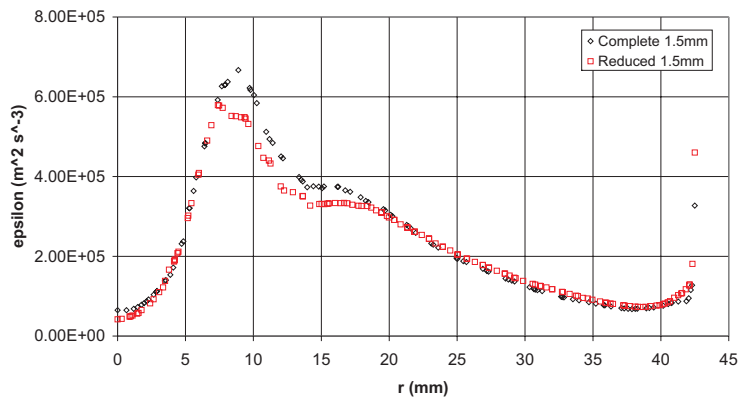
Figure E.5: Profiles of ε at 1.5 mm from the burner exit.
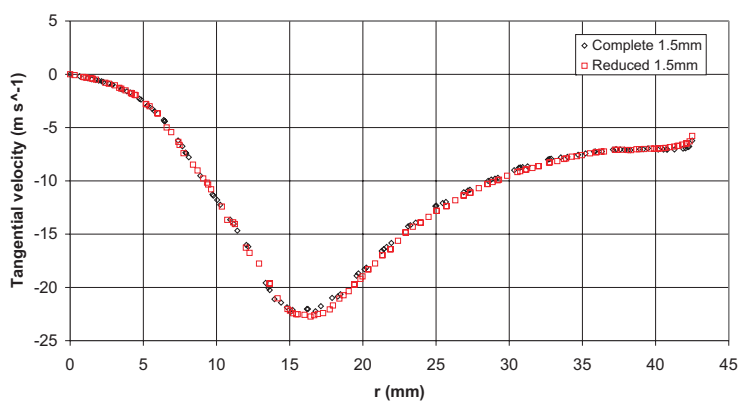
Figure E.6: Profiles of the radial velocity at 1.5 mm from the burner exit. Positive values denote movement towards the origin.
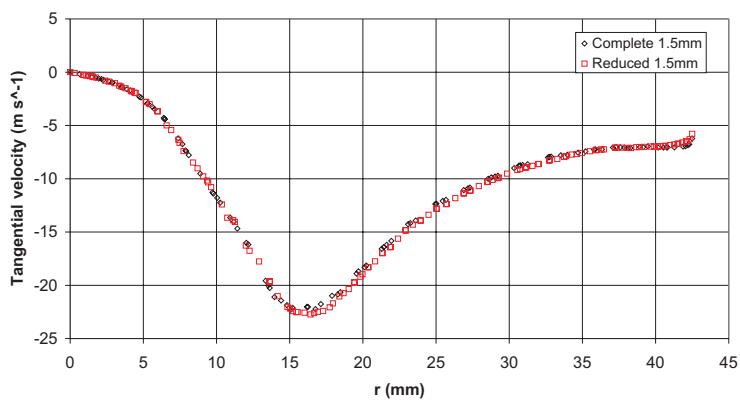
Figure E.7: Profiles of the tangential velocity at 1.5 mm from the burner exit.

Appendix F

Turbulent case study graphs

In this appendix, figures F.1 to F.4, the CFD graphs mentioned in chapter 4 are shown. Furthermore, the flow fields of the Base case, Steam case and N2 of the comparison study case are depicted. In figure F.5 the velocity vectors of the 3 cases are plotted for the axial mid-plane. In figure F.6, the recirculation zones of the 3 cases are visualized. In figure F.7 the temperatures through the axial midplane are shown, where the graphs all obey the left legend. The peak temperatures are 2012 K, 1894 K and 1904 K for the Base case, Steam case and N2 case, respectively. The peak temperature of the legend arises in the axial mid-plane of the plot of the Base case. In figure F.8, the O mass fractions are plotted for the 3 cases. In figure F.9, the NO source terms are shown. In figures F.11, F.12and F.13 the means and variances of c and the variance of f are shown, respectively.
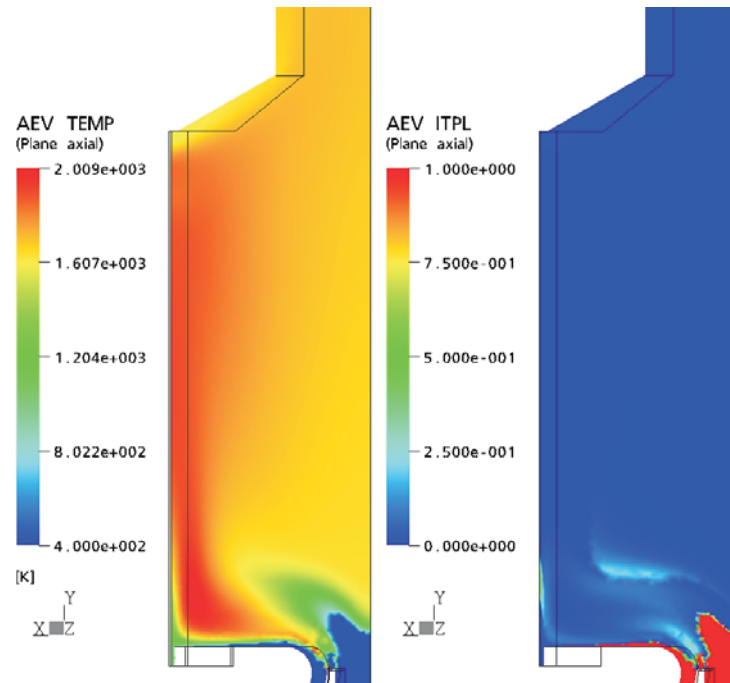
Figure F.1: Temperatures (left) and integrated interpolation scalar (right), Base case, axial plane through the mid-plane of a combustor side wall.
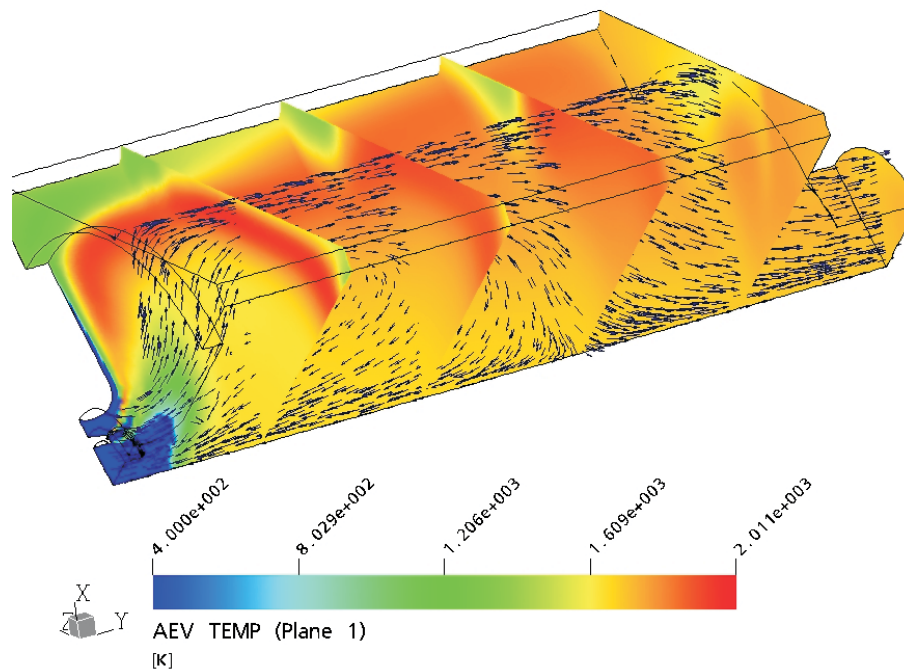
Figure F.2: Temperature profiles for the Base case. Shown are a periodic plane and various planes perpendicular to that. Velocity vectors are shown in black in the axial mid-plane.
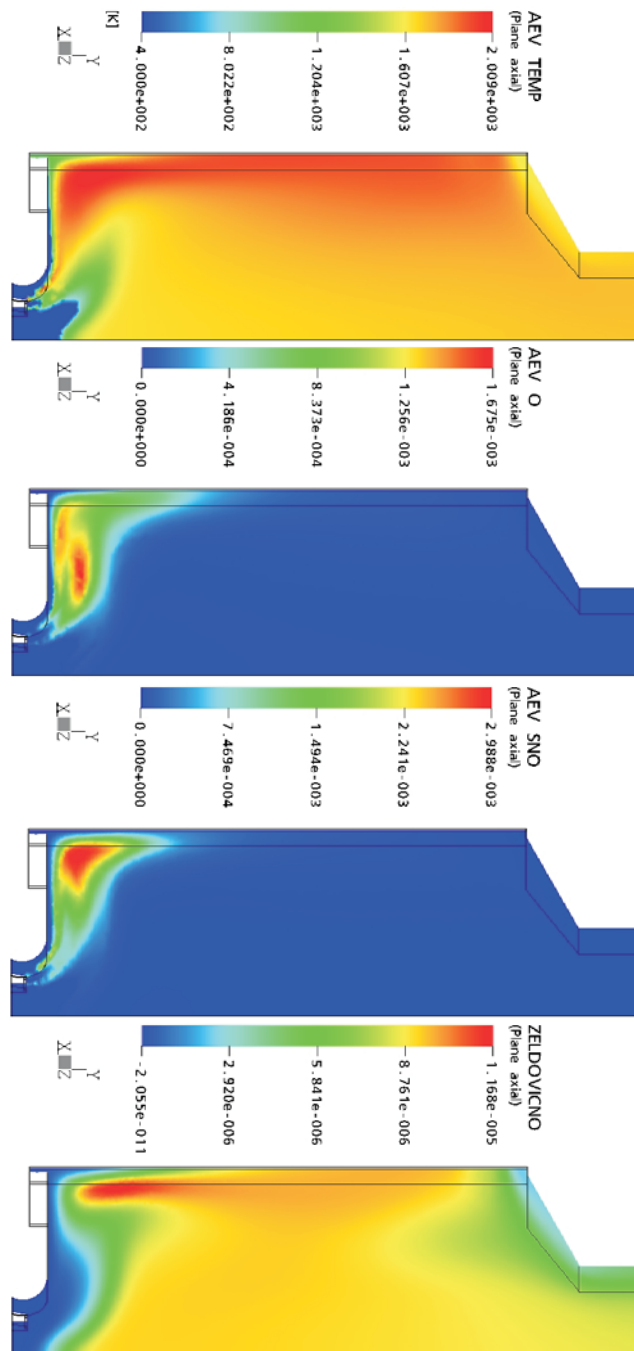
Figure F.3: From top to bottom: Temperature profiles, O mass fractions, NO source term and NO mass fractions for the Base case, shown in the axial mid-plane.
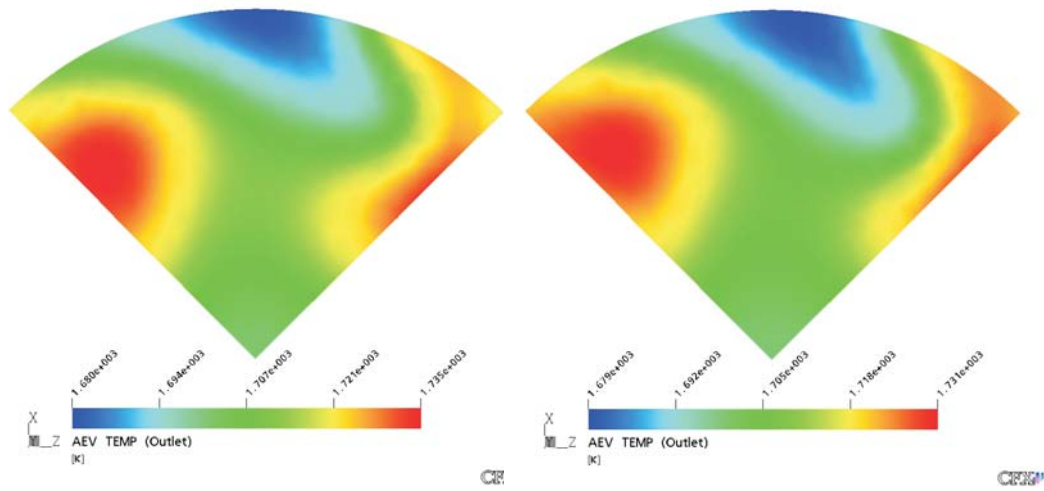
Figure F.4: Exit temperature profiles, Base case (left) and Steam case (right).
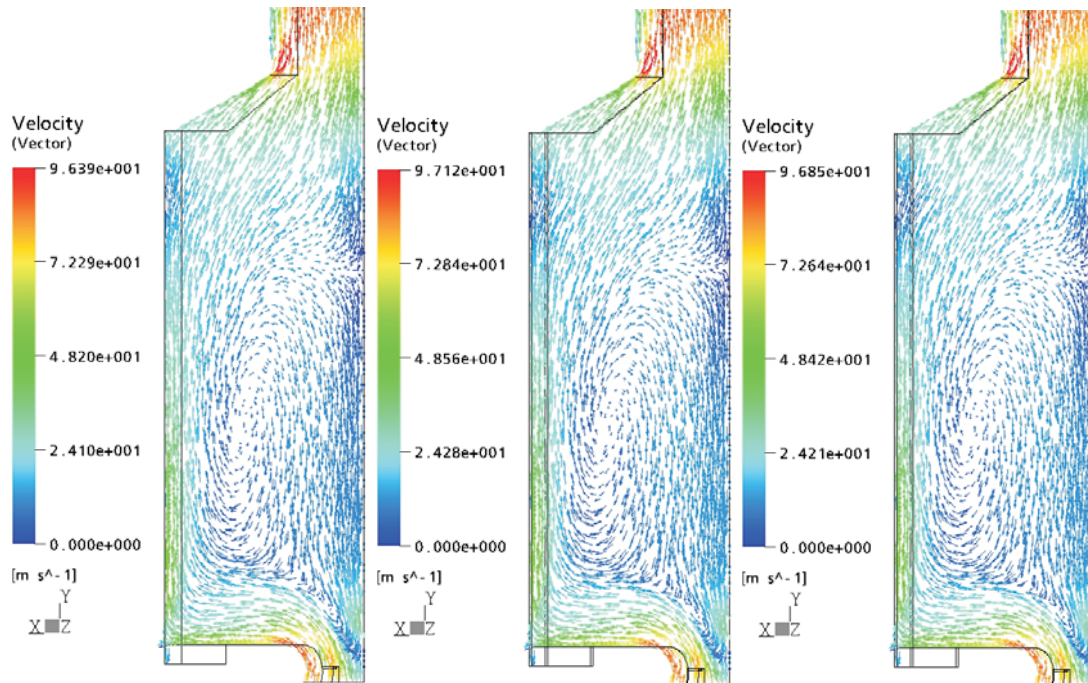
Figure F.5: Velocity vectors of the axial mid-plane, Base case (left), Steam case (middle) and N2 case (right).
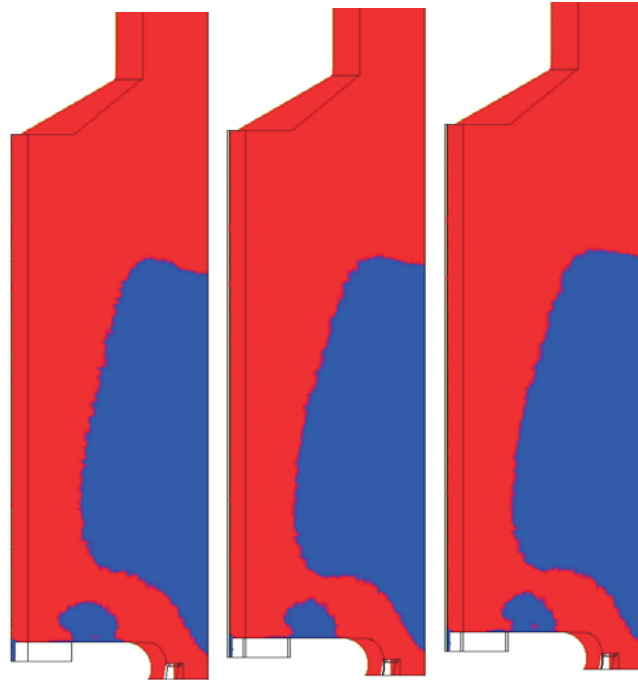
Figure F.6: Recirculation zones, axial mid-plane, Base case (left), Steam case (middle) and N2 case (right). Red indicates positive axial velocity, blue negative.
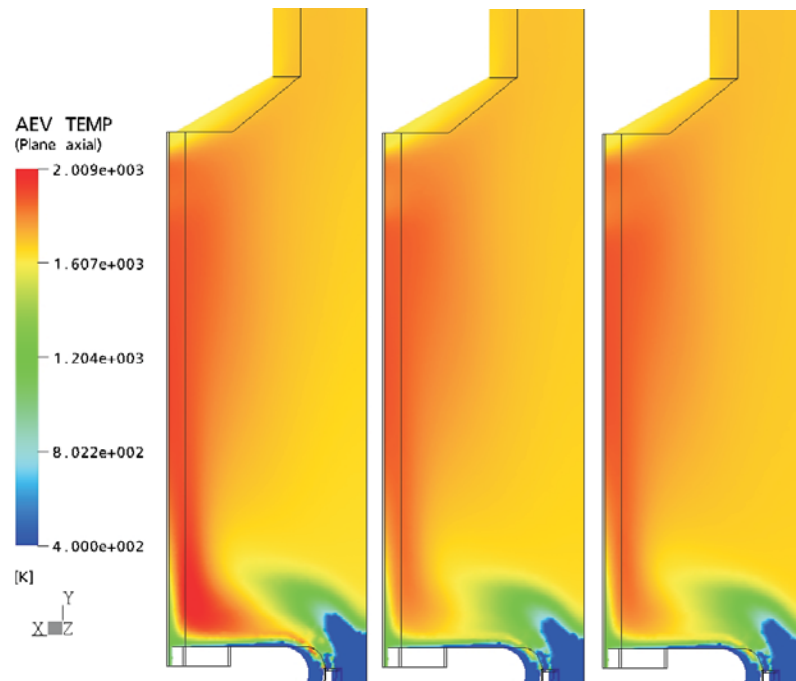
Figure F.7: Temperatures, axial mid-plane, Base case (left), Steam case (middle) and N2 case (right).
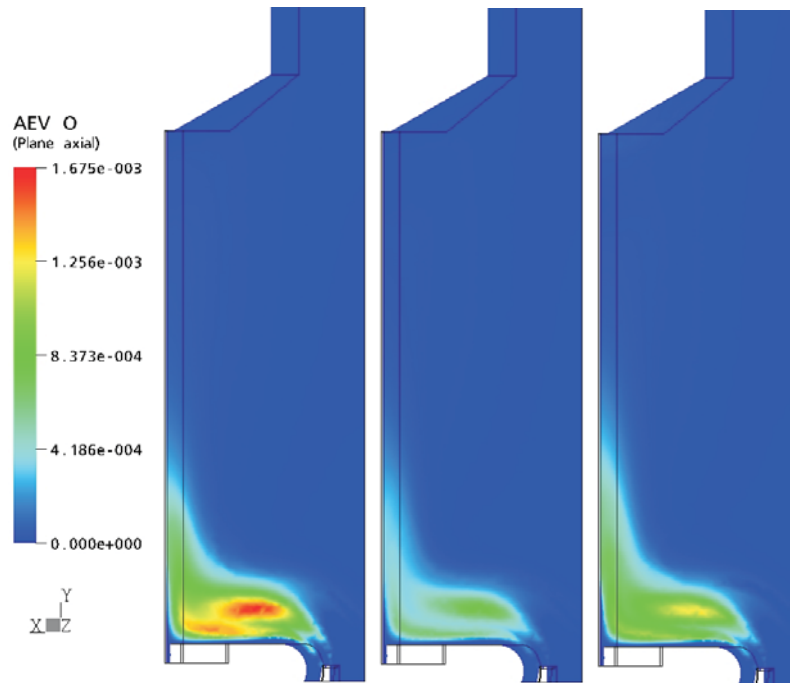
Figure F.8: O Mass fractions, axial mid-plane, Base case (left), Steam case (middle) and N2 case (right).
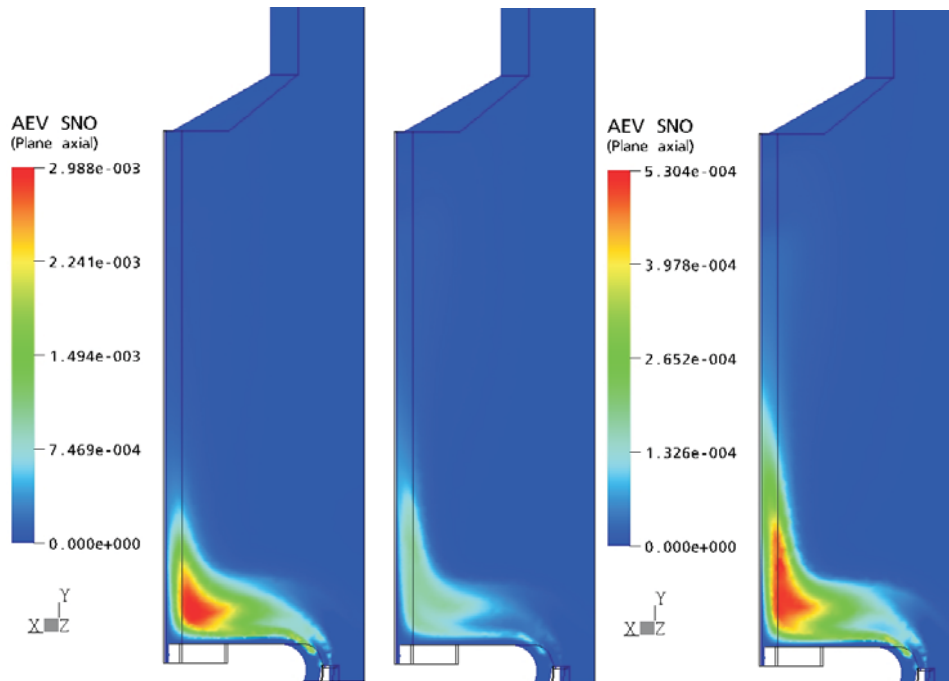
Figure F.9: NO source terms, axial mid-plane, Base case (left), Steam case (middle) and N2 case (right). The middle and right plot colors are represented in the right legend, the colors of the left plot are identified in the left legend.
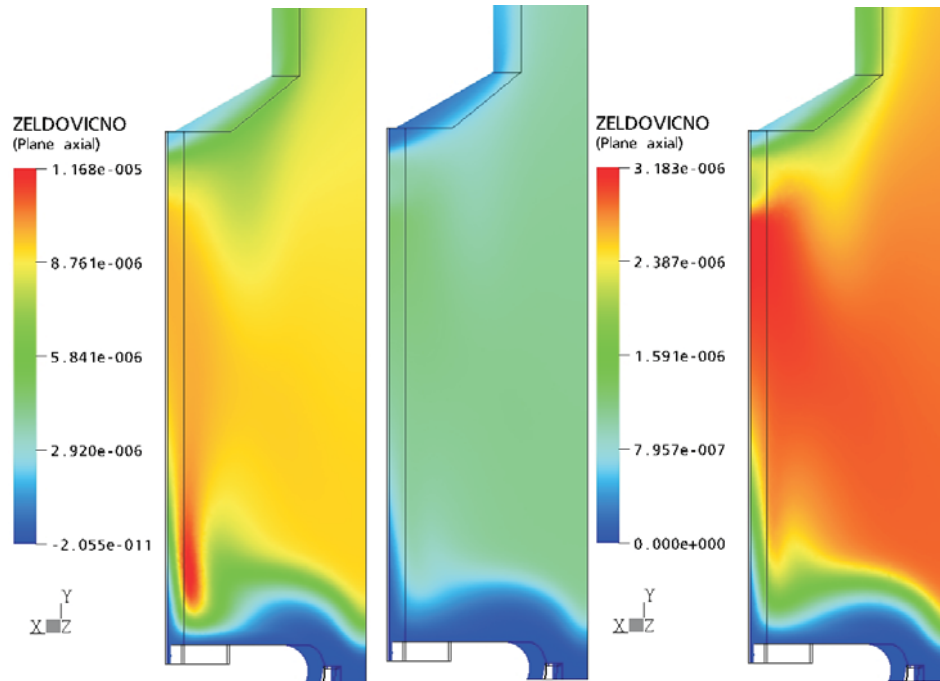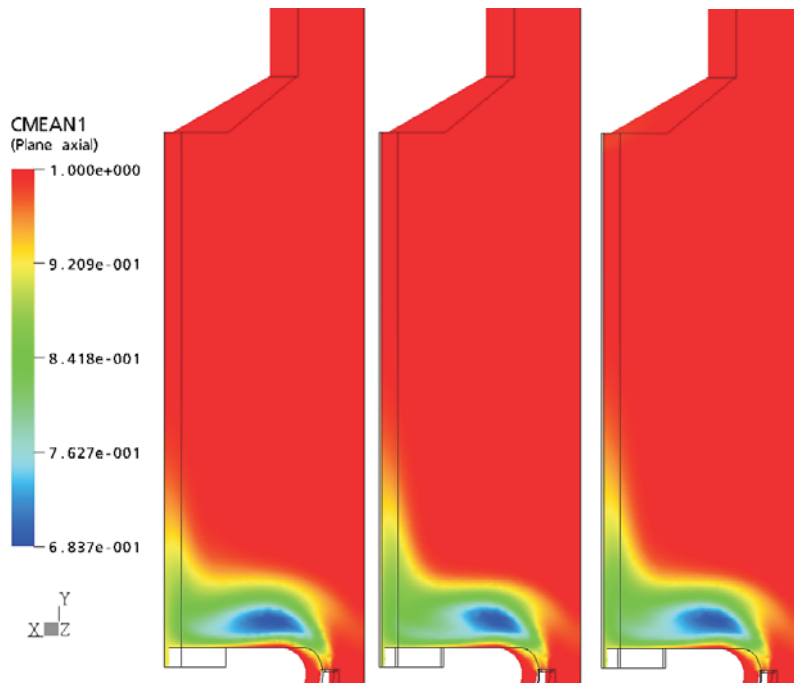
Figure F.10: NO Mass fractions, axial mid-plane, Base case (left), Steam case (middle) and N2 case (right). The middle and right plot colors are represented in the right legend, the colors of the left plot are identified in the left legend.

Figure F.11: Profiles of $\widetilde{c}$, axial mid-plane, Base case (left), Steam case (middle) and N2 case (right).
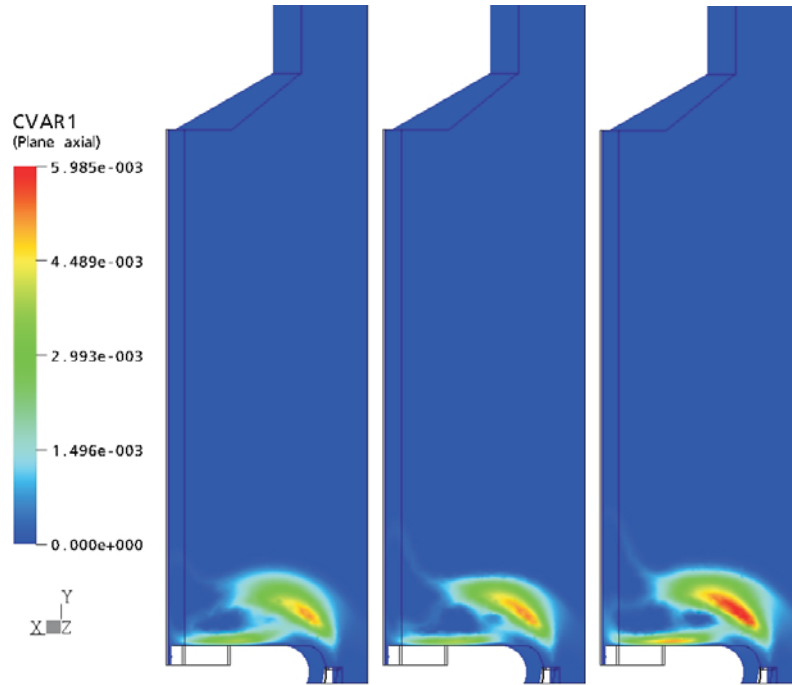
Figure F.12: Profiles of $\widetilde{c''^2}$, axial mid-plane, Base case (left), Steam case (middle) and N2 case (right).
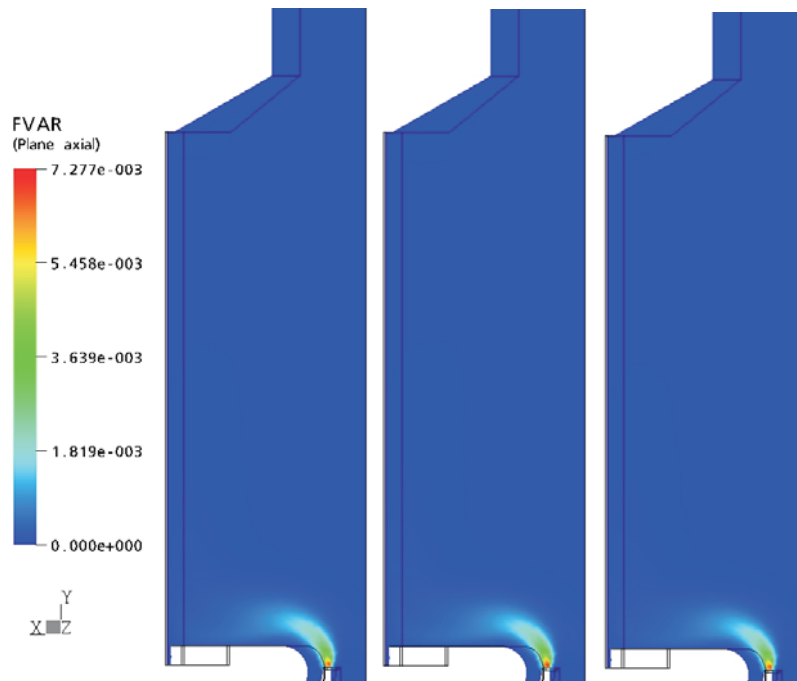

Figure F.13: Profiles of $\widetilde{f''^2}$, axial mid-plane, Base case (left), Steam case (middle) and N2 case (right).

Bibliography

[1] Ågren, N. (2000), Advanced Gas Turbine Cycles with Water-Air Mixtures as Working Fluid, PhD Thesis, Dept. of Chemical Engineering and Technology/Energy Processes, Stockholm, Sweden

[2] Albrecht, B.A. (2004), Reactor modeling and process analysis for partial oxidation of natural gas, PhD Thesis, University of Twente, Enschede, The Netherlands

[3] Ansys CFX, http://www-waterloo.ansys.com/cfx/

[4] CFX-5.6 Reference manual, ANSYS, Inc., Canonsburg, PA, United States of America

[5] Bhargava, A., Colket, M., Sowa, W., Castleton and Maloney, D. (2000), *An Experimental and Modeling study of Humid Air Premixed Flames*, ASME Journal of Engineering for Gas Turbines and Power 122, pp. 405-411

[6] Bolland, O. and Stadaas, J.F. (1995), *Comparative Evaluation of combined Cycles and Gas Turbine Systems With Water Injection, Steam Injection, and Recuperation*, ASME Journal of Engineering for Gas Turbines and Power 117, pp. 138-145

[7] Borghi, R. (1988), *Turbulent combustion modelling*, Prog. Energy Comb. Sci. 14, pp. 245-292

[8] Brewster, B.S., Cannon, S.M., Farmer, J.R. and Meng, F. (1999), *Modeling of lean-premixed combustion in stationary gas turbines*, Progress in Energy and Combustion Science 25, pp. 353-385

[9] Chiesa, P., Lozza, G., Macchi, E. and Consonni, S. (1995), *An Assessment of the Thermodynamic Performance of Mixed Gas-Steam Cycles: Part B–Water-Injected and HAT Cycles*, ASME Journal of Engineering for Gas Turbines and Power 117, pp. 499-508

[10] Correa, S.M. (1985), *A model for non-premixed turbulent combustion of CO/H_2 jets*, Archivum Combustionis 5 (3-4), pp. 223-243

[11] Derksen, M.A.F., Kok, J.B.W. and Van Der Meer, Th.H. (2003), *Modelling of Turbulent Combustion with Reaction Progress Variables and CSP*, European Combustion Meeting, Orléans, France

[12] Derksen, M.A.F. and Kok, J.B.W. (2004) *Simulations of Turbulent Combustion of Natural Gas using a CSP-based Progress Variable Approach*, Joint Meeting of the Greek and Italian Sections of the Combustion Institute, Corfu, Greece

[13] Duan, X.R., Weigand, P., Meier, W., Keck, O., Stricker, W. and Aigner, M. (2004), *Experimental investigations and laser based validation measurements in a gas turbine model combustor*, Progress in Computational Fluid Dynamics 4 (3-5), pp. 175-182

[14] Durbin, P.A. and Petterson-Reif, B.A. (2001), Statistical theory and modeling for turbulent flows, John Wiley and Sons Ltd., Chichester, England

[15] Eastop, T.D. and McConkey A. (1993), Applied Thermodynamics for Engineering Technologists, Fifth Edition, John Wiley and Sons, New York, USA

[16] El-Masri, M.A. (1988), *A Modified, high-Efficiency, Recuperated Gas Turbine Cycle*, ASME Journal of Engineering for Gas Turbines and Power 110, pp. 233-242

[17] Gallo, W.L.R. (1997), *A comparison between the HAT cycle and other gas-turbine based cycles: efficiency, specific power and water consumption*, Energy Conversion and Management 38 (15-17), pp. 1595-1604

[18] Geurts, B.J. (2004), Elements of direct and large-eddy simulation, R.T. Edwards, Philadelphia, United States of America

[19] Giezendanner, R., Weigand, P., Duan, X.R., Meier, W., Meier, U., Aigner, M. and Lehmann, B. (2004), *Laser based investigations of periodic combustion instabilities in a gas turbine model combustor*, Proceedings of ASME Turbo Expo 2004, Vienna, Austria

[20] Janicka, J. and Kollmann, W. (1979), *A two-variables formalism for the treatment of chemical reactions in turbulent H_2-air diffusion flames*, 17th symposium (International) on Combustion, The Combustion Institute, Pittsburg, USA, pp. 421-430

[21] Janicka, J. and W. Kollmann (1982), *The calculation of mean radical concentrations in turbulent diffusion flames*, Combustion and Flame 44, pp. 319-336

[22] Heppenstal T. (1998), *Advanced gas turbine cycles for power generation: a critical review*, Applied Thermal Engineering 18, pp. 837-846

[23] Hilbert, R., Tap, F., El-Rabii, H. and Thévinin, D. (2004), *Impact of detailed chemistry and transport models on turbulent combustion simulations*, Progress in Energy and Combustion Science 30, pp. 61-117

[24] Hoffmann, J. and Agostinelli, G.L., *High Fogging Commissioning Test in the Alstom Test Center Birr (Switzerland)*, Paper No 205, Alstom Schweiz AG, Baden, Switzerland

[25] Horlock, J.H. (1997) *Aero-Engine Derivative Gas Turbines for Power Generation: Thermodynamic and Economic Perspectives*, ASME Journal of Engineering for Gas Turbines and Power 119, pp. 119-122

[26] Horlock, J.H. (1998), *The Evaporative Gas Turbine [EGT] Cycle*, ASME Journal of Engineering for Gas Turbines and Power 120, pp. 336-343

[27] Jones, W.P. and Whitelaw, J.H. (1984), *Modelling and measurements in turbulent combustion*, 20th symposium (international) on combustion, The Combustion Institute, Pittsburgh, United States of America

[28] Kee, R.J., Rupley, F.M., Miller, J.A., Coltrin, M.E., Grcar, J.F., Meeks, E., Moffat, H.K., Lutz, A.E., Dixon-Lewis, G., Smooke, M.D., Warnatz, J., Evans, G.H., Larson, R.S., Mitchell, R.E., Petzold, L.R., Reynolds, W.C., Caracotsios, M., Stewart, W.E., Glarborg, P., Wang, C. and Adigun, O. (2000), *CHEMKIN Collection*, Release 3.6, Reaction Design Inc., San Diego, United States of America

[29] Kok, J.B.W., Louis, J.J.J. and Yu J.H. (1999), *The IRST model for turbulent premixed non-adiabatic flames*, Combustion Science and Technology. 149, pp. 225-247

[30] Korobitsyn, M.A. (1998), New and advanced energy conversion technologies. Analysis of cogeneration, combined and integrated cycles, PhD Thesis, Febodruk BV, Enschede, The Netherlands

[31] Kolp, D.A. and Moeller, D.J. (1989), *World's First Full STIG^{tm} LM5000 Installed at Simpson Paper Company*, ASME Journal of Engineering for Gas Turbines and Power 111, pp. 200-210

[32] Lam, S.H. and Goussis, D.A. (1994), *The CSP method for simplifying kinetics*, International Journal of Chemical Kinetics 26, pp. 461-486

[33] Landman, M.J. (2003), Onderzoek naar het gedrag van een Winnox gasturbinebrander, MSc Thesis, Faculty of Engineering Technology, University of Twente, Enschede, The Netherlands

[34] Landman, M.J., Derksen, M.A.F. and Kok, J.B.W. (2005), *Effect of combustion air dilution by water vapour or nitrogen on NO_x emission in a premixed turbulent natural gas flame, an experimental study*, accepted for publication in Combustion Science and Technology

[35] Lazzaretto, A. and Segato, F. (2001), *Thermodynamic Optimization of the HAT Cycle Plant Structure – Part I: Optimization of the "Basic Plant Configuration"*, ASME Journal of Engineering for Gas Turbines and Power 123, pp. 1-7

[36] Lazzaretto, A. and Segato, F. (2001), *Thermodynamic Optimization of the HAT Cycle Plant Structure – Part II: Structure of the heat exchanger network*, ASME Journal of Engineering for Gas Turbines and Power 123, pp. 1-7

[37] Lazzaretto, A. and Segato, F. (2002) *A thermodynamix approach to the definition of the HAT cycle plant structure*, Energy Conversion and Mangagement 43, pp. 1377-1391

[38] Lefebvre, A.H. (1999), Gas Turbine Combustion, 2nd edition, Taylor and Francis, Philadelphia, USA

[39] Louis, J.J.J. (1996), On turbulent combustion of coal gas, PhD Thesis, University of Twente, Enschede, The Netherlands

[40] Louis, J.J.J., Kok, J.B.W. and Klein, S.A. (2001), *Modeling and measurements of a 16-kW turbulent nonadiabatic syngas diffusion flame in a cooled cylindrical combustion chamber*, Combustion and Flame 125 (1-2), pp. 1012-1031

[41] Maas, U. (1998), *Efficient Calculation of Intrinsic Low-dimensional Manifolds for the Simplification of Chemical Kinetics*, Computing and Visualization in Science 1, pp. 69-81

[42] Macchi, E., Consonni, S., Lozza, G. and Chiesa, P. (1995), *An Assessment of the Thermodynamic Performance of Mixed Gas-Steam Cycles: Part A–Intercooled and Steam-Injected Cycles*, ASME Journal of Engineering for Gas Turbines and Power 117, pp. 489-498

[43] Martínez, J.M. (1994), *Algorithms for Solving Nonlinear Systems of Equations*, in: Spedicato, E. (Ed), Algorithms for Continuous Optimization, Kluwer Academic Publishers, The Netherlands, opp. 81-108

[44] Massias A., Diamantis D., Mastorakos E. and Goussis D.A. (1999), *An Algorithm for the Construction of Global Reduced Mechanisms with CSP Data*, Combustion and Flame 117, pp. 685-708

[45] Najjar, Y.S.H. and Zaamout, M.S. (1996), *Enhancing Gas-Turbine Engine Performance by Means of the Evaporative Regenerative Cycle*, Journal of the Institute of Energy 69, pp. 2-8

[46] Nakhamkin, M., Swensen, E.C., Wilson, J.M., Gaul, G. and polsky, M. (1996), *The Cascaded Humidified Advanced Turbine (CHAT)*, , ASME Journal of Engineering for Gas Turbines and Power 118, pp. 565-571

[47] Nieuwstadt, F.T.M. (1989), *Turbulentie; Dictaat bij het college turbulentie A (b60a)*, revised version, Delft University, Delft, The Netherlands

[48] Pope, S.B. (2000), Turbulent flows, Cambridge University Press, Cambridge, United Kingdom

[49] Press, W.H. (1992), Numerical recepies in Fortran 77: The art of scientific computing, Cambridge university press, Cambridge, UK

[50] Rao, A.D. (1989), "Process for producing power," US Patent 4,829,763

[51] Rice, I.G. (1995), *Steam-Injected Gas Turbine Analysis: Steam Rates*, ASME Journal of Engineering for Gas Turbines and Power 117, pp. 347-353

[52] Ritchey, I., Fisher, E.H. and Agnew, G.D. (2000), *Water spray cooling of gas turbine cycles*, Proceedings of the Institution of Mechanical Engineers 214 (A), pp. 203-214.

[53] Rogg, B. (1993), *RUN-1DL–The Cambridge universal laminar flamelet computer code*, in: Peters, N. and Rogg, B. (Eds.), Reduced Kunetic Mechanisms for Applications in Combustion Systems, Springer, Berlin, pp. 350-351

[54] Rosén, P.M. (2000), Evaporative cycles – in theory and practice, PhD thesis, Lund institute of Technology, Lund, Sweden

[55] Smith, G.P., Golden, D.M., Frenklach, M., Moriarty, N.W., Eiteneer, B., Goldenberg, M., Bowman, C.T., Hanson, R.K., Song, S., Gardiner, W.C. Jr., Lissianski, V.V. and Qin, Z. (1999), GRI-mech home page, http://www.me.berkeley.edu/gri_mech/

[56] Traverso, A. and Massardo, A.F. (2002), *Thermoeconomic Analysis of Mixed Gas-Steam Cycles*, Applied Thermal Engineering 22, pp. 1-21

[57] Tuzson, J. (1992), *Status of Steam-Injected Gas Turbines*, ASME Journal of Engineering for Gas Turbines and Power 114, pp. 682-686

[58] Van Berkel, A.I., 1996, MSc-Thesis, University of Twente, The Netherlands

[59] Veynante, D. and L. Vervisch, 2002, *Turbulent combustion modeling*, Prog. Energy Comb. Sci. 28, pp. 193-266

[60] Walsh, P.W. and Fletcher, P. (2004), Gas Turbine Perfomance, Second Edition, Blackwell Science Ltd, Oxford, UK

[61] Weigand, P., Meier, W., Duan, X.R., Stricker, W. and Aigner, M. (2004), *Investigations of Swirl Flames in a Gas Turbine Model Combustor. Part I: Flow Field, Structures, Temperature and Species Distributions*, to appear

[62] Weiser, A. and Zarantonello, S.E. (1988), *A Note on Piecewise Linear and Multilinear Table Interpolation in Many Dimensions*, Mathematics of Computation 50 (181), pp. 189-195

[63] Williams, F.A., Combustion Theory (1985), $2nd$ edition, The Benjamin/Cummings Publishing Company, Inc., Menlo park, California, United States of America

[64] Yu, J.H. (1996), On formation of NO_x and CO in turbulent premixed combustion, PhD Thesis, University of Twente, Enschede, The Netherlands

[65] Zhao, D., Yamashita, H., Furuhata, T. and Arai, N. (2000), *Analysis of Combustion Characteristics of Coaxial Jet Diffusion Flame with Steam Addition*, Journal of Propulsion and Power 16 (4), pp. 552-556

[66] Zhao, D., Yamashita, H., Kitagawa, K. and Furuhata, T. (2002), *Behavior and Effect on NOx Formation of OH radical in Methane-Air Diffusion Flame with Steam Addition*, Combustion and Flame 130, pp. 352-360

Curriculum Vitae

Marco Anton Frederik Derksen is 15 april 1973 geboren in Nijmegen. In 1990 haalde hij zijn HAVO diploma, en in 1992 zijn VWO diploma aan het Canisius College Mater Dei in Nijmegen. Hierna begon hij een studie Technische Natuurkunde aan de Technische Universiteit Twente te Enschede. In januari 1993 stapte hij over naar de opleiding Werktuigbouwkunde aan diezelfde universiteit.

Daar koos hij de afstudeerrichting Thermische Werktuigbouwkunde. Tijdens zijn opleiding heeft hij een stage genoten van 6 maanden bij ABB Power Generation Ltd. (Nu Alstom Power) in Baden, Zwitserland. Hier heeft hij onder begeleiding van Dr. E.G. Engelbrecht diverse engineeringsprojecten uitgevoerd in de brandergroep van de ontwikkelingsafdeling van het bedrijf. In april 2000 studeerde hij af onder begeleiding van Dr.Ir. J.B.W. Kok op het onderwerp "Large-eddy simulations of spatially developing turbulent internal flows."

Na zijn afstuderen heeft Marco 6 maanden gewerkt aan de universiteit Twente, in een project in samenwerking met het ECN te Petten, onder begeleiding van Prof.Dr. H.J. Veringa. In deze periode heeft hij een technologische ontwerpmethode ontwikkeld en gerealiseerd voor de Stirling gedreven Stirling warmtepomp (Stirling Driven Heat Pump ofwel SDHP).

In november 2000 is hij begonnen aan zijn promotieonderzoek bij de vakgroep Thermische Werktuigbouwkunde van de Universiteit Twente. Het onderzoek "On the influence of steam on combustion" is uitgevoerd onder leiding van Prof.Dr. Th.H. van der Meer en onder begeleiding van Dr.Ir. J.B.W. Kok.

In januari 2005 is Marco begonnen bij Stork Thermeq B.V. in Hengelo (Ov.), waar hij werkzaam is als Combustion Engineer.

Publicaties

1. Derksen, M.A.F., Kok, J.B.W. and Van Der Meer, Th.H. (2003), *Modelling of Turbulent Combustion with Reaction Progress Variables and CSP*, European Combustion Meeting, Orléans, France

2. Skevis, G., Chrissanthopoulos, A., Goussis, D.A., Mastorakos, E., Derksen, M.A.F. and Kok, J.B.W. (2003), *Numerical investigation of methane combustion under MAST conditions*, First International Conference on Gas Turbine Technologies, Brussels, Belgium

3. Derksen, M.A.F. and Kok, J.B.W. (2004) *Simulations of Turbulent Combustion of Natural Gas using a CSP-based Progress Variable Approach*, Joint Meeting of the Greek and Italian Sections of the Combustion Institute, Corfu, Greece

4. Skevis, G., Chrissanthopoulos, A., Goussis, D.A., Mastorakos, E., Derksen, M.A.F. and Kok, J.B.W. (2004), *Numerical investigation of methane combustion under mixed air-steam turbine conditions-FLAMESEEK*, Applied Thermal Eng. 24, pp. 1607-1618

5. Landman, M.J., Derksen, M.A.F. and Kok, J.B.W. (2005), *Effect of combustion air dilution by water vapour or nitrogen on NO_x emission in a premixed turbulent natural gas flame, an experimental study*, accepted for publication in Combustion Science and Technology